UNIVERSITÀ DEGLI STUDI DELL'INSUBRIA

Facoltà di Scienze Matematiche, Fisiche e Naturali

Anno Accademico 2006-2007

Laurea Specialistica in Fisica

DESIGN AND PERFORMANCE OF FAST, A TRACKER FOR ANTIPROTON PHYSICS

Laureando: Valerio Mascagna
Matricola 521129

Tutor:	Dr.ssa Michela Prest Università degli Studi dell'Insubria
Cotutors:	Dr. Aldo Mozzanica Università degli Studi di Milano
	Dr. Erik Vallazza INFN - Sezione di Trieste

Contents

Riassunto della tesi **VIII**

Introduction **4**

1 Antiproton annihilation cross section **5**
1.1 Historical introduction 5
Antimatter discovery 5
Antiprotons and *CPT* invariance 6
Antiproton annihilation 7
1.2 Antiproton factories 7
1.2.1 Producing and accumulating antiprotons 8
Production methods 8
Accumulating antiprotons 11
1.2.2 Decelerating antiprotons 12
From GeV to MeV 13
LEAR 14
Decelerating below 1 MeV 14
1.3 The Antiproton Decelerator 16
Deceleration cycle 17
Multiple extraction 18
1.4 Annihilation cross section experiments 19
Early experiments 19
The KEK detector 19
1.4.1 The LEAR experiments 20
ASTERIX (PS171) 20
OBELIX (PS 201) 21
Crystal Barrel (PS 197) 23
1.4.2 Overview of the LEAR results 25
1.4.3 Cross section measurement at AD 27

Tracking detector requirements 31

2 Particle tracking with scintillating fibers **33**
2.1 Scintillating fiber detector physics 33
2.1.1 The scintillation mechanism in organic scintillators 33
Light collection in scintillating fibers 36
Number of collected photons 38
2.1.2 Fiber arrangements 39
2.1.3 From photons to signals: the photodetectors 40
CCD (Charged Coupled Device) with light intensifier 41
MAPMT (Multi Anode Photomultipliers Tubes) 42
APD (Avalanche PhotoDiodes) 44
SiPM (Silicon PhotoMultipliers) 46
VLPC (Visible Light Photon Counters) 47
2.2 Experiments with scintillating fiber trackers 48
2.2.1 The UA2 fiber detector 49
2.2.2 The DØ Scintillating Central Fiber Tracker 50

3 Detector design and simulation **53**
3.1 FAST design 54
3.1.1 Geometrical and time constraints 54
3.1.2 The detector 55
3.1.3 The scintillating fibers 58
3.1.4 The photomultipliers 58
3.1.5 The electronics 60
The frontend 60
The readout 63
3.2 The prototype 65
3.2.1 Prototype characteristics 66
3.2.2 Tests with an electron beam 67
The Beam Test Facility beam 68
Test results 69
Efficiency 76
Crosstalk 79
Spatial resolution 81
3.3 Montecarlo simulation 84
3.3.1 Passage of particles in the fibers 86
Channel geometry 86
3.3.2 FAST tracker simulation 91

Layer geometry . . . 92
Note on hadronic interaction . . . 93
Geometrical efficiency of the tracker . . . 94

4 FAST commissioning and physics run 99
4.1 Cosmic ray data taking . . . 99
4.1.1 Final assembly . . . 100
4.1.2 Experimental setup . . . 100
Plastic scintillator counters . . . 101
Silicon detectors . . . 103
Electronics . . . 105
Analysis software . . . 105
4.1.3 Results . . . 107
Layer alignment problem . . . 107
Efficiency . . . 114
Spatial resolution . . . 116
Crosstalk . . . 120
4.1.4 The Geant simulation . . . 121
Cosmic rays . . . 121
Triangle heights . . . 122
Spatial resolution and vertex reconstruction . . . 123
4.2 September 2006 data taking . . . 130
4.2.1 Experimental setup . . . 131
The HPDs . . . 132
Expected number of events . . . 133
Vertex reconstruction . . . 135
4.2.2 The Geant simulation . . . 137
4.2.3 The beam problem . . . 139
4.3 July 2007 data taking . . . 140
4.3.1 Experimental setup . . . 140
4.3.2 The solution of the pre-bunch puzzle . . . 143

Conclusions 150

List of acronyms 153

List of figures 156

List of tables 157

Bibliography **159**

Riassunto della Tesi

All'interno del Modello Standard le simmetrie giocano un ruolo fondamentale. Anche se possono essere ben descritte da un punto di vista sperimentale, le violazioni delle tre simmetrie discrete C, P e T, rimangono non interamente collocabili all'interno del modello teorico. La lista delle domande aperte nel modello standard non si ferma qui: il problema della generazione delle masse fermioniche e della loro gerarchia e il fatto che un numero elevato di parametri liberi vadano ricavati dai dati sperimentali rappresentano ancora dei punti interrogativi.
Gli esperimenti con antiprotoni di bassa energia costituiscono, da questo punto di vista, un interessante campo di indagine. A basse energie si possono misurare piccolissime deviazioni dalle predizioni del Modello Standard e i valori delle costanti fondamentali possono essere estratti da misure su antiprotoni liberi o in stati legati. In quest'ambito, il processo di annichilazione di un antiprotone su un nucleo, per quanto difficile da rivelare, è un'arma di indagine fondamentale.
La dipendenza della sezione d'urto di annichilazione (σ_{ann}) di antiprotoni su nuclei dal numero di nucleoni fu misurata presso LEAR (Low Energy Antiproton Ring, CERN) negli anni '80 (principalmente dalla collaborazione OBELIX): nel range di momento da 200 MeV/c a 800 MeV/c, risultò $\sigma_{ann} \propto A^{\nu}$ con $\nu \approx 2/3$ (A massa atomica del bersaglio). Esperimenti successivi a minori energie ($p \lesssim 60$ MeV/c) hanno mostrato che il suo valore è costante al variare dei nuclei leggeri bersaglio utilizzati (H, D, ^{4}He). Ulteriori misure a bassa statistica su ^{20}Ne a 57 MeV/c e su ^{3}He sembrano confermare un effetto di saturazione della sezione d'urto con il numero di massa A a basse energie.
Per una comprensione più profonda della dinamica di annichilazione di antiprotoni su nuclei e, più in generale, dell'interazione forte, sono necessari ulteriori esperimenti a statistica più elevata.
Questo lavoro di tesi descrive la progettazione, la costruzione e le performance di FAST (Fiber Antiproton Scintillating Tracker), un rivelatore a fibre scintillanti per misure di sezione d'urto di annichilazione di antiprotoni su nuclei nell'ambito dell'esperimento ASACUSA presso l'Antiproton Decelerator (AD) del CERN. Il

lavoro svolto viene descritto essenzialmente nei Capitoli 3 e 4, mentre i primi due hanno carattere introduttivo.
Nel primo Capitolo, dopo una breve introduzione storica e teorica sulla fisica degli antiprotoni (con uno specifico interesse per le misure di sezione d'urto di annichilazione), vengono presentati alcuni degli esperimenti che, fin dagli anni '60 a BNL (Brookhaven National Laboratories) e a LEAR (Low Energy Antiproton Ring) presso il CERN, hanno contribuito in modo significativo allo studio della dinamica dell'interazione nucleone-antinucleone ($\bar{N}N$), e quindi dell'annichilazione.
Il Capitolo 2 è dedicato ad alcune considerazioni in merito al tracciamento di particelle cariche con fibre scintillanti. In una prima parte viene presentata la fisica alla base del processo di scintillazione, in particolare per quanto riguarda gli scintillatori organici di cui le fibre scintillanti sono costituite. Successivamente viene considerato l'intero processo che porta alla formazione di un segnale elettrico in seguito al passaggio di una particella all'interno di una fibra: dalla produzione della luce di scintillazione alla sua raccolta, dal trasporto all'interno della fibra fino alla sua conversione in segnale elettrico per mezzo degli opportuni fotoconvertitori. Questi ultimi vengono descritti in modo approfondito, presentando le diverse tipologie di strumenti che attualmente possono essere utilizzate allo scopo.
Il terzo e il quarto Capitolo rappresentano il cuore della tesi. Lo scopo di FAST è quello di tracciare i pioni carichi ($\pi^{\pm}$) provenienti da annichilazione di antiprotoni su protoni/neutroni di nuclei di varia natura per contare i vertici di annichilazione sul bersaglio distinguendoli dagli eventi sulle pareti e di fondo in generale.
FAST consiste di 6 strati concentrici (geometria cilindrica) di fibre scintillanti di 1 mm di diametro organizzate in 2 shell cilindrici di raggio 12.2 cm e 15.6 cm. Ogni shell è a sua volta costituito da tre strati di fibre, uno assiale (parallelo alla direzione del fascio) e due stereo (a $\pm 20°$). Il passaggio della particella genera un hit in ognuno dei layer creando dei tripletti di hit che permettono di trovare il punto di intersezione.
FAST deve operare con il fascio di antiprotoni di AD, cioè un fascio emesso in bunch da 50 ns (FWHM) circa 6 volte ogni 100 s, ciascuno con un'intensità di $\sim 10^6$ particelle. Per ogni bunch circa ~10 annichilazioni (con una media di 3 tracce per annichilazione) sono attese sul bersaglio; l'unico modo per assegnare le tracce a un vertice consiste nell'assegnare ad ogni hit un time tag, cioè l'istante di tempo a cui è avvenuto l'evento. La scelta delle fibre scintillanti lette da fotomoltiplicatori multianodo è stata dettata proprio dalla necessità di avere un sistema veloce con una risoluzione temporale di qualche nanosecondo. Dal punto di vista della risoluzione spaziale invece, le richieste sono meno spinte (dell'ordine di qualche mm in entrambe le coordinate).

La validazione del disegno e delle possibili performance di FAST è stata effettuata tramite la realizzazione di un prototipo costituito dalle stesse fibre del rivelatore finale nella stessa configurazione geometrica (1 strato assiale e due strati stereo) e dalla stessa elettronica (sia di frontend che di lettura). Il prototipo è stato testato presso la Beam Test Facility dei Laboratori Nazionali di Frascati. Sia il prototipo che il rivelatore finali sono stati simulati tramite Geant3 (capitolo 3): la simulazione Montecarlo riproduce la geometria completa del rivelatore e hanno permesso lo studio della risposta analogica delle fibre oltre che della capacità di ricostruire un vertice.
Il Capitolo 4 è dedicato principalmente alla fase di commissioning di FAST e alle problematiche relative alle prime due prese dati (2006 e 2007) presso AD.
L'assemblaggio finale di FAST è avvenuto presso il CERN nell'Agosto del 2006. Per circa un mese sono stati acquisiti dati con i raggi cosmici in modo da caratterizzare il funzionamento del rivelatore; la risoluzione spaziale è stata misurata tramite un tracciatore al silicio di riferimento. Durante questa fase si sono riscontrati alcuni problemi dovuti principalmente alla fase di montaggio; alcuni di essi sono stati risolti grazie proprio a questa fase di presa dati con i raggi cosmici e al confronto con la simulazione.
In seguito il rivelatore è stato installato presso l'area sperimentale dell'esperimento ASACUSA in AD dove si è effettuata la presa dati 2006. I problemi del fascio di antiprotoni (sia di dimensione che temporali) non hanno però permesso l'acquisizione di dati utili al calcolo della sezione d'urto.
Nel 2007 un'altra presa dati era pianificata e si è da poco conclusa. Il problema al fascio dell'anno precedente è stato risolto e i primi eventi di annichilazione sono stati ricostruiti da FAST. L'analisi dati è al momento in corso.
L'idea di realizzare un tracciatore a fibre scintillanti per ricostruire tracce tramite il time tagging si è dimostrata un'idea vincente; l'elettronica di frontend e di readout permettono non solo la possibilità di acquisire eventi di annichilazione di antiprotoni da 5 MeV ma anche, con un upgrade limitato, di antiprotoni da 1 keV, come previsto in una delle prossime fasi di run di AD. Lo studio dettagliato del detector tramite i raggi cosmici e questa prima presa dati ha permesso di evidenziare dei problemi di costruzione meccanica, che andranno risolti nel prossimo futuro. Inoltre, i problemi connessi con il fascio di antiprotoni hanno dimostrato come sia necessario ideare un monitor di fascio che semplifichi il settaggio della linea e permetta di capire come il fascio stesso possa essere utilizzato per una misura di sezione d'urto.

Introduction

In modern physics (and in particular in the SM - *Standard Model*) symmetries play an important and central role. It is rather unsatisfactory that within the SM the physical origin of the observed breaking of discrete symmetries in weak interactions (P, T and CP) remains unrevealed, although the experimental findings can be well described. Moreover, there are conservation laws which are not so well "physically" understood, as there is no known symmetry from which they could be derived.
The list of open questions goes on with the hierarchy of the fundamental fermion masses, the number of fundamental particle generations, the fact that the electroweak SM has a large number of free parameters that have to be extracted from the experimental data.
Effects in speculative models (that include new particles, leptoquarks, supersymmetries, supergravity, etc.) can be searched by means of high energy accelerator experiments where, for example, new particles can be directly produced. On the other side, at low energy, small deviations from the accurate predictions within the SM can be looked for in precision experiments.
Low energy antiprotons offer excellent opportunities from this point of view. Known interactions can be tested and fundamental constants can be extracted from accurate measurements on free antiprotons and in bound states. One of the most interesting processes in this field is the annihilation of an antiproton on nuclei.
The annihilation cross section of antiprotons (σ_{ann}) on nuclei has been studied and measured at LEAR (Low Energy Antiproton Ring, CERN) in the '80s and '90s (mainly by the OBELIX experiment): its dependence from the atomic mass number A of the target nucleus, for an antiproton momentum range of 200 MeV/c–800 MeV/c, was found to be $\sigma_{ann} \propto A^{\nu}$ where $\nu \simeq 2/3$.
Recent measurements, with antiproton beams below 60 MeV/c, have shown an anomalous behaviour when compared with the high energy data: the annihilation cross section seems to have comparable values for different A. This has been

confirmed by successive low statistics measurements of low energy antiproton annihilation on ^{20}Ne and ^{3}He, confirming a saturation effect of σ_{ann} with the atomic mass number of the targets with decreasing antiproton momentum.
In order to understand this behaviour and, in general, to study deeply the strong interaction, new measurements are needed at higher statistics and with heavier nuclei.
This thesis work presents the project, the assembly and the testing phases of FAST (Fiber Antiproton Scintillating Tracker), a scintillating fiber detector for antiproton annihilation cross section measurements within the ASACUSA experiment at AD (Antiproton Decelerator, CERN). The work is mainly described in Chapters 3 and 4, while Chapter 1 and Chapter 2 have an introductory purpose.
In the first Chapter, after a brief historical and theoretical introduction on antiproton physics (focusing on the annihilation process), an overview of the most important experiments that, from the '50s up to now, provided significative contributions to the study of the antinucleon–nucleon interaction dynamics, will be presented.
Chapter 2 is dedicated to the charged particle tracking by means of scintillating fiber detectors. In the first part the physics of scintillators will be presented, in particular of plastic scintillators (that are the basic material in scintillating fibers). The whole process of charged particles detection in fibers will then be analyzed, from their passage through the fiber to the signal formation and acquisition by means of suitable photodetectors.
Chapter 3 and Chapter 4 represent the heart of this thesis work. The FAST goal is to track charged pions originated in $\overline{p}$ annihilations on the protons/neutrons of different nuclei (in gaseous and solid targets) in order to reconstruct (and count) annihilation vertices and distinguish them from background events (in most of the cases annihilations on the detector walls).
FAST consists of 6 cylindrical layers of 1 mm diameter scintillating fibers placed in a double-shell structure whose average radii are 12.2 cm and 15.6 cm. Each shell is made of three layers, one parallel to the incident beam direction (longitudinal layer) and two stereo ones (angle of ±20°). At the detector center cylindrical aluminum vessels filled with gases or with a solid thin target (in the middle of the vessel) can be placed. When an annihilation occurs within the sensitive region of the detector, the charged particles hit all the layers and two main triplets (one per shell corresponding to the hit in each of the fiber layer of the shell) can be identified allowing the reconstruction of the annihilation vertex position.
FAST has to cope with the AD beam which is ejected (at the experimental line) in ~50 ns (FWHM) bunches 6 times every ~110 s. Each bunch has ~10^6 antiprotons and the expected number of annihilations in the target is of the order of 10 (with

an average number of tracks per annihilation of 3). The only way to assign the tracks to a vertex is to time tag each hit, that is to assign to each hit the time at which it took place. The choice of a system consisting of scintillating fibers with multianode photomultiplier readout was driven by the necessity of a fast system, allowing a time resolution of a few ns. As far as the spatial resolution is concerned, the margins are not so tight (of the order of a few mm).
The validation of the design and of the detector performances have been carried out building a prototype with the same fibers of FAST arranged in the same geometry and with the same readout electronics. The prototype has been tested at the Beam Test Facility at LNF (Laboratori Nazionali di Frascati).
The detector and the prototype have been simulated with the Geant3 simulation toolkit (Chapter 3): the simulation reproduces the whole geometry of the detector and allowed the study of the analog response of the fibers as well as the vertex reconstruction capabilities.
Chapter 4 is dedicated to the commissioning phase of FAST with cosmic rays and to the problems faced during the first two data taking periods (2006 and 2007) at AD.
The final assembly of FAST took place at CERN in August 2006; a 1 month cosmic ray acquisition allowed the characterization of the detector behaviour. The spatial resolution has been measured by means of a silicon tracker. During this period some problems, mainly due to the assembly phase, became evident. Some of them have been solved thanks to the cosmic ray run itself and to the simulation.
The detector has been installed in the experimental area of the ASACUSA experiment at AD in September 2006. The antiproton beam characteristics (both in size and in time) were unexpected and this prevented any physics useful data to be collected.
The second data taking period (planned for July 2007) has just ended. The beam problems have been solved and the first annihilation events have been reconstructed. The analysis is ongoing.

Chapter 1

Antiproton annihilation cross section

In this Chapter, after having introduced a few historical notes and some considerations about annihilation processes in hadron physics, an overview of the antiproton factories from the past up to now will be given together with the techniques that brought to the modern antiproton beams (mostly based on [1, 2]).
Some of the most significative experiments in this physics field will be then shortly reviewed. In the last part of the Chapter the specific physics topic of the antiproton annihilation cross section on nuclei will be presented together with the motivation presented in 2004 for a new experiment at the CERN Antiproton Decelerator, which is the subject of this thesis work.

1.1 Historical introduction

Antimatter discovery

The concept of "antimatter" was put forth by Dirac who wrote down his new equation for the electron in 1927; even if for several years Dirac tried to explain the extra components of the solutions as the proton, indeed positively charged and 2000 times heavier than the electron, he actually arrived to the prediction of an "antimatter" counterpart of the electron initially called "anti-electron" [3].
The idea of solutions which represent "anti-particles" may be generalized to the sector of strong interactions: thus, for any hadron with mass m, charge Q and spin J, there exists an antiparticle with the same mass m, spin J and opposite charge $-Q$.
The discovery of the positron in cosmic ray events provided a strong confirmation of Dirac's hypothesis [4].
Searches for the $\overline{p}$, the antiparticle corresponding to the proton p, were performed

using data from cloud chambers and photographic emulsions exposed to cosmic rays [5, 6, 7]. Some events were seen and they were consistent with a $\overline{p}$ formation, but it was not possible to give a conclusive interpretation. The first decisive evidence for the existence of the antiproton was obtained at the Berkeley Bevatron in 1955; in these experiments measurements of the velocity, the momentum, as well as the sign and the magnitude of the electric charge of the antiproton, were performed [8]. It was confirmed (to within a few %) that the mass of the $\overline{p}$ was the same as that of the proton.
One year later the experimental proof of the existence of the antineutron $\overline{n}$ was found [9].

Antiprotons and *CPT* invariance

The antiproton search was immediately involved in a fundamental physics context: while the positron had been clearly identified many years before as the charge conjugate of the electron, it was still possible to question the assumption that the proton was a fundamental Dirac particle at all; its magnetic moment suggested that the Dirac equation might not give a complete description of it.
At the same time there were two other far-reaching developments in physics: the observation of parity violation in weak interactions and the establishment of the *CPT* theorem as the most fundamental among discrete symmetries.
In the late '50s it became evident that the parity (P) violation experiments carried out by C. S. Wu and her colleagues in December 1956 [10] had also invalidated C invariance as a general property of all interactions [11], although no conclusion could be drawn at the time about the invariance or violation of the T symmetry.
From considerations on all the data available from the early antiproton experiments, physicists were able to establish the equality of the antiproton and proton masses at the 2% level; also a lower limit on the antiproton lifetime of 10^{-7} s could be computed [12]. As a comparison, the masses of positive and negative muons were equal to ~0.1% and lifetimes to ~1% [13].
Given that C and P violations occurred in one-part-in-10^7 (in the characteristic scale of weak interactions), the question was the following: if C invariance breaks down, how could the equality of the masses and lifetimes of any particle/antiparticle pair be maintained?
The *CPT* theorem clarified all these matters; in fact it had been shown to represent the minimal set of conditions for the existence of any relativistic field theory consistent with both quantum mechanics and special relativity [14, 15].
Although C invariance was at the time accepted as the reason for the very existence

of antiparticles, what became apparent was that *CPT* invariance alone [16, 17], and not the stronger condition of *C* invariance, was sufficient to guarantee the equality of the masses, lifetimes, charges, spins and magnetic moments of particle antiparticle pairs, although not in general for branching ratios. Indeed the equal masses and lifetimes of lepton–antilepton and baryon–antibaryon pairs could be interpreted as experimental checks on the weaker but more general *CPT* symmetry.
The discovery of antiprotons was therefore not only a new and direct confirmation of the Dirac equation, but an implicit challenge to experimental physicists to probe the foundations of modern physics still further by comparing its properties with those of the proton.

Antiproton annihilation

Annihilation is one of the most interesting processes of the low energy hadron physics since matter undergoes the transition from its baryonic structure to a new one consisting of only charged and neutral mesons [18, 19, 20].
As partially introduced, the historical background of QED resulted in a description of the antinucleon-nucleon ($\bar{N}N$) annihilation process similar to the positron-electron one, that is a short range process mediated by baryon exchange.
Today a valid alternative is offered by the quark models (that will be shortly discussed later on), which describe the annihilation as a "quark rearrangement" in analogy with rearrangement collisions in atomic and molecular physics. This replaced the concept of a "true" annihilation of all the incoming quarks and antiquarks.
Before describing the most important experiments on this topic of modern and past physics, a presentation of the antiproton machines that have been developed since the 50's until AD (Antiproton Decelerator) at CERN was built (Sec. 1.3) will be given.

1.2 Antiproton factories

High precision experiments on any particle (or atom) require it to be both isolated and at rest. Isolation from the perturbing effects of collisions is an obvious prerequisite to any close study of a given particle, while the state of rest in the laboratory is, in general, the only condition under which the particle can be kept under observation for long periods.
For electrons and protons these conditions can be best approached by confining

them in potential wells in the form of electromagnetic field configurations that pull the electrical charge of these particles toward some central point or region of stability; such configurations are known as *charged-particle traps*. Even when these two particles are bound together as in a hydrogen atom, achieving the highest precision in atomic spectroscopy requires that this atom is kept still in a laser beam, either by the use of *neutral-atom traps* that pull the electron magnetic moment (and therefore the whole atom) to a central equilibrium point, or by confining the atoms in a cold atomic beam that stays within the region covered by a collinear laser probe.
Precision studies of the antiproton and the positron and of their bound state, the antihydrogen atom, clearly require to aim at the same ideal conditions of rest and isolation. Not only the problem of isolation is increased considerably by the phenomenon of annihilation, but the state of rest is itself far more difficult to reach since both particles must necessarily be produced from high energy sources.
The problem is reduced to some extent for the antiproton, as its negative charge allows it to be confined very easily in the potential well surrounding the ordinary atomic nuclei. Such natural occurring traps are more commonly known as *exotic atoms*. They are very easily formed but they preserve the antiprotons from annihilation only for a short time.
The possibility of achieving the ideal conditions described above, or at least of approaching them, has been a technical challenge; the first problems to be addressed are:

- How to produce antiprotons and collect a sample of them.
- How to bring this sample to rest, given that any production mechanism provides at least a kinetic energy of 1 GeV.
- How to isolate the sample from ordinary matter.

In the following, the first two items will be briefly addressed. Since the third one mainly concerns spectroscopy experiments, it will not be treated in this work.

1.2.1 Producing and accumulating antiprotons

Production methods

The Berkeley Bevatron, which produced the first handful of antiprotons, was completed in 1954 and allowed a maximum proton kinetic energy of 6.2 GeV.
At threshold, by definition, antiprotons are produced at rest in the center-of-mass system and the conservation of the nucleon number further requires two new proton masses to be added to the two old ones. The laboratory threshold energy for

producing antiprotons by directing a proton beam onto a stationary proton target is then exactly $6m_p$ (where m_p is the proton mass, 938.28 MeV/c^2), as these four equal mass particles must each emerge in the laboratory with one quarter of the beam momentum. In fact, the target used in the experiment of antiproton discovery by Chamberlain and his collaborators [8] was not hydrogen but copper, so that the Fermi motion of protons within the target nuclei reduced the threshold.
In order to produce antiprotons in large numbers it would obviously be necessary to go far above threshold. Under such conditions, the antiprotons, no longer at rest in the center-of-mass system, would be boosted by the Lorentz transformation to laboratory energies far beyond the threshold value of around 1 GeV and be taken still further away from the ideal condition of rest necessary for precision measurements.
Several sources of antiprotons have come and gone since 1954. Among them, the one at CERN may serve as an example. With a momentum of 26 GeV/c and a proton beam intensity of the order of 10^{13} s^{-1}, the CERN proton synchrotron (PS) can produce antiprotons abundantly enough for typical high energy particle physics experiments, in which the cross sections to be studied are of the order of μb or nb; experiments below the 1 GeV threshold energy will be discussed in detail afterwards.
The beam from the CERN proton synchrotron is extracted onto an iridium target, typically a cylinder with a diameter of 3 mm and a length of 50 mm, embedded in graphite. The primary proton beam is focused on both planes by optical elements to form an image inside the target cylinder that matches its size and shape as far as possible. The primary beam emittance[1] will limit the overall emittance of the secondary (antiproton) beam, usually required to be as small as possible. In the ideal case the target should be long enough with respect to the collision length L_{coll} to make sure that the protons interact, but short compared with the absorption length L_{abs} for antiprotons, so that most of the antiprotons will leave the cylinder. As $L_{coll} \approx L_{abs} = 50$ mm for iridium, the goal will normally be to produce an antiproton beam by using a 50 mm long cylinder. The emerging antiprotons must then be collected by another double-focusing element. Among the various possibilities, magnetic horns are usually preferred since robustness, ease of repair and simplicity are the fundamental considerations. When this is not so, lithium lenses and active (or current-carrying) targets may be used, resulting in yields that

[1] The beam emittance is the phase-space volume occupied by beam particles and it is measured in units of mm×rad; its physical meaning is correlated with the "parallelism" of the beam; for example lenses can focus a beam, reducing its size while increasing its angular spread, but cannot change the total emittance that is conserved.

are 20-40% higher.
The usable antiproton intensity is limited by several factors, including the acceptable thermal shock to the target produced by the proton beam. For the maximum allowable target temperature (about 1500 °C), the proton pulse intensity delivered to a 1 mm^2 area must be less than $\sim 6\times10^{14}$ particles per GeV/c. For a 26 GeV/c starting beam (the CERN case) it corresponds to 2.5×10^{13} protons: in Fig. 1.1 the yield is computed as a function of the antiproton collection momentum [21].
The yields are normalized to their value at the 3.5 GeV/c maximum, and show a

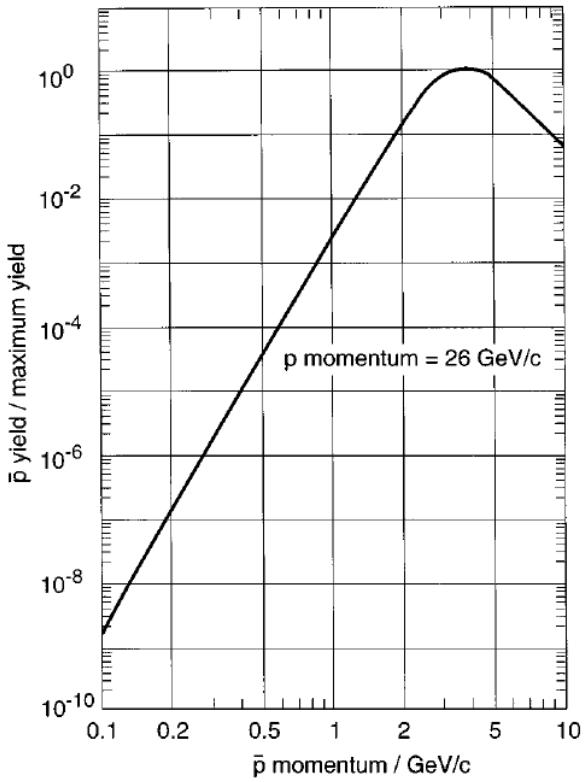

Figure 1.1: Normalized antiproton yield (antiprotons per proton) with a 26 GeV/c proton beam momentum. The normalization is chosen so that the yield is one at maximum. The true yield depends on the collection system and the acceptances of the antiproton channel: for example, with the collection system used in the AC, the measured yield at 3.5 GeV/c was $3.5\times10^{-6}\bar{p}s/p$ [21].

very steep falloff on either side, so it is important not to stay far from this value. The position of the maximum of the antiproton yield varies with the incoming

proton beam momentum as shown in Fig. 1.2.
The other antiproton facility at Fermilab (see Fig. 1.3), with a proton beam energy

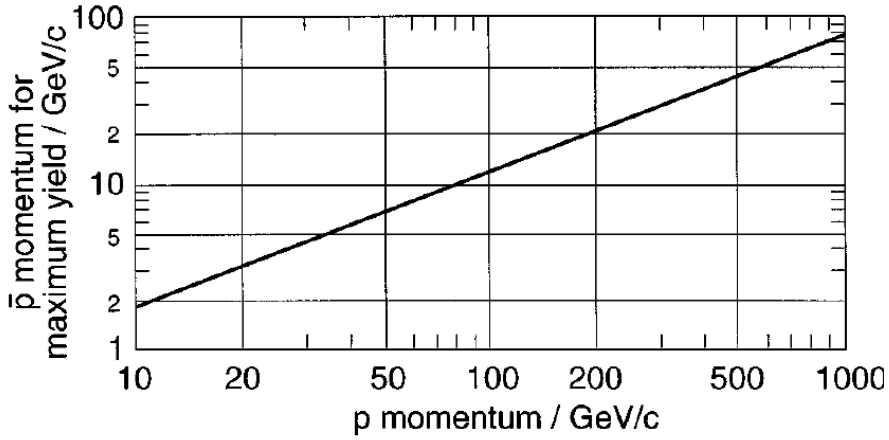

Figure 1.2: Antiproton momentum for maximum yield vs. incident proton momentum [1].

of 120 GeV/c, has a momentum at the maximum yield of ~9 GeV/c. Although the production cross section is 20 times larger, the yield (antiprotons per proton) is only four times higher than at CERN, largely due to the target heating limitation mentioned above.

Accumulating antiprotons

Since the early days, the difficulty of working with antiprotons was increased by the large number of pions and other negatively charged particles that were produced in the target along with the antiprotons. Until the early 1970s all $\bar{p}$ beams were therefore "unseparated", that is to say that they were usually π^- beams in which the antiprotons constituted a small background. Electrostatic separators, which work by deflecting particles of equal momentum but different mass when they pass between the plates of a condenser, certainly improved the background problem, but what was really needed was a technique for collecting antiprotons produced near the momentum of maximum yield over an extended period, without also collecting particles of other types.
This need was eventually fulfilled by the advent of the beam cooling techniques that culminated in the discovery of the W and Z bosons at the CERN 300 GeV

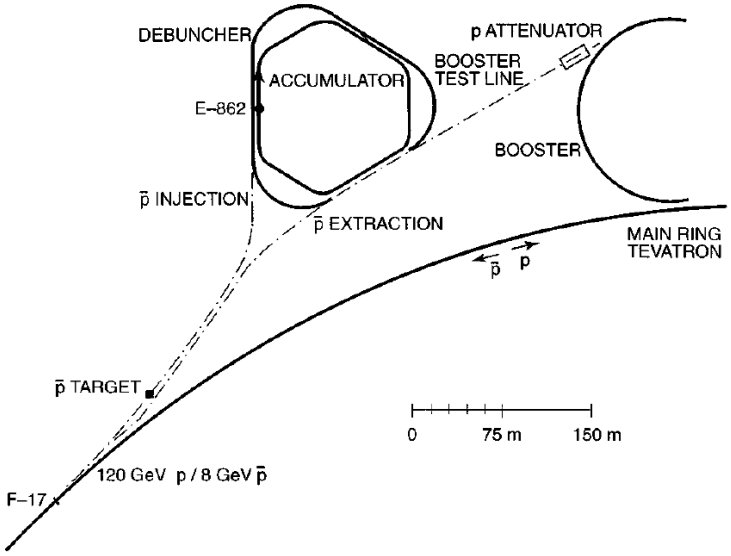

Figure 1.3: The FNAL antiproton factory [1].

proton-antiproton collider ($Sp\bar{p}S$) in 1983. The array of machines assembled for this purpose (Fig. 1.4) exemplifies most of the features of a typical modern antiproton "factory".

W and *Z* experiments needed an enormous amount of particles that was achieved accumulating in the Antiproton Collector (AC) many successive pulses prior to acceleration to 300 GeV. Stochastic cooling [22] avoids some relevant phase-space constraints[2] by the application of repeated corrections to the particles orbits in the storage rings by means of signals from pickup electrodes that sense their mean deviation from the ideal orbit.

The final element required for the *Z* and *W* experiments was the AC, a supplementary storage ring concentric to the AA; this was added in 1983 [24].

1.2.2 Decelerating antiprotons

It has been discussed how the needs of high energy experiments with antiprotons have been fulfilled since their discovery in 1955, while the requirements of experi-

[2]The horizontal and vertical Antiproton Accumulator acceptances were both of the order of $100\times\pi$ mm$\times$mrad, and its momentum acceptance $\Delta p/p$ was 0.7%. The single pulse yield of about 10^7 antiprotons from the target station occupied about 50% of this phase space volume, while the *W* and *Z* experiments required building an AA stack containing several times 10^{11} particles [23].

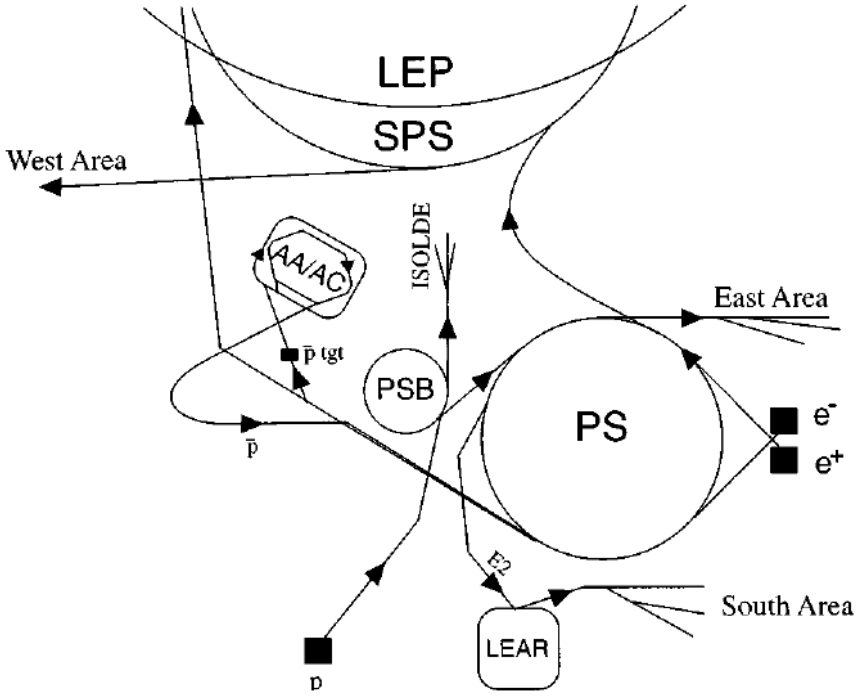

Figure 1.4: The CERN antiproton factory (not to scale) up to late 1990s. Also e^+ and e^- sources, the Large Electron-Positron collider (LEP) and the Super Proton Synchrotron (SPS) are shown. The Antiproton Collector (AC) ring is the outer of the two concentric storage rings labelled AA (Antiproton Accumulator) and AC (Antiproton Collector). PSB is the Proton Synchrotron (PS) Booster ring.

ments with antiprotons at very low energies have always been rather incidental to these purposes.

From GeV to MeV

The condition that the phase-space volume occupied by a collection of particles remains constant (better known as *Liouville condition*) is true only at constant momentum; if the particles undergo deceleration, the theorem ensures that this volume will increase with the inverse third power of momentum [21].
The solution of this problem has come from phase-space cooling. It was quickly realized that the rapid phase-space blowup that inevitably would accompany deceleration below the 3.5 GeV/c AA/AC storage momentum could be compensated

by cooling the beam pulse at one or more intermediate momenta.
This led to the adaption of the AA cooling techniques to a new storage ring, LEAR (Low-Energy Antiproton Ring) that allowed to obtain the most important results of the CERN 300 GeV $p\bar{p}$ collider for low antiproton studies.

LEAR

This machine survived the $Sp\bar{p}S$ itself for many years. The sequence of the events to decelerate antiprotons was the following: it began with the return from the AA to the proton synchrotron, approximately once every 30 minutes, of bunches containing a few 10^9 particles and extracted from the 3.5 GeV/c 10^{12}-strong AA stack [25]. In the proton synchrotron they were decelerated to 0.6 GeV/c before being transferred to the LEAR ring (Fig. 1.5), where cooling was applied after successive deceleration to three or four intermediate momenta. At and below 300 MeV/c, the electron cooling technique was found to be more efficient than stochastic cooling and permitted energies as low as 2 MeV (momentum ~ 61 MeV/c).
In the electron cooling the antiprotons transfer energy by collisions to a velocity matched (comoving) electron beam; this, being continuously refilled with cold electrons from its source, carries off the protons surplus relative energy into the electron-beam dump. A final application of cooling at the extraction momentum compressed the beam phase space to the emittance required in the external beamlines[3]. In addition to these deceleration capabilities, LEAR could also re-accelerate the 600 MeV/c antiprotons to 1.6 GeV/c.
LEAR was formally closed in December 1996, after fourteen years of service. The space of the former AC ring (Fig. 1.4) is now occupied by **AD** (Antiproton Decelerator). Its characteristics will be discussed in detail in Section 1.3.

Decelerating below 1 MeV

A practical lower limit for the standard deceleration techniques previously used in LEAR, and now used in AD, is approximately 5 MeV (it corresponds to a momentum of 100 MeV/c). Although several methods are available for reaching the practical upper limit of electromagnetic trap structures (50-100 keV), they are often less than ideal for all purposes, and the choice among them is usually made according to the way the antiprotons will be used at the lower energy.
Some of these methods are:

[3]Typical 106 MeV/c (6.0 MeV) beamline values were 1π mm$\times$mrad and $\Delta p/p$=5$\times 10^{-4}$.

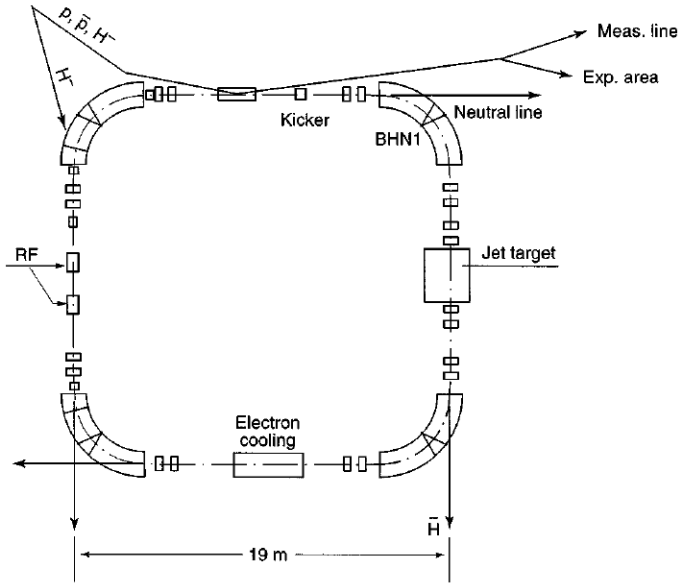

Figure 1.5: The CERN Low-Energy Antiproton Ring (LEAR). For most experiments, the antiproton beams were sent to the experimental hall on the right. For the antihydrogen experiments, the internal circulating beam was used with a xenon gas jet target in the indicated position.

- Passive energy dissipation.
  It consists of slowing down particles by passage through thin foils and/or gases without any attempt to compensate the inevitable effects of multiple scattering and energy spread; the annihilation and loss of energy in the degrader material typically deflect the particle phase space outside the detector acceptance downstream to the degrader so that they become unusable. The main reason why such disadvantages do not prevent the use of passive degradation is that many studies of very low energy antiprotons require few particles.

- The cyclotron trap ("anticyclotron").
  The so called "cyclotron trap" [26] developed for studies of exotic atoms, has in addition provided many data on the stopping power of gases in this energy region. This device is a cyclotron operating in inverse (i.e. decelerating) mode. However, the deceleration is not produced by a radiofrequency electric field, but by dissipative forces in a low pressure gas introduced into

what would, in a normal cyclotron, be the vacuum chamber.
In such a device antiprotons can be injected at 100-300 MeV/c of momentum and extracted at lower energies up to the eV-scale needed for the formation of exotic atoms.

- Radio-frequency quadrupoles.
  A third technique for decelerating antiprotons below a few MeV of kinetic energy is based on the radio-frequency quadrupole (RFQ) [27]. Electric quadrupole fields, unlike their magnetic counterparts, develop deflecting forces that do not depend on the particle velocity and therefore they are effective for particles down to zero kinetic energy. Thus a dc voltage applied to four hyperbolic-section electrodes arranged as in Fig. 1.6 produce central restoring forces (i.e. linearly increasing with increasing distance from the symmetry axis) on particles moving at any speed in the z direction.

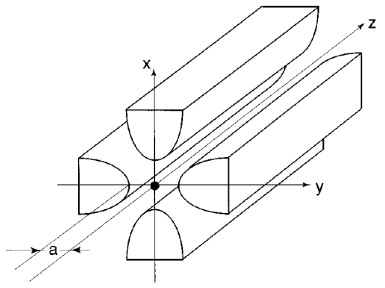

Figure 1.6: Principles of a Radio-Frequency Quadrupole (RFQ). A voltage $+V_0/2\sin(wt)$ is applied to the two electrodes on the z axis, a voltage $-V_0/2\sin(wt)$ to the electrodes on the y axis.

1.3 The Antiproton Decelerator

The Antiproton Decelerator (AD) at CERN (Fig. 1.7) was successfully commissioned, starting in 1998 [28] and it has been operating for physics since 2000. A first four-month particle physics run took place from July to October 2000 followed by a second run, which started after the shutdown of the CERN machines at the end of April 2001. Almost 90% of the equipment has been taken from the AC (target area, injection/ejection lines, hall, magnets, power supplies, radio-frequencies,

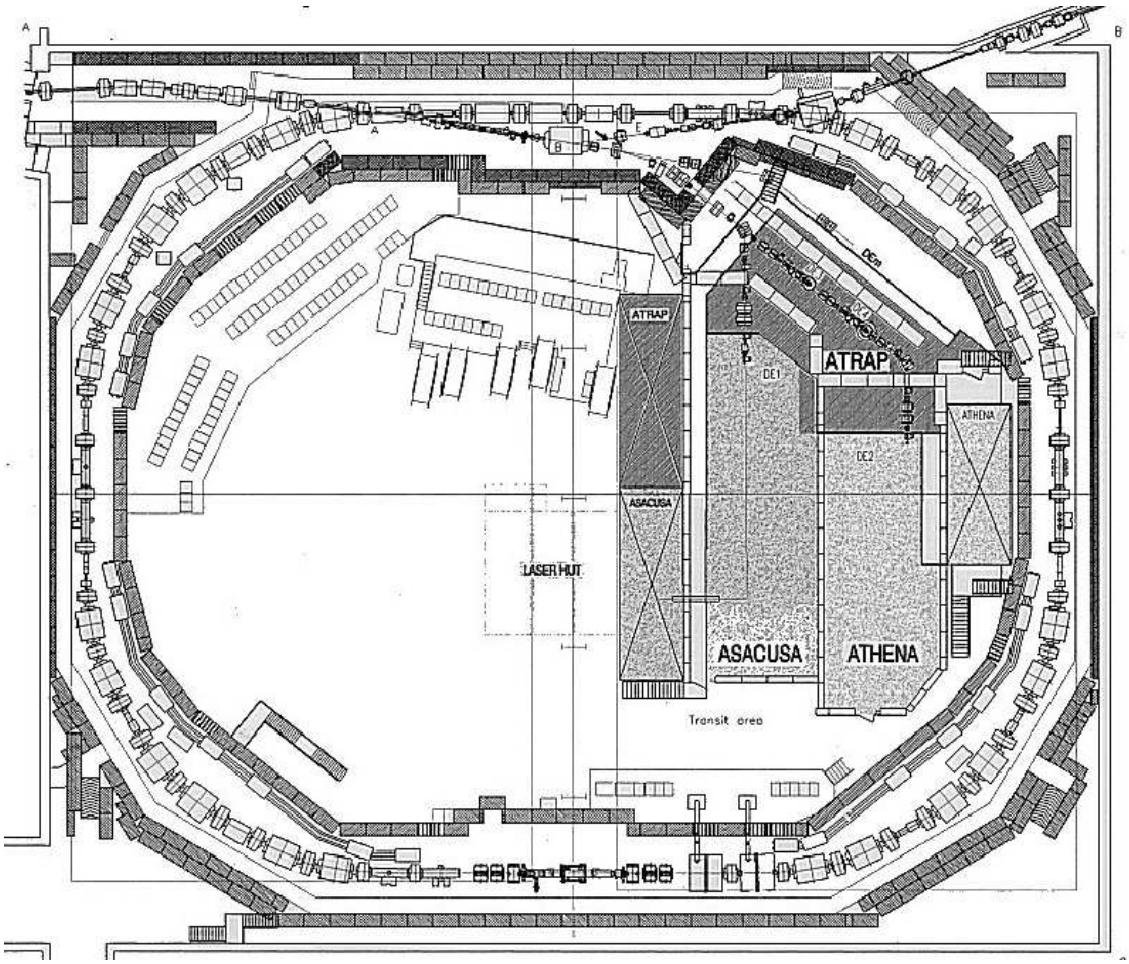

Figure 1.7: AD experimental hall. The ejection lines correspond to the three experiments ATRAP, ALPHA (formerly ATHENA) and ASACUSA.

stochastic cooling, diagnostics...). Some components came from LEAR (electron cooling, additional supplies and beam line equipments) and from the AA. Compared to the scheme used until 1996 which needed four machines (AC, AA, PS and LEAR) to provide low-energy antiproton beams, AD has brought considerable savings in operational costs and manpower [29].

Deceleration cycle

In Fig. 1.8 the deceleration cycle of AD is shown.
Antiprotons are produced in a target by the 26 GeV/c proton beam from the CERN

PS, then collected and transferred to the AD ring. After injection at 3.57 GeV/c, antiprotons are rotated of 90° in the longitudinal phase-space (precooling), taking advantage of the large AD momentum acceptance and short bunch length of about 25 ns. Then the beam is stochastically cooled and decelerated down to 2 GeV/c. Stochastic cooling is repeated again, mainly to reduce the momentum spread to fit the requirements of the deceleration RF cavity. The beam is then decelerated

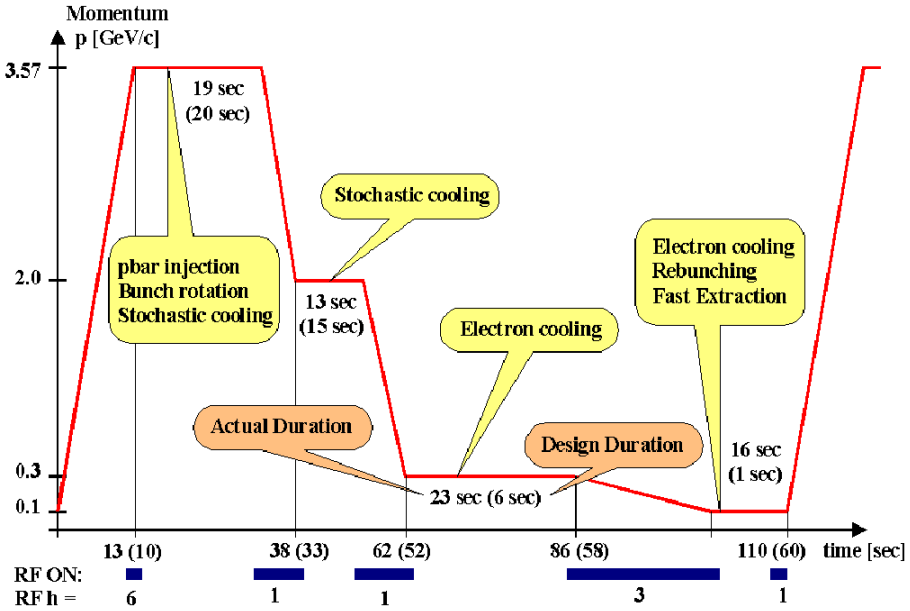

Figure 1.8: AD deceleration cycle. It is also shown in parenthesis the duration of the steps in the design program.

down to 300 MeV/c and cooled down by the electron beam from the electron cooler (*electron cooling*). After cooling the beam is decelerated to the ejection momentum of 100 MeV/c (corresponding to a kinetic energy of 5.3 MeV). Then the antiprotons are cooled again by the electron beam, rotated of 90° in the longitudinal phase space (if experiments demand a shorter beam, which is typically the case) and ejected [30].
The beam at 5.3 MeV (100 MeV/c) is routinely delivered to the three experiments (ALPHA, ATRAP and ASACUSA) every ~110 s.

Multiple extraction

When the antiprotons are within the main ring, they can be captured into several buckets which are kicked out individually [29]. This "multiple extraction" is the way the AD beam has been operated in the annihilation cross section experiment subject of this thesis work.

1.4 Annihilation cross section experiments

In the following a short review of the past and present experiments on antiproton annihilation physics will be given. The corresponding results will be summarized in the next section.

Early experiments

The two first experiments, both with bubble chambers, were carried out at BNL (Brookhaven National Laboratories) and at CERN.
The CERN bubble chamber was ~72 dm^3 of sensitive volume and placed into a magnetic field of 2.1 T. The antiprotons with a momentum of 700 MeV/c were moderated by a Cu degrader and then sent into the target within the chamber. Even if the magnetic field and the target itself caused a spreading of the beam, applying suitable cuts on the path lengths of the antiprotons, the system was set to achieve 3 or 4 annihilations for each expansion of the chamber so that stereoscopic pictures of annihilation events were taken. Then, scanning the obtained films, a three-dimensional reconstruction was performed with a 80 μm precision and the momenta of charged particles were given by their curvature due to the magnetic field. The achieved momentum resolution was about ~3%.
During these years (from the 50's to the 70's) a lot of data were collected (exceeding the scanning capabilities of that time); anyway most of $\bar{p}p$ annihilation aspects were investigated (meson production and frequencies, X-rays produced in annihilation, etc.)

The KEK detector

The KEK (High Energy Accelerator Research Organization, Tsukuba, Japan) 12 GeV proton synchrotron provided an antiproton beam of 580 MeV/c of momentum. The KEK detector (Fig. 1.9) consisted in a liquid molecular hydrogen target surrounded by scintillation counter hodoscopes and a tracking system with cylindrical and

planar multiwire proportional chambers for a solid angle coverage of ~93%. The antiproton beam passed through a graphite degrader and then was stopped in the target. The photons were detected by a NaI crystal calorimeter surrounded by

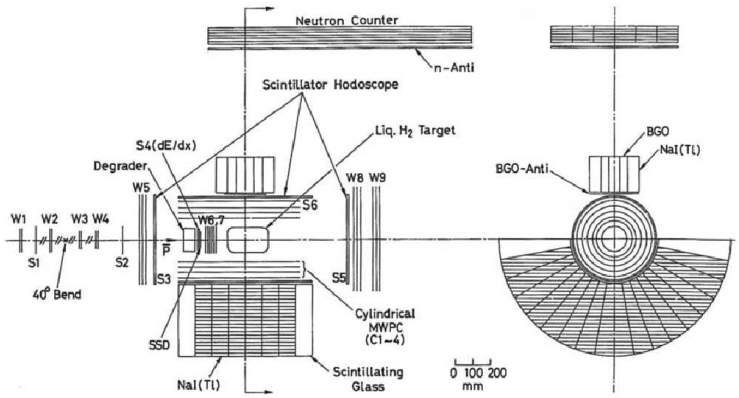

Figure 1.9: Side and back views of the KEK detector [18].

scintillating glass modules.
An event was recorded when the detector indicated the antiproton incidence on the target and one or two photons were detected by the NaI scintillators.

1.4.1 The LEAR experiments

A real step forward in antiproton physics was done when the cooled antiprotons became available in the '80s at LEAR. In addition to the already discussed technical details (see Sec. 1.2), it should be remarked that the LEAR beam had a small physical size and a narrow momentum spread ($\Delta p/p$ ~0.1%). For low momentum antiprotons this meant a very small stopping region in liquid H_2 and D_2 targets, allowing at the same time the use of gaseous targets. The typical beam intensities ranged from 10^4 to 10^6 $\bar{p}$s per second, with a beam purity of 100%.
At LEAR three main experiments were carried out:

- ASTERIX;
- OBELIX;
- Crystal Barrel (CBAR).

ASTERIX (PS171)

The early experiments with bubble chambers used liquid H_2 and D_2 in which annihilations occur at rest; in fact, the annihilation is preceded by the capture of an antiproton by a hydrogen (or deuterium) atom.
The ASTERIX experiment was designed to study $\overline{p}p$ annihilations by stopping the antiprotons in a H_2 gas target at room temperature and pressure and observing the emitted X-ray spectrum.
The detector, situated in a homogeneous magnetic field of 0.8 T, consisted mainly in the following elements (see Fig. 1.10):

- a gas target whose volume (length 45 cm, radius 7 cm) was large enough to contain the full distribution of $\overline{p}$ annihilations at an incident particle momentum of 105 MeV/c;

- a X-ray drift chamber, placed around the target vessel, used to improve the tracking capability and for the particle identification by means of the dE/dX distribution. The achieved energy resolution was as good as 20% for 8 keV X-rays and π/K mesons were distinguished up to 400 MeV/c of momentum;

- a set of 7 multiwire proportional chambers allowed charged particle tracking achieving, for $\overline{p}p \to \pi^+\pi^-$ events at 928 MeV/c[4], a 3% momentum resolution;

- the interaction point of photons was reconstructed by means of a lead foil (1 radiation length) in front of the outer chambers;

- the two endcap detectors made of three wire planes with cathode readout on both sides. This gave a large angle coverage. Moreover, the endcap detectors were used for γ identification but not for the reconstruction of charged particle tracks.

A "long track" criterion, that is two long tracks passing at least five of the wire chambers, was applied and gave the optimum momentum resolution. The so collected data were of the order of 10^6 events; with less stringent constraints, that is without the triggering on X-rays, the number was twice this value.

[4]For the two body decay, each pion has a total energy of a proton mass (m_p = 938.3 MeV/c). Thus its momentum is $p_\pi = \sqrt{m_p^2 - m_\pi^2} \simeq$928 MeV/c.

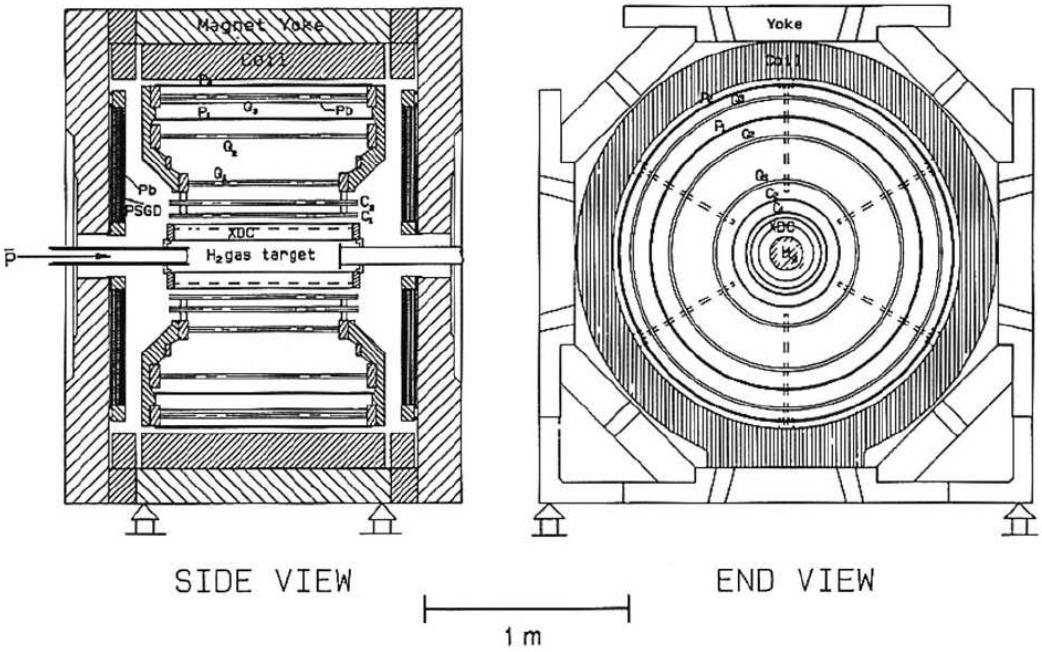

Figure 1.10: Two schematical views of the ASTERIX detector.

OBELIX (PS 201)

The OBELIX detector consisted in an inner structure of four sub-detectors placed inside a 0.5 T field. In Fig. 1.11 a view of the detector is shown; the sub-detectors (labelled 2-4, 3, 5 and 6) were the following:

- a spiral projection chamber (SPC) that allowed a three-dimensional imaging of the annihilation vertices as well as of the X-rays. Also the angular correlation between X-rays and annihilation products was measured;
- a time of flight (TOF) system made of two coaxial barrels of plastic scintillators which consisted in 30 tiles whose distance from the beam axis ranged from 18 cm to 136 cm. The achieved time resolution was as good as 800 ps (FWHM);
- the charged particle tracking and identification was achieved by means of a jet drifted chamber (JDC) that measured the dE/dX with 3280 wires with flash ADCs readout. The intrinsic spatial resolution was 12 mm as far as the z coordinate is concerned and 200 μm for the ϕ one. The momentum resolution (for monoenergetic pions at 928 MeV/c, that is from the two body decay) was 3.5%;

- a calorimeter made of four modules. Each module consisted in layers made of 3×4 m^2, 3 mm thick lead foils (converters) with planes of limited streamer tubes as active elements. The whole system, called high angular resolution gamma detector (HARGD), counted twenty converter layers for a total width of 10 radiation lengths. Thanks to the energetic resolution of the HARGD, a good reconstruction of the final states was achieved. For example, the mass of the π_0 was reconstructed with a resolution of 10 MeV/c^2. As far as the efficiency is concerned, the obtained values were between 15% and 25% (depending on the momentum).

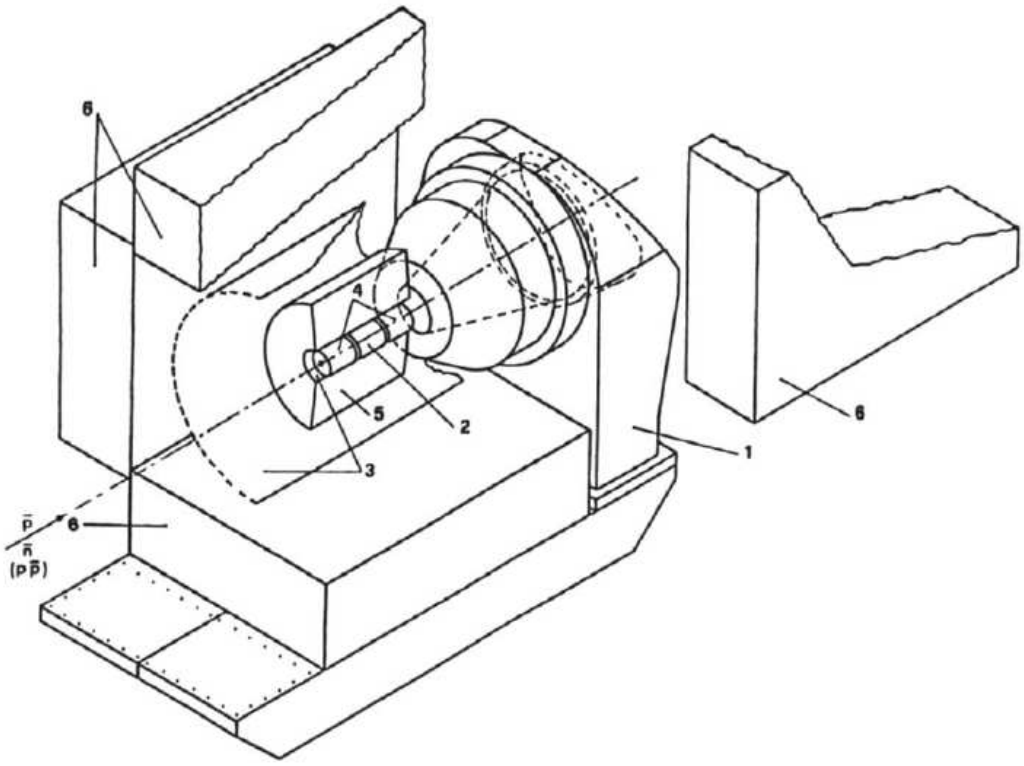

Figure 1.11: Scheme of the OBELIX detector [18]. The labels indicate the axial field magnet (1), the SPS (2,4), the TOF (3), the JDC (5) and the HARGD (6).

The OBELIX detector was used with several targets: liquid H_2 and D_2, gaseous H_2 at room temperature and with pressures ranging from 30 mbar up to 1 bar. Placing a further H_2 liquid target 2 m upstream from the main detector allowed the production of antineutrons (through charge exchange), thus performing measurements

also for $\overline{n}n$ and $\overline{n}p$ annihilations.

Crystal Barrel (PS 197)

The Crystal Barrel (CBAR) detector is shown in Fig. 1.12. Its characteristics were studied to face two main topics: the first one was the search for glueballs (gg) and hybrid mesons ($g\bar{q}q$) produced in in-flight annihilations with protons and neutrons; the second purpose was the study of $\overline{p}p$ and $\overline{p}n$ annihilation dynamics as well as the study of radiative and rare meson decays. One of the features for which the CBAR

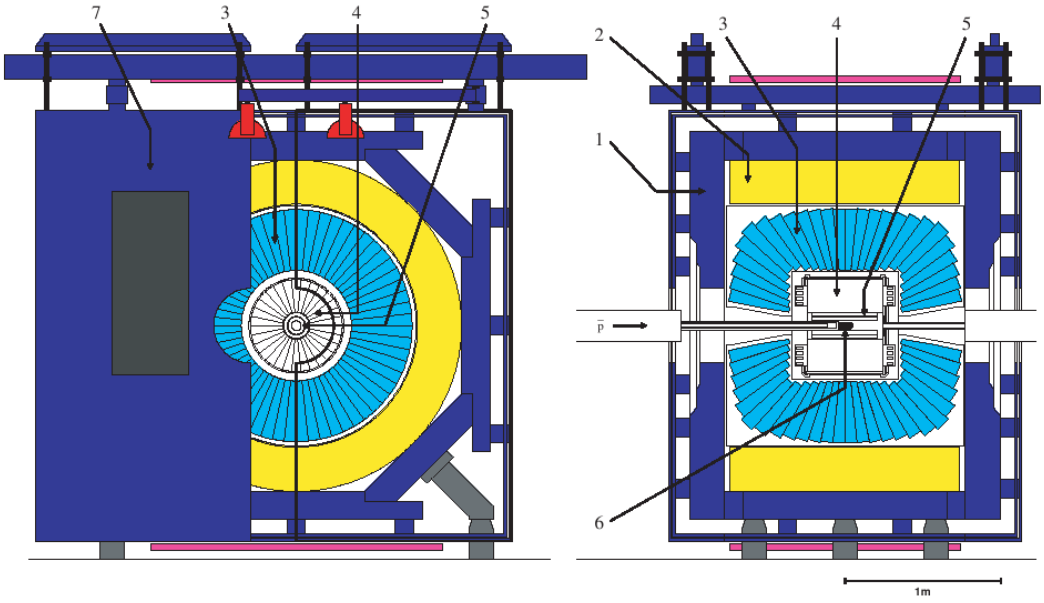

Figure 1.12: Crystal Barrel experiment detector front and side view [18]. The numbers stand for the magnet joke (1), the magnetic coils (2), the CsI barrel (3), the JDC (4), the MWPCs (5), the target (6) and one half of the endplate (7).

detector distinguished itself from the other LEAR experiments was the photon detection over a large solid angle and with a good energy resolution.
A 200 MeV/c antiproton beam stopping in a liquid hydrogen target (4 cm long) placed at the center of the detector was used. A 1.5 T solenoidal magnetic field was provided with its axis parallel to the incident beam one. The target was surrounded by two multiwire proportional chambers (MWPCs) and a cylindrical jet drift chamber (JDC); the last one consisted in 30 sectors each of them made of 23 sense wires which provided (by means of the charge sharing among the nearby

wires) the position of a track with a resolution of ~8 μm. As far as the transverse plane coordinate is concerned, the achieved resolution was 125 μm. Selecting the tracks crossing all the JDC layers, the momentum resolution for pions ranged from 2% (at 200 MeV/c) to 7% (for 1 GeV/c). Moreover, a π/K meson separation of 500 MeV/c of momentum was achieved.
A barrel shaped calorimeter consisting of 1380 CsI(Tl) crystals surrounded the JDC. Its polar angle coverage ranged from 12° to 168°, while a total one was possible for the azimuth angle, thus obtaining a total of 95%×4π for the overall shower acceptance. Photons were detected with a 1.2° spatial resolution (both angles); as far as the energy resolution is concerned, the otained value was $2.5\%/E^{1/4}$ (energy in GeV). The neutral pion mass was reconstructed with a 10 MeV/c^2 resolution.
After 1995 the MWPCs were replaced by silicon strip detectors for a total of 15 single sided layers, each made of 128 strips with a pitch of 50 μm). This naturally improved the vertex reconstruction resolution (both ϕ and z) and momentum resolution for charged pions up to 3.4% at 0.8 GeV/c and 4.2% at 1.0 GeV/c.
As already said, antiproton annihilations were studied with gaseous hydrogen too. The gas was placed within a mylar vessel (the entrance window thickness was 195 μm) at room temperature and at 12 bar of pressure; a silicon detector 55 μm thick was placed to count the incident $\overline{p}$s (the typical measured value for the liquid targets was 10^4 antiprotons per second for an incoming momentum of 200 MeV/c, while larger intensities, up to 10^6 $\overline{p}$s were available for the gaseous target and with momenta of 600–1940 MeV/c).
One important feature of the detector was a multi-level trigger system that allowed a deep study of the rare decay channels suppressing the well known (dominant) ones.

1.4.2 Overview of the LEAR results

The antiproton-nucleus annihilation rate was measured by the OBELIX experiment for low momenta down to 40 MeV/c (usually the so called low energy range refers to momenta below ~100 MeV/c, that is ~5 MeV of kinetic energy). This value is quite large if compared to the characteristic momenta in particle-antiparticle systems bound by the electromagnetic (Coulomb) force which for example, for the $\overline{p}p$ one, is of the order of 4 MeV/c. The reason is that, in this energy range, the usual Bethe's 1/v law (where v is the velocity of the interacting particle) has to be replaced by a $1/v^2$ regime. This was firstly predicted in 1948 [31] and it is a well known principle in atomic physics. But as far as nuclear physics is concerned, the electromagnetic repulsion between protons gives rise to an exponential decrease

of the interaction probability at low energy.
The OBELIX experiment deeply investigated the behaviour in such a system (i.e. with a Coulomb attraction) and the results, or, at least, some of them, were rather unexpected. Given the amount of the available data, the need of a deep theoretical nuclear physics background and the fact that it would be outside the purpose of this thesis work, only some specific data and comments will be presented. A general review of the physics results and of the inherent theoretical aspects, on nucleon-antinucleon interactions, can be found in [32, 18].
Going back to the $\overline{p}$-nucleus annihilation cross section, a naive picture of the process would suggest that the probability of its occurrence should increase with the number of the available targets in the nucleus, that is the number of nucleons. The measurements performed at LEAR on $\overline{p}$ and $\overline{n}$ annihilations on nuclei at a momentum range of 200 MeV/c–600 MeV/c confirmed this idea. The results showed that the behaviour of the annihilation cross section was given by:

$$\sigma_{ann} = \sigma_0 A^{\nu}$$

where $\nu \approx 2/3$ and A is the atomic mass number of the target nucleus (see Fig. 1.13). But at lower energies this trend is not respected. In Fig. 1.14 some results of recent (low statistics) measurements are presented. Without entering into detail, all measurements at low energy (the most important ones are reported in the STRAD experiment proposal [33]) seem to confirm the occurrence of a "saturation effect" of the annihilation rate in light nuclei. This effect has been explained by a few phenomenological models based upon optical potentials [34, 35].
Concluding, it can be said that all the authors are in agreement about the need of new measurements: higher statistics would reduce error bars on some present data that, up to now, can be interpreted in different (and sometimes discordant) ways; moreover, heavier nuclei should be used in order to probe the $A^{2/3}$ behaviour of the annihilation cross section.
For these reasons, it has been proposed a new[5] $\overline{p}$-nuclei annihilation measurement for AD at CERN that is presented in the next section.

1.4.3 Cross section measurement at AD

A cross section measurement at AD had been planned taking into consideration, first of all, the high intensity of the incoming beam. In the LEAR experiments

[5] A possible experiment has been previously proposed [33]. It consisted in a streamer chamber filled with the wanted gas (or mixture), with the gas working both as degrader for $\overline{p}$ momentum and as target. This setup could have hosted also solid targets. The detector was designed to collect a picture of in-flight annihilations as well as at rest ones.

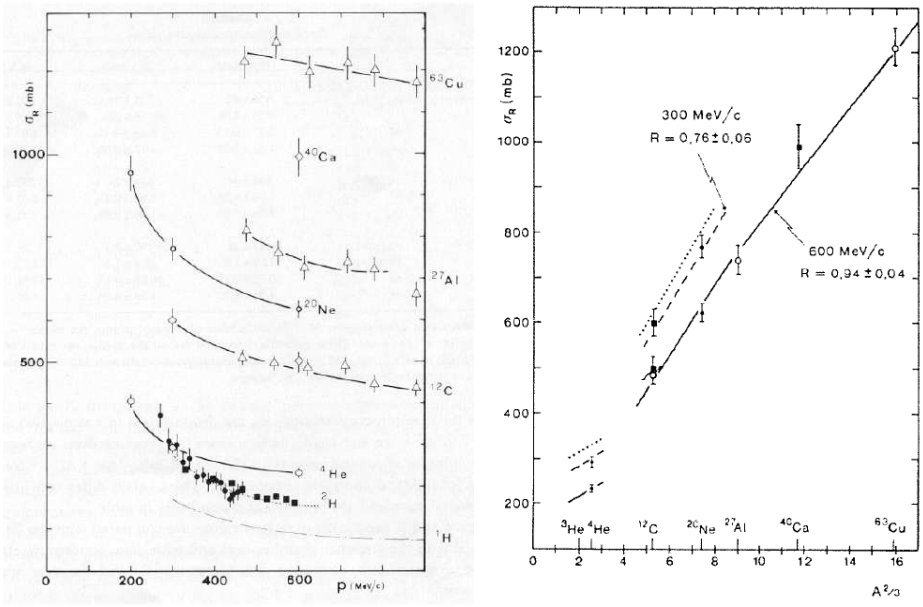

(a) (b)

Figure 1.13: (a) Comparison among the annihilation cross sections at different $\overline{p}$ momenta. (b) $\overline{p}A$ annihilation data as a function of $A^{2/3}$ at 300 MeV/c and 600 MeV/c. The lines indicate some model predictions (see the text for references). Both plots are reported in [33].

the beam was flowing almost continuously in the beam pipe and a small fraction of the antiprotons of the main ring was extracted and sent to the experimental lines; as a result, a few isolated particles reached the sensitive volumes at a (relatively) slow rate of ~10^4–10^6 $\overline{p}$/s. At AD, up to 10^6–10^7 antiprotons are packed in a ~50 ns (FWHM) bunch, that means an extremely high rate during the bunch crossing through the detector volume. This is a consequence of the main purposes for which AD has been designed, that is for spectroscopy experiments [36, 37]. In fact, given the short lifetime of some bound states formed by the antiprotons and nuclei, and given the limited power of the laser beams used to induce transitions on the so formed antiprotonic atoms, an antiproton density as high as possible was needed.
The basic idea is of a detector with cylindrical geometry placed around a vessel containing the target to which the 100 MeV/c antiprotons are sent.The vessel should be able to contain both gaseous and solid targets, giving the possibility to investigate a wide range in the A number. The detector has to detect the annihilation products

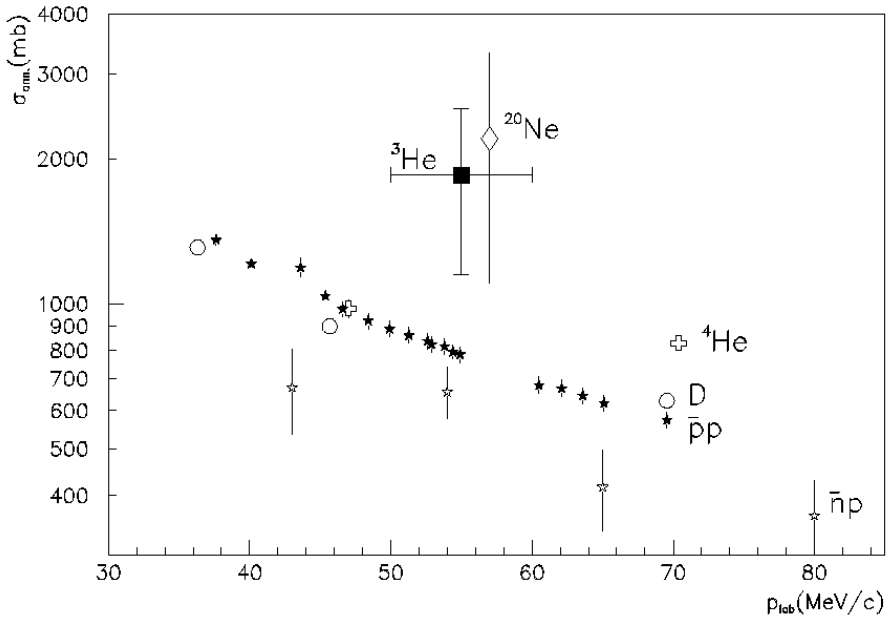

Figure 1.14: Antiproton annihilation cross section for D, ^{3}He, ^{4}He and Ne. Full and empty stars correspond, respectively, to $\overline{p}$ and $\overline{n}$ [33].

in order to count and localize the annihilation vertices. As reported in [18], the typical $\overline{p}p$ annihilation products are π-mesons (other rare events can be neglected for this experiment purposes) whose average number is $\simeq$3.1. This number has to be considered in the design phase of the detector.
The other main constraints for the geometry and for the acquisition modalities are given by the following points.

- The inner vessel containing the target should be as long as possible since the antiprotons (almost all) that do not interact with the target, will hit the endcap of the vessel itself, thus inevitably saturating the readout system with a large number of unwanted pions. Placing the sensitive volume far away from the vessel endcap will reduce this number. Anyway the annihilation events must be detected earlier than this occurs.

- For the same reason, the bunch should be as short as possible in time, even if it implies a lower interaction rate. Moreover, also the bunch size should be minimized since the beam tails could, in principle, annihilate on the beam pipe itself having the detector hit by the produced charged pions.

- Once more, the undesired pions that would impinge on the sensitive elements of the detector, do not allow the use of any beam monitor device. In fact, a huge number of antiprotons would annihilate on it.
- The solid targets have to be as thin as possible (low pressures in the gaseous target case) in order to avoid beam divergence to increase and thus making its tails hit the vessel walls. Once more, this would also decrease the number of annihilation events.
- The incoming particles cannot be counted. In principle, a beam monitor can be placed near the detector in order to detect the pions produced when the bunch reaches the endcap of the vessel. Anyway, the high intensity of these events prevent any high sensitive detector to be used, thus only integration measurements can be performed, limiting the accuracy in case of the absolute cross section measurements.

In order to cope with these constraints, the setup shown in Fig. 1.15 has been proposed. A tracking detector with a cylindrical geometry is placed around an inner region in which the target will be located. The tracker is able to detect the charged pions originated by the $\bar{p}p$ annihilations and to reconstruct the vertex position. As far as the target type is concerned, two possibilities have been studied (and effectively put into operation).

- **Gaseous target** (Fig. 1.15 TOP). The vessel consists in a unique tank that is filled with the chosen gas. A dedicated (and compact) gas control unit can provide a wide range of pressures (from 1 mbar to 1 bar) together with a fast gas replacing capability. In this case the vessel is isolated from the beam pipe; this implies that the antiprotons, before reaching the sensitive volume, must cross the exit window of the AD beam pipe (70 μm of Kapton) and the 50 μm entrance window of the vessel (as well as the air between them). This causes a beam divergence spreading and also some annihilation events that should be taken into account.
- **Solid target** (Fig. 1.15 BOTTOM). In this case a ultra-high vacuum pipe, with its valve and pumping system, is hosted within the tracking detector. The main difference from the previous case is that the antiprotons, with this system, do not meet any obstacle in their path towards the target. The target element is sputtered on a thin (0.9 μm, which is the thinnest foil usable in practice) diskette of mylar placed at the desired z position within the vessel. When the antiprotons cross the target (a few hundreds of nm of material) one or very few annihilations are expected to occur.

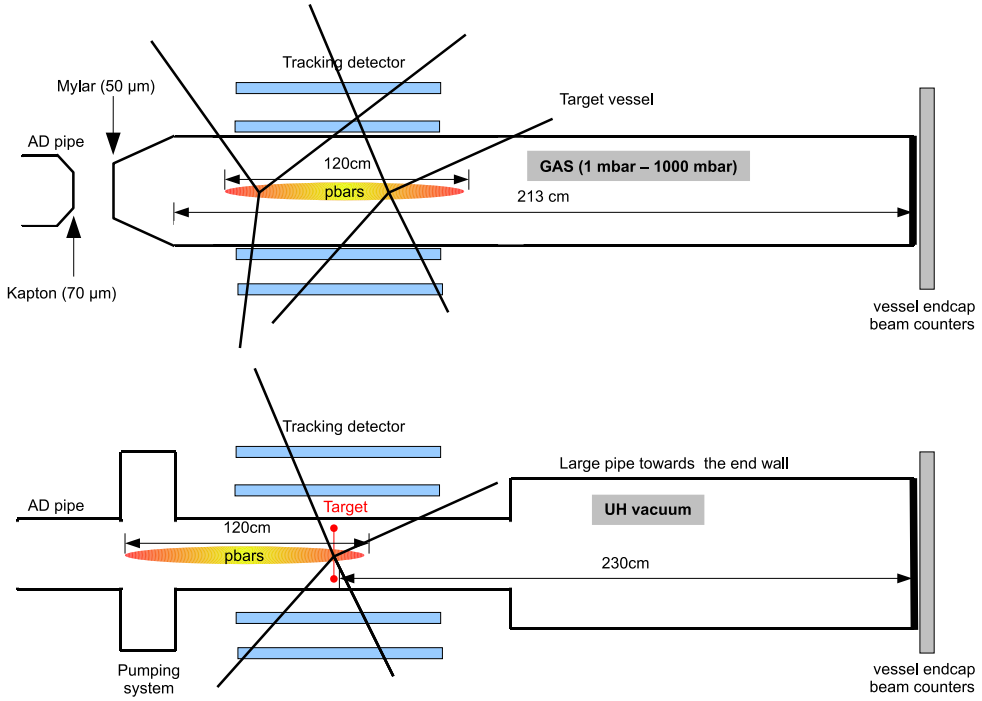

Figure 1.15: Proposed detector setup for the $\bar{p}p$ annihilation cross section measurements at AD. (a) Gaseous target case. (b) Solid target case.

In both cases, a high dynamic range detector is placed at the vessel endcap in order to monitor the incoming antiproton multiplicity and the time structure of the beam. It must be remarked that the measurement strongly depends on the bunch length: if the antiproton cloud is too long the early tails would strike the vessel endcap just as the core of the bunch is crossing the target, thus completely saturating the detector while the annihilation events are occurring. Since antiprotons move at ~3 cm/ns, a bunch FWHM greater than ~80-90 ns would be critical.
Given the problem in the evaluation of the incoming antiproton number and given the thickness of the target and the support, the measurements can be performed in this way: for both gaseous and solid target cases, the number of detected in-flight annihilations can be compared to the known cross section of hydrogen. In fact, in the first proposed setup the available gases (D_2, ^{3}He, ^{4}He, Ne, Xe) data can be compared with hydrogen itself (H_2), while in the second one, the number of in-flight annihilations on the mylar+X (X=Ni, Sn, Pt) samples can be compared with respect to the ones on the mylar alone (since most nuclei in mylar are hydrogen).

Thus the measurements will allow to compare the cross section of hydrogen with respect to higher Z (and A) materials.

Tracking detector requirements

As already said, the annihilations under investigation (the ones in the target) must be distinguished by the (unavoidable) annihilations on the walls of the vessel and, at last, on the vessel endcap. Since these last ones cannot be suppressed without affecting the interesting events too, the measurement could not be performed with a simple "counter". This is the reason why a tracker detector is needed: annihilation vertices must be divided and classified between "in-target" and "out-target" ones. Thus a further set of constraints must be taken into consideration as far as the tracker itself is concerned:

- a space resolution of the order of 1 cm should be achieved to localize the vertex position and assign it to the target or reject it;
- a time resolution as good as possible to tag each hit on the tracker with a time as precise as possible. This is of fundamental importance because background events, most of which are annihilations on the vessel endcap, should occur later than the in-target ones;
- a good efficiency for charged pions detection to collect as many data as possible (the AD repetition rate is low);
- a low duty cycle, in fact the detector has to be active for some hundreds of ns six times every AD cycle (~2 min);
- as far as the readout time is concerned, there is no need of extremely high speed since the 6 bunches are extracted from the AD beam at a ~1 s rate;
- the detector should be easy and fast to install (several experiments are hosted in the ASACUSA experimental area in AD) and easy to operate (a small crew must operate the whole system);
- low cost.

One last consideration concerns the capability of adapting the whole system to future measurements at even lower energies with as few as possible modifications. Two experiments are foreseen: a measurement of the annihilation cross section at 5 MeV (with gaseous targets) and a second one at 1 keV (this very low energy range

can be reached by means of the RFQD system of the ASACUSA experiment). Especially in the second case, slow $\overline{p}$s exit the (further) decelerating devices randomly distributed in a few second time interval, thus the sampling gate of the detector should be increased of orders of magnitude. On the other hand, the sampling resolution can be decreased, since events are isolated in time.

Chapter 2

Particle tracking with scintillating fibers

The detector for the measurement of low energy antiproton annihilation cross sections has to be fast (because of the beam features), compact (because of the line setup) and able to reconstruct tracks in a 3D frame. As the next Chapter will describe, for all these reasons scintillating fibers readout by multianode photomultipliers have been chosen. This Chapter is dedicated to a review of the principle of light production in plastic scintillators in general and in scintillating fibers in particular. The second part of the Chapter will describe the possible layout of fiber trackers, the photodetectors and two of the experiments based on fibers for tracking.

2.1 Scintillating fiber detector physics

2.1.1 The scintillation mechanism in organic scintillators

The main component (~98% in weight) of an organic scintillator is a polymeric material such as polystyrene, polyviniltoluene (PVT) or polymethyl-methacrylate (PMMA). These materials (commonly referred to as solution), apart from giving to scintillators their optical and mechanical properties, allow the absorption of kinetic energy from ionizing particles and its consequent transfer to the so called aromatic molecules (benzene rings), which are the solute dissolved in the base material and responsible of the scintillation light emission. The energy transfer occurs via a non radiative dipole-dipole interaction known as Forster Transfer [38]. As an example, in order to excite a molecule of the polymeric material 5 eV are needed and the

transfer process has a ~3% efficiency [39].
The benzene rings are chemical structures characterized by a large number of vibrational levels for the so called π-electrons (see Fig. 2.1): these are the electrons shared by the typical 6 carbon atom ring. This delocalization of the electrons is known as *aromaticity* and gives benzene great stability. When a ionizing particle

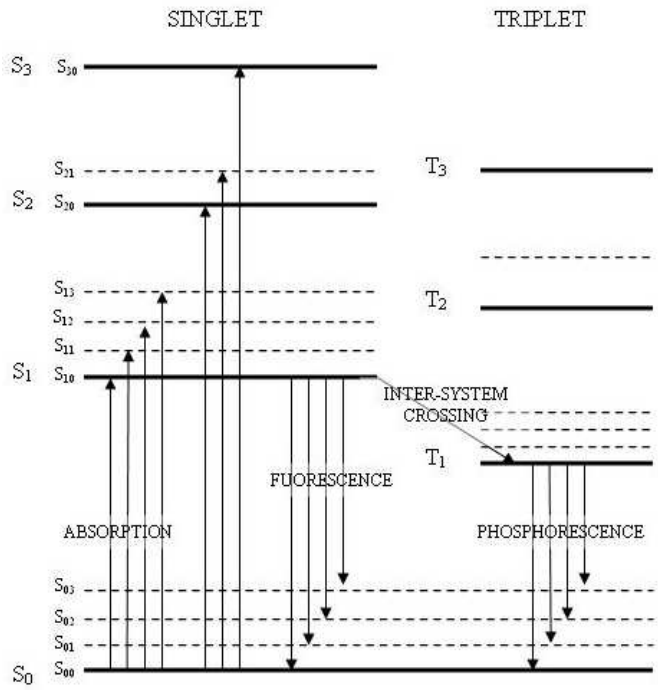

Figure 2.1: π-states in a typical organic scintillator molecule.

crosses such a material, π-electrons are likely to be excited to a higher energy level with a random vibrational state (the dashed lines in Fig. 2.1). The molecule undergoes a very fast (10^{-12} s) vibrational relaxation with the nearby molecules taking the excited electron to the lowest of the excited states from which it decays with the subsequent (a few ns) emission of a photon in the visible range; the process is known as *fluorescence*. Another phenomenon, the *phosphorescence*, is present when the first relaxation cannot occur in the same way due to forbidden states. In this cases the time scale is several orders of magnitude larger (up to hours) than in the fluorescence ones. Since fast detectors are needed, phosphorescence will not be treated in this work.
The self absorption of the fluorescence photons in the surrounding molecules is limited by the fact that their average energy is lower than the excitation energy

needed by the π-electrons in the lower energy states. This can be seen in Fig. 2.1: if an electron has been excited from the S_{00} state to one of the S_{1n}, after the vibrational relaxation it goes back first to the lowest excited state (S_{10}) and then to one of the S_{0n} emitting a photon that cannot excite another electron from a S_{00} energy level. In other words, the fluorescence photons have not enough energy to be immediately absorbed by another benzene molecule and they can travel a few mm in the material without being reabsorbed. Since for most applications the photon path from the emission point has to be larger than a few mm (depending on the scintillator size and on the way the light is readout), one more fluorescent element is needed. This component, working as a wavelength-shifter, absorbs the primary photon with a high cross-section and re-emits it with a longer wavelength. They typically can suppress the self absorption phenomenon of an order of magnitude making the attenuation length (λ_{att}) of the secondary light larger (up to several meters). In this way photons can easily reach the scintillator edge where a dedicated system collects them (see next section).
In Tab. 2.1 some physical properties of the Bicron BCF-10 scintillator (the same as the one of the fibers of this work) are presented; in Tab. 2.2 some of the most used wavelength-shifter materials are listed among which the 3HF (3-hydroxyflavone) is a good candidate for small diameter fibers since it has a very little overlapping of its emission and absorption spectra. The attenuation length decreases with the increase of the wavelength shifter material concentration; therefore, when the photon loss must be minimized due to their low number (as in small diameter fibers) higher concentrations are needed and the 3HF presents optimal characteristics (even if it has a poor quantum efficiency).

density	1.032 g·cm^{-3}
refractive index	1.58
light output	~8000 photons/MeV
rise time	0.9 ns
decay time	2.4 ns
wavelength of maximum emission (λ_{peak})	424 nm
attenuation length (λ_{att})	250 cm
H atom density	4.74×10^{22} cm^{-3}
C atom density	5.23×10^{22} cm^{-3}

Table 2.1: BCF-10 scintillator properties (Bicron datasheet).

short name	λ_{peak} (nm)	decay time (ns)	Q.E.
PBD	360	1.1	0.92
POPOP	410	1.4	0.93
bis-MSB	420	1.3	0.94
3HF	510	<1	0.36

Table 2.2: Properties of the most common wavelength shifter materials. Q.E. is the quantum efficiency, that is the ratio between the number of absorbed and emitted photons.

Light collection in scintillating fibers

Generally speaking, the light produced in a plastic scintillator undergoes reflections on the detector walls and reach the readout device (different kinds of readout systems will be reviewed later on) with a 10–20% of efficiency. This percentage, that is the collection efficiency, depends on the scintillator dimensions and geometry, on those of the photodetector window as well as its ratio with respect to the scintillator size, on the attenuation length and so on.
A scintillating fiber is made of an inner scintillator core (polystyrene) and an outer cladding region made of a material of a lower refractive index to allow light transport (Fig. 2.2). When a charged particle crosses the fiber, it releases energy along

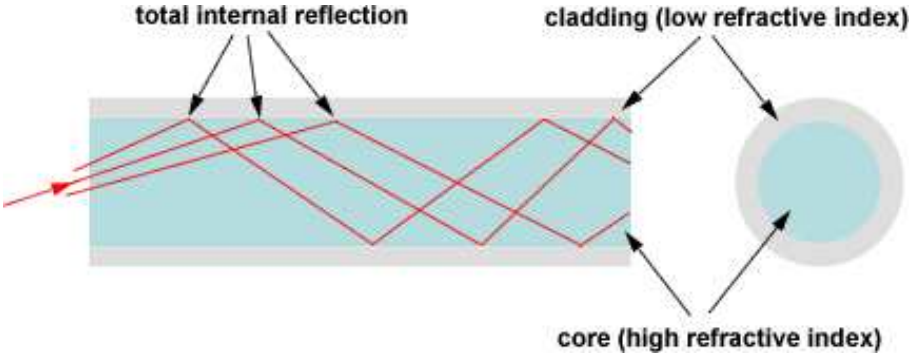

Figure 2.2: Working principle of an optical fiber. In scintillating fibers the core is made of polystyrene (n=1.59) and the cladding (typically) of PMMA (n=1.49).

its path generating isotropically the primary fluorescence photons. As already said, the second fluorescent material provides the absorption and re-emission of a wavelength-shifted light again isotropically.
The emitted light remains inside the fiber due to the total reflection (Snell's law) at

the core-cladding interface. They can be also built with two claddings in order to enhance transport efficiency (double-cladding fibers); in this case, the second external cladding has an even lower refractive index (with respect to the first internal one).
The cladding has usually a thickness of a few μm to provide the fiber its mechanical properties as well as to prevent the core from chemical attacks (from a theoretical point of view, a few wavelengths needed to contain the exponential decreasing electromagnetic wave would be enough).
When the light is emitted on the fiber axis, it is kept within the core if its emission angle α is less than $\alpha_c \equiv \pi/2\text{-}\theta_c$ (see Fig. 2.3), where θ_c is the critical angle given by Snell's law:

$$\sin\theta_c = \frac{n_{clad}}{n_{core}}$$

The light emitted outside this cone should be absorbed by an *Extra Mural Absorber*

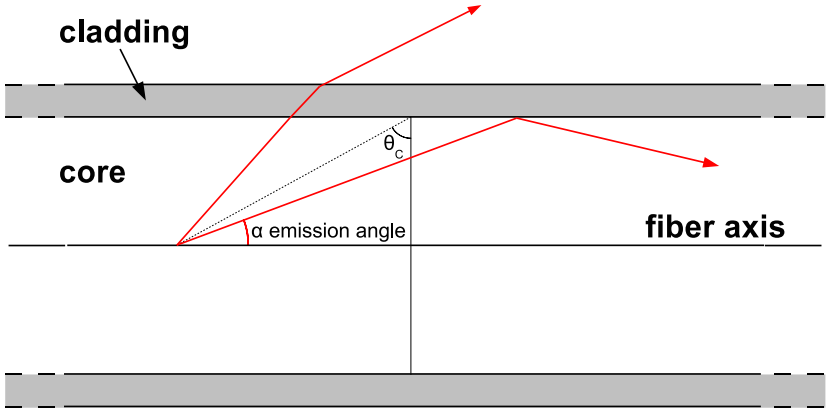

Figure 2.3: Propagation of light within a fiber. If the angle of emission $\alpha < \alpha_c = \pi/2 - \theta_c$ than the light propagates within the fiber.

(EMA) whose function is to suppress the crosstalk with the nearby fibers. The cone defines a solid angle given by $2\pi(1\text{-}\cos\alpha_c)$ so that the fraction ϵ of the light collected in the forward cone is:

$$\epsilon_{\text{fwd}} = \frac{1}{2}\left(1 - \frac{n_{clad}}{n_{core}}\right)$$

Since typical values for the involved parameters are n_{core}=1.59 and n_{clad}=1.49, $\theta_c \simeq 70°$ and $\epsilon_{\text{fwd}} \simeq 3.2\%$ (single cladding fiber), $\epsilon_{\text{fwd}} \simeq 4.9\%$ (double cladding fiber).

It must be noticed that α_c represents also the angle of the light cone emitted at the fiber exit where it should be readout.
If the photon source point is not on the fiber axis the formulas are more complex; the emitted light is described by the so called skew rays, whose helical path wound around the fiber axis. These skew rays are on the average more attenuated because of their longer path, but, on the other side, this is compensated by the larger acceptance angle. The net effect can be measured experimentally and is a ~10–30% increase in the collected light with respect to the one expected from point-like sources placed along the fiber axis [40].
Even if the particle crosses the fiber far away from its axis, the collected light does not vary so much; in fact, thanks to the skew rays, the farther from the fiber axis is the particle track, the larger is the acceptance light cone. As a result, the total light yield shows no significant dependence on the distance from the fiber axis over more than 80% of the fiber diameter.
If the fiber diameter is reduced, the light collection mechanism becomes more inefficient: if the attenuation length λ_{att} of the primary scintillation light (~0.5 mm) decreases till the value of the fiber radius r, a large fraction of it escapes from the fiber before being absorbed by the secondary fluorescent molecules; thus when $\lambda_{att} \gg r$ the collection efficiency drops from ϵ to ϵ^2. This can be avoided with a reflective layer (for example aluminum) outside the fiber cladding which reflects back the primary scintillation light within the core more and more times; obviously there are mechanical limitations to this approach, especially in small fibers.
In order to compensate the poor primary light collection in narrow fibers, it is possible to increase the secondary fluorine concentration, but also the self absorption effect increases. As a result, considering a fiber length of ~1 m and a good efficiency, the minimum diameter should be of the order of 500 μm.

Number of collected photons

Considering the data reported in Tab. 2.3 (those of the fibers used in this work), the calculation of the number of collected photons at the fiber edge per crossing m.i.p. (minimum ionizing particle) can be done as it follows.

The energy loss of a m.i.p. in polystyrene is ~2 MeV/cm [41], the mean path in the scintillating material of one particle crossing the center of the fiber is $\pi/2 \times r$ (r=500 μm is the fiber radius) that is 785 μm. Therefore a m.i.p. deposits ~157 keV in the fiber core. Given the light output of ~8000 photons per MeV, the number of generated photons in the fiber is ~1260. At last, considering the trapping efficiency ϵ_{fwd} ~5%, a total of ~63 photons is trapped in the fiber and propagates towards the

core refractive index	1.6
inner clad refractive index	1.49
outer clad refractive index	1.42
core density	1.05 g·cm^{-3}
inner clad thickness	3% of fiber Ø
outer clad thickness	1% of fiber Ø
trapping efficiency (forward) ϵ_{fwd}	~5%
light output	~8000 photons/MeV
decay time	2.7 ns
wavelength of maximum emission	432 nm
attenuation length	220 cm

Table 2.3: BCF-10 scintillating fiber properties (double cladding, 1 mm Ø - from Bicron datasheet). The core is made of polystyrene, the inner clad of Acrylic and the outer one of Fluor-Acrylic.

fiber edge (the same amount travels in the opposite direction). The blind face can be aluminized in order to enhance the light yield reflecting back the light.
Travelling from the source point z to the photodetector (z=0), the light is attenuated by a factor $\exp(-z/\lambda_{\text{att}})$, thus resulting, for 1 m long BCF-10 fibers, in a total number of photons of ~40. At the interface fiber-photodetector ~10% of the light is reflected and lost. The whole process has lead to ~35 photons reaching the photodetector.

2.1.2 Fiber arrangements

Scintillating fibers can be arranged in different ways to form the building block of a tracking detector.
The easiest way from the mechanical point of view is to place them one beside the other on the same plane, but in this geometry consistent dead areas between the fibers are present. The blind region between the cores is twice the cladding width (~50μm); moreover, when the particles cross the fiber too far from the fiber axis they don't lose enough energy to allow the photons to reach the readout face of the fiber.
A better configuration consists in the so called doublet ribbon (see Fig. 2.4(a)) in which the dead region problem is avoided because the crossed material is rather constant with the particle track position. Moreover, with this configuration and a single fiber readout, a spatial resolution better than the digital one ($\sigma = p/\sqrt{12}$ where p is the readout pitch) can be obtained. This is due to the fact that the particle

that originates a signal in two fibers is well localized in space. For example, the spatial resolution of a 830 μm diameter fibers doublet (readout pitch 415 μm) measured during the DØ detector commissioning can be as good as 100 μm [42]. It must be noticed that the spatial resolution cannot be enhanced by performing an analog readout for two reasons:

- the number of collected photons at the photodetector is usually so low that the statistical fluctuations would be the dominant effect;
- the light collection efficiency, as already said in the previous section, has a poor dependency on the track distance from the fiber axis.

Another possible arrangement is allowed by square section fibers which ensure a better coverage of the space but, as a drawback, show a poorer light transmission properties. The dead areas due to the cladding thickness can be suppressed by tilting the fiber of half a diameter length as shown in Fig. 2.4(b). These fibers

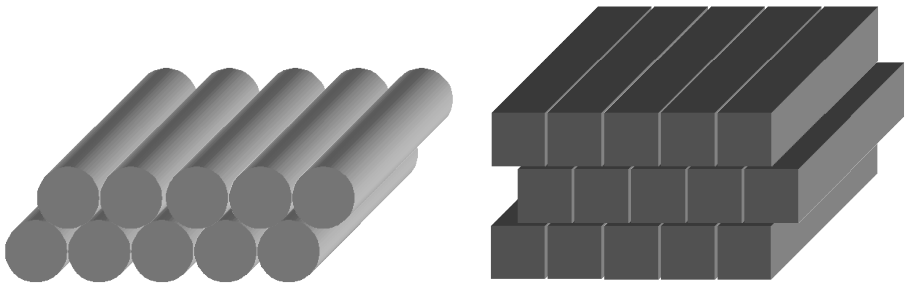

(a) (b)

Figure 2.4: Two possible fiber arrangements: (a) doublet ribbon, (b) tilted square fibers.

are indicated for multilayer detectors where high efficiency can be easily reached maintaining a good spatial resolution. With 10 layers of 500 μm square fibers and a distance between the planes of 50 μm, a resolution of 25 μm [43] has been obtained. Square fibers show a shorter attenuation length than the classical round fibers; for this reason, their use is limited to short and compact detectors (<1 m).

2.1.3 From photons to signals: the photodetectors

Only a few photons, as seen in the previous section, reach the fiber edge and are available for a conversion into a readable signal. The physical limits to this number

are difficult to overcome; since a reasonable efficiency should be always maintained, the biggest improvements in a scintillation fiber tracking system should come from the photodetectors more than from the fibers themselves. An optimal photoconverter should present the following characteristics:

- capacity to generate a signal starting from a few tens of photons without the need of preamplifiers that would increase noise;
- good spectral matching between the incoming scintillation light and its sensible window;
- a time resolution of the same order of magnitude of the fiber one, that is $\lesssim$ns;
- compactness because often the fibers must face the photodetectors in the detector area itself, thus with the minimum available space;
- limited cost.

Two classes of photodetectors can be identified with at least some of these features: vacuum based photodetectors (Photomultipliers, Micro Channel Plates), solid state ones (Avalanche Photodiodes, Visible Light Photon Counters, Silicon Photomultipliers) or hybrid ones.
In the following, a short description of each of them will be presented.

CCD (Charged Coupled Device) with light intensifier

This multichannel readout system consists in a multi-stage light intensifier with a CCD collecting the secondary light; a MCP (Micro Channel Plate) is usually inserted in the amplification chain for fast gating purposes. It is a compact system and quite cheap (considering its cost per channel). In Fig. 2.5 an example of a two stage device is shown.
The primary photocathode (light yield gain ~5) converts electrons which are accelerated and focused on a first phosphor screen connected to a second photocathode. Then the MCP multiplies (gain ~1000) photoelectrons and makes them hit a second phosphor screen after which photons are conveyed to the CCD. The light of a single fiber is readout by more than one CCD pixel (it is reasonable since this device has a low cost per channel). In such a system both the granularity of the CCD (that allows the use of small diameter fibers) and the high gain of the image intensifier contributions are exploited.
One drawback of such a system is the poor timing performances; in fact, the full frame readout of a CCD needs up to 10 ms, thus no fast signals (as a trigger one is)

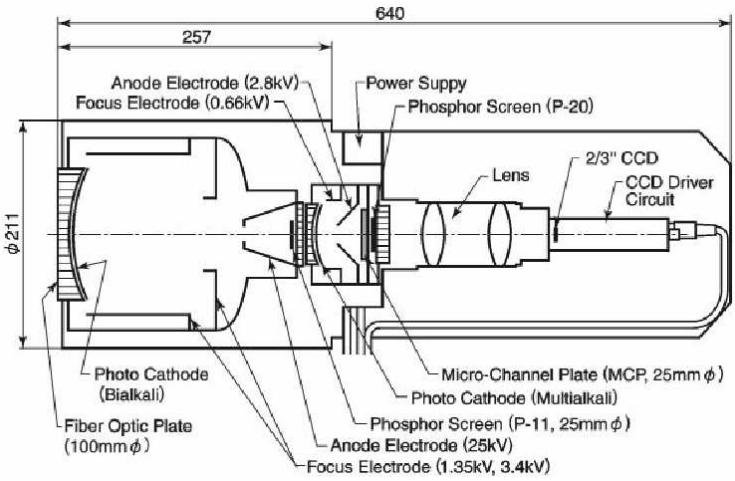

Figure 2.5: Image intensifier with CCD readout of the K2K scintillating fiber detector. This two-stage device reaches a total light yield gain of ~5000 (a factor 5 from the image intensifier while the remaining factor 1000 is provided by the MCP) [44].

are available. In any case, even when a trigger signal is externally provided, the image intensifier system has an intrinsic time resolution limit due to the phosphor decay time which is of the order of few tens of ns. For this reason the good gating capabilities of the MCP cannot be really exploited.
Another drawback is represented by strong magnetic fields that negatively affect the focusing system; anyway, if the field intensity is not too high, metal shielding is enough to have the MCPs working.
Last but not least, another limitation is given by the low radiation hardness of the CCD chips and also the worsening of the MCP performances due to age.

MAPMT (Multi Anode Photomultipliers Tubes)

While on one hand, standard photomultiplier tubes (PMT) are the most widespread readout systems for scintillation detectors, they are mechanically unfit for a fiber tracker with a large number of channels. The problem can be solved using Multi-anode PhotoMultipliers that appeared on the market in the late '80s.
A MAPMT is a single tube with a photocathode (flat in most cases), a dynode system which provides the electron multiplication and a segmented anode (Fig. 2.6). In this way the device is equivalent to many PMTs sharing the same voltage, but more compact and cost effective compared to a single PMT. As far as the performances are concerned, MAPMTs show the same characteristics of standard PMTs

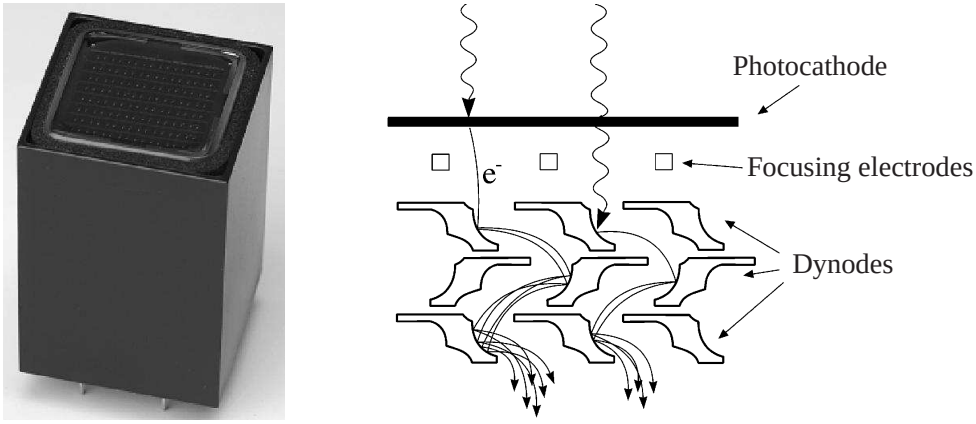

Figure 2.6: (a) Photo of the Hamamatsu H7546-series MAPMT (the same used in the FAST tracker). (b) Scheme of the multiplication process at the multianode window in a MAPMT.

(see Tab. 2.4), with the only exception of a lower gain. It should be noticed how the

number of channels	64 (8×8)
anode size	2×2 cm^2
quantum efficiency at peak wavelength	0.21
gain	3.0×10^5
anode dark current	0.2 nA
rise time	1.0 ns
transit time spread	0.3 ns

Table 2.4: Hamamatsu R7600-M64 multianode photomultiplier data [45].

need of a fast response of a fiber tracking system can be fulfilled by such a system with a dispersion on the pulse rise time better than 0.5 ns. On the other side, MAPTs present two problems: a channel by channel gain dispersion, that can be eliminated by means of a calibration and a threshold correction, and the crosstalk between nearby cathode pads. This is a non trivial issue that has created serious difficulties in the FAST commissioning phase. Three main different processes [46] give rise to the crosstalk phenomenon:

- the light exiting from one fiber can hit an adjacent cathode with respect to the one it is coupled to; it is possible because the collected photons come out

from the fiber face with a divergence (that is roughly the acceptance cone angle treated in the previous section) and also because of the presence of a finite thickness of the glass window between the fibers and the photocathodes which cannot be reduced below ~1 mm;

- since the multiplication region under the glass window cannot be physically segmented, a photoelectron extracted in one photocathode can be focused on the wrong dynode;
- for the same reason, also some of the multiplied electrons can be carried to the wrong set of dynodes resulting in a sort of charge sharing between nearby channels.

The first two effects, which are referred to as "optical crosstalk", typically give rise to a ~1 photoelectron (p.e.) false signal, thus completely indistinguishable from a true one. The third effect ("electrical crosstalk"), on the contrary, produces a much smaller electrical signal (~2% of the first ones in Hamamatsu H7546 tube). The geometry of the fiber-pad coupling deeply affects the optical crosstalk: for example, in Tab. 2.5, the data obtained lighting one channel (Hamamatsu H7546 MAPMT) with a 1 mm round fiber in the pad center are presented.

As far as magnetic fields are concerned, a μ-metal shielding is needed also for

0.11%	0.54%	0.13%
0.68%	100%	0.80%
0.11%	0.56%	0.12%

Table 2.5: Optical crosstalk measured for the Hamamatsu H7546 Multianode Photomultiplier. A single photon exits a 1 mm round fiber and enlightens the central pad (the surrounding ones are normalized to it) [46].

moderate fields since the multiplication process is very sensitive.

APD (Avalanche PhotoDiodes)

The APDs exploit the high quantum efficiency of a photodiode performing a PMT-like multiplication process.
In fact, common PMTs or image intensifiers have a quantum efficiency, in the spectral region of interest, smaller than 25%; on the other side, photodiodes, that have an intrinsic high quantum efficiency, cannot provide a suitable electronic signal (one electron-hole pair per incoming photon is generated).

In an APD (see Fig. 2.7) electron-hole pairs are generated in the depletion region; then the electrons, drifting to the high field multiplication region, start the avalanche process.

The APD can be operated in two modes: the proportional mode (gain limited to

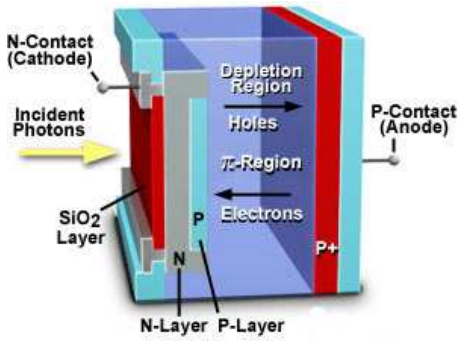

Figure 2.7: Avalanche Photodiode scheme.

a few hundreds, thus a low noise amplification is needed) and the Geiger mode. In the second case, the bias voltage is high enough to overcome the breakdown limit (typically ~200 V) and make the device enter the so called Geiger region: every electron that reaches the multiplication region generates a discharge current that lasts until the voltage drop on the bias resistor leads the APD one below the breakdown. Given the voltage drop and the APD junction capacitance, the gain of an APD operated in this way can easily reach ~10^6. One major drawback of this high gain is that the passive quenching introduces a dead time of tens of μs (it can be reduced with an active quenching).

As far as the dark count rate is concerned, it is significantly affected by temperature. At room temperature it is proportional to the device volume; considering the typical dimensions in a fiber tracking system (~1 mm fibers) and also the long dead time of an APD operated in Geiger mode, the dark count rate is too high. Cooling down the APD to ~-50°C is enough to reduce it to suitable values. On the other side, the device size can be reduced, thus reducing the dark count rate, if a light concentrator is present [47].

In principle, if the APD is operated in proportional mode, it can sustain a high count rate; anyway the cooling, since it reduces the number of phonons (phonons interactions with the electrons are responsible for their slowing down), enhances the gain. At -50°C APDs have been used, in proportional mode, for a scintillating fiber readout with a high detection efficiency [48, 49].

Further amplification can be provided by a low noise VLSI electronics but at the

expense of the timing performances of the system.
In a Geiger mode operated APD both the avalanche development and electron drift (in the depletion region electrons move at a speed of ~5 mm/ns) are fast processes; because of this fact, the rise time of the signal can be very short (~2 ns).
If many Geiger mode APDs (structured in arrays) are used on the same substrate, crosstalk can be present; in fact, the thermalization of high energy electrons (that can be generated in the avalanche process) gives rise to optical photons that can move to the adjacent APD cells. Anyway, if the distance between the pixels is increased thus losing in compactness, this phenomenon can be reduced.
As far as magnetic fields are concerned, APDs do not suffer of their presence.

SiPM (Silicon PhotoMultipliers)

Silicon PhotoMultipliers[1] are arrays of very small (~15×15 μm^2) Geiger mode APDs connected in parallel with individual quenching resistors (Fig. 2.8): in this way the total signal is the sum of all the hit pixels [50].
As already said, each pixel is an APD operating in Geiger mode. Therefore, its

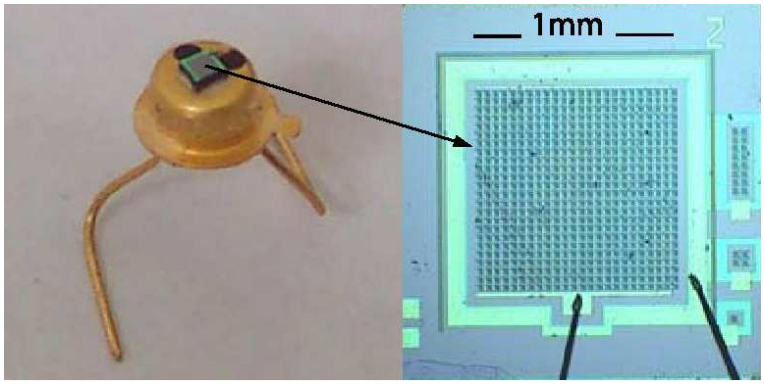

Figure 2.8: Silicon Photomultiplier photo. Each cell (pixel) works as a single APD.

signal amplitude does not depend on the number of collected photons. Each cell is a "digital" device, whose response is of the type yes/no, but the whole unit is in practice an analog detector whose dynamic range is limited by the number of pixels.
SiPMs are commonly built with an area ranging from 0.5 mm^2 to 2 mm^2 and, as far as the number of pixels is concerned, from 200 to 2000 [51, 52].

[1]This name was given by the first developers in CPTA (Center of Perspective Technologies and Apparatus, Moscow) in 1999. They are also referred to as MPPC (Multi-Pixel Photon Counter).

The single photodetection efficiency (PDE) of a SiPM is obtained multiplying the quantum efficiency by the ratio between the effective area and the total area (limited by the dead region at the pixel borders where a bias resistor of ~10 MΩ is placed). Optimized devices can reach a PDE as high as 40%.
The dark count rate at room temperature is very high (~MHz); anyway SiPMs present an advantage with respect to standard APDs: it is possible to set the threshold at a higher level (for example 1.5 p.e.) to suppress the dark count rate (if no single photon detection is needed) since the dark counts of two cells are uncorrelated.
The dead time of each cell depends on the pixel capacitance charging constant through the bias resistor; typical values are a fraction of μs. As far as the dead time of the whole SiPM is concerned, the effective value is much lower that the single pixel one because only the hit pixels are blind (this is valid if the baseline shift can be handled).
The crosstalk between two pixels occurs, at a 5% level, because of the photons generated during the avalanche [53], thus degrading the linearity of the device and increasing the dark count rate (with a 1.5 p.e. threshold). Anyway this does not represent an obstacle if SiPMs are used for a fiber system readout.
The discussed SiPM characteristics, together with some other features (sensitivity on a wide spectral range, low voltage operation, compactness, capability of working in manetic fields and low cost per channel) make them the possible choice for the next future fiber tracking detectors.

VLPC (Visible Light Photon Counters)

The VLPCs[2] consist in silicon diodes designed to convert photons into thousands of electrons through an avalanche process maintaining a high quantum efficiency [54, 55].
The photons enter the device through an antireflection coating and a transparent anode metalization (see the scheme in Fig. 2.9(a)), then an electron-hole pair is generated in the intrinsic region (which is not doped). The hole drifts until it reaches the so called gain region (high depletion) where, colliding with a neutral donor, kicks out an electron which starts an avalanche via ionization. The gain region has a high concentration (up to 10^{17} cm^{-3}) of donor atoms so that the Fermi level is only 50 meV below the conduction band. Because of this fact, only electrons undergo multiplication giving a very low gain dispersion as well as a confinement

[2]VLPCs were first developed by the Rockwell International Science Center, Thousand Oaks, USA.

of the avalanche itself. The gain saturates at a few 10^4.
VLPC is an optimal photon counter since every photon generated avalanche sums with the others, thus the output signal is a multiple of the single avalanche signal. Moreover, VLPCs show a high quantum efficiency (up to 85% at 543 nm) over all the visible light spectrum [56].
As far as timing performaces are concerned, VLPCs have demonstrated to be an almost ideal readout system for a fiber tracking device since a time resolution of the order of 1 ns can be easily obtained [57].
VLPCs must work at very low temperatures (as low as 6 K) in order to avoid thermal excitation of the impurities (the gap between the impurity band and the conduction one in the multiplication region can be as small as 50 meV) and to suppress infrared background (they are sensible up to 30 μm wavelength photons). In Fig. 2.9(b) an example of a small 4×2 array of 1 mm diameter VLPCs is shown. A large number of these sub-arrays are enclosed in a single cassette provided with a liquid cryogenic system (helium), preamplifiers and optical coupling to hundreds of fibers.
VLPCs are not affected by magnetic fields, but radiation can seriously damage them; thus they are usually placed far from the detection area. The consequent light attenuation due to the longer fibers is compensated by the high quantum efficiency of VLPCs.

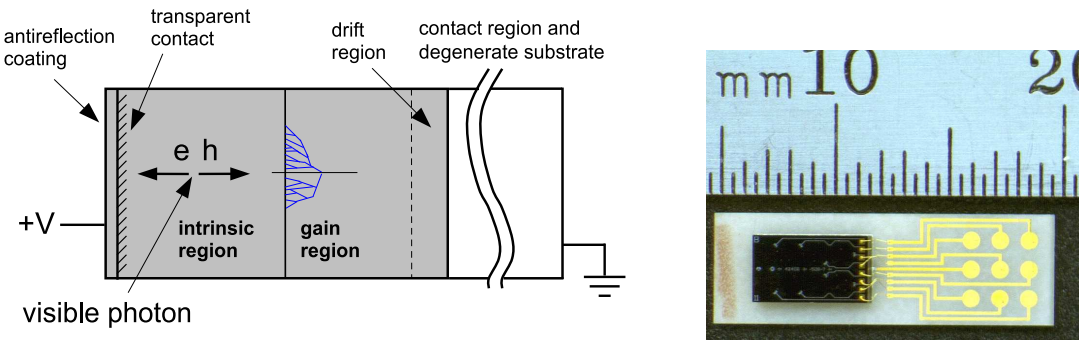

(a) (b)

Figure 2.9: (a) VLPC scheme; (b) detail of a 4×2 array of 1 mm diameter VLPCs.

2.2 Experiments with scintillating fiber trackers

In the following two large scale experiments using a scintillating fiber tracking system will be shortly reviewed:

- the UA2 Scintillating Fiber Detector, which was the first application of the scintillator fiber technology as a tracking detector;
- the DØ Central Fiber Tracker that represents the state of the art of scintillating fiber trackers (in the year 2000).

2.2.1 The UA2 fiber detector

The UA2 Scintillating Fiber Detector (SFD) has been the first relevant application of the scintillating fiber technology at the CERN SPS collider. The detector was used for the outer tracking and for the e^-/π preshower identification [58, 59, 60]. It consisted in more than 60000 fibers (diameter 1 mm) with a length of ~240 cm arranged in a cylindrical geometry (average radius 41 cm) as sketched in Fig. 2.10(a). The fibers were arranged in 24 layers: 6 stereo triplets (at 0° and ±15.8°) before a 1.5 radiation length[3] lead converter; the remaining 2 stereo triplets (placed at 0° and ±21.0°) were positioned after the converter for the preshower measurements (see Fig. 2.10(b)).

The scintillating fibers had a polystyrene core with a polyvinylacetate cladding;

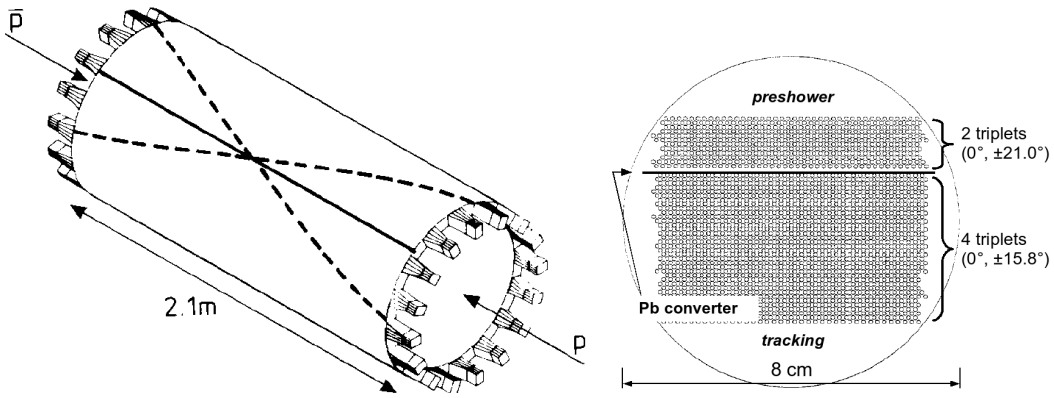

(a) (b)

Figure 2.10: UA2 Scintillating Fiber Detector. (a) Scheme of the cylindrical layers with the 32 image intensifiers with CCD readout. (b) Cross section of the layer displacement [60].

the waveshifter was a POPOP (see Tab. 2.2) and there was a sputtered aluminum

[3]The radiation length X_0 is defined as the mean path after which a high energy electron loses a 1-1/*e* fraction of its initial energy.

EMA. The collected light was readout by 32 two stage modules which consisted in an image intensifier plus a CCD. The system could be triggered at 100 kHz and the maximum readout rate was 100 Hz.
The single layer efficiency was ~91%. It was a good result considering that it was a real single layer and not a fiber doublet ribbon.
As far as the spatial resolution is concerned, a value of 350 μm was obtained: it was a bit worse than the binary one because of distorsions in the electrostatic focusing system that probably induced crosstalk [61]. If all the 18 layers of the inner tracking are considered together, a tracking efficiency of 96% with a corresponding resolution of 150 μm was obtained.
The preshower system, considering the total pulse height of the fibers after the converter, allowed a clear separation between pions and electrons (for 40 GeV particles and a detection efficiency for electrons of 98%, the achieved rejection factor was 15).

2.2.2 The DØ Scintillating Central Fiber Tracker

The Central Fiber Tracker detector has been built for the DØ experiment upgrade from the Tevatron Run II in 2002 at FNAL. The upgrade, which involved almost all the detector elements, was necessary because of the higher luminosity and the shorter bunch crossing period (from 3.5 μs to 132 ns) with respect to Run I. A new frontend electronics with bunch tagging capabilities has been developed for the calorimeter and the muon system; as far as the tracking system is concerned, a new one was needed since the momentum measurements had to cope with a 2 Tesla magnetic field, the tracking coverage had to be increased up to η=±3 (η is referred to as *pseudorapidity*[4]), the capability to extract first level trigger was to be achieved and, at last, the detector response had to be faster and without dead time [62, 63].
The tracking system of the DØ detector consists in an inner silicon tracker and the outer Central Fiber Tracker (CFT). In Fig. 2.11(a) a scheme of the detector is presented.
The CFT is made of 8 superlayers, each one made of 2 fiber doublet ribbons with *zu* and *zv* orientation (the stereo layers, usually indicated as *u* and *v*, are placed at ±3°). Each doublet consists in two layers of fibers (multicladding, diameter 830 μm) with 870 μm between one fiber and the nearby, held in place by a carbon fiber support (Fig. 2.11(b)).
The fibers are Kuraray SCSF-3HF, which are polystyrene core fibers doped with

[4]The pseudorapidity η is defined as $-\ln(\tan(\theta/2))$, where θ is the angle between the particle track and the beam direction.

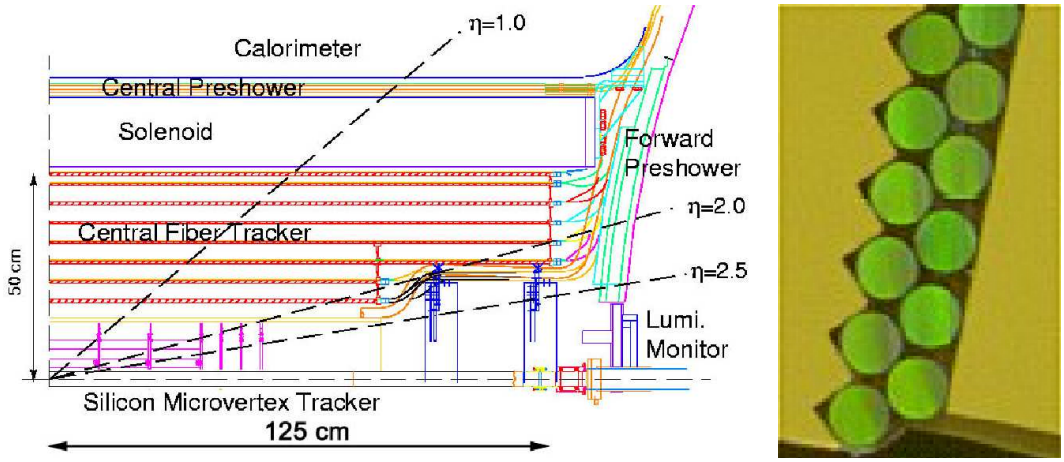

(a) (b)

Figure 2.11: (a) Scheme of the DØ detector. (b) Close-up of the carbon support with the doublet ribbon in place [64].

1.25% of p-terphenyl and 1500 ppm of 3HF (see Tab. 2.2). The low self-absorption probability of the 3HF waveshifter increases the attenuation length up to 5.5 m. This is a fundamental feature since the fibers are 1.7–2.5 m long.
The fibers are not directly readout; in fact ~11 m long clear fibers, optically coupled to the scintillating ones, carry the light to the photodetectors far away from the interaction region.
The so collected light is readout by a VLPC array (kept at 7–9 K by a liquid helium cryogenic system) for a total number of channels of 77000. The light loss in the transport is not negligible (the length of the clear fibers is comparable with their attenuation lengths of 10.5 m); in order to minimize it and to make misalignment errors negligible, the clear fibers diameter is intermediate between that of the scintillating fibers and the VLPCs (respectively 830 μm and 1 mm).
As already said, the VLPCs present a very high quantum efficiency, so that the average number of photoelectrons collected by the fiber doublets is high too (~8.5 p.e.) allowing an efficiency greater than 99.9%.
As far as the spatial resolution is concerned, the achieved doublet result is better than 100 μm in the ϕ direction.
The trigger information is provided by a FPGA system to which the digitized signals are sent. In less that 100 ns the system computes a Level 1 trigger decision with a sharp threshold on the transverse momentum P_T at ~1.5 GeV/c, a high efficiency and no dead area coverage [65, 66].

Chapter 3

Detector design and simulation

The FAST (Fiber Antiproton Scintillating Tracker) detector goal is to detect $\bar{p}p$ annihilations in gaseous or solid targets to measure the $\bar{p}p$ annihilation cross section at low energy (~100 MeV/c of momentum). This can be achieved detecting the annihilation products, in particular π^+s and π^-s, and counting the annihilation vertices.
As it will be explained in the next sections, the main constraint from the detector point of view is represented by the rate of events, requiring the capability of associating hits in the tracker to form a track based on the signal time (thus assigning what is called a time stamp). In other words, a very fast detector coupled to a very fast frontend electronics was a must. For these reasons, scintillating fibers and photomultipliers have been chosen; the frontend and readout electronics have been designed in order to allow the reconstruction of vertices to separate the target events from the wall and background ones.
In the following, the detector requirements will be analyzed and the final tracker will be described, discussing in detail each detector element, from the fibers to the electronics.
The tests performed on a small prototype of the tracker will be used to describe the expected performances in terms of spatial and time resolution.
The last part of the Chapter will be dedicated to a description of the Montecarlo simulations whose results will be presented in the next Chapter.

3.1 FAST design

3.1.1 Geometrical and time constraints

The FAST detector has to operate with the antiproton beam produced by the Antiproton Decelerator (AD) at CERN. As already described in Chapter 1, AD delivers a high intensity beam in bunches; each bunch contains up to 5×10^7 particles and lasts 200 ns (by design; the measured value in the data taking will be of 50 ns). The bunch period is 120 s.
The detector has to reconstruct the tracks of charged pions coming from a cylindrical volume with a diameter of ~20 cm (the beam pipe size). Therefore the detector geometry is cylindrical with the need, at least, of an inner tracking layer as close as possible to the pipe and of an outer one as far as possible; the latter one is obviously limited by the available space and by the fact that the farther from the center, the larger is the number of readout channels.
Given the bunch duration and the fact that a few tens of annihilations are expected for each bunch (with an average of 3 tracks per annihilation), the tracking has to be performed assigning the hits in the tracker medium to a track using the information on the time of crossing. This method requires a particularly fast detector, such as scintillating fibers, readout by a fast electronics ensuring a time resolution better than 10 ns FWHM.
The goal of the tracker is to reconstruct points in space, but since fibers have to be connected to the photomultipliers, the cylindrical structure doesn't allow the classical (r, ϕ, z) structure typical for example of silicon trackers. Thus, the geometry was chosen similar to the one used in the scintillating fiber trackers of UA2 and DØ (see Chapter 2): 2 axial layers, that is with the fibers parallel to the z direction on a cylindrical surface, and n stereo layers forming an angle with the z axis. The two axial layers define a plane in space and the n stereo ones n points for the track reconstruction, given by the intersection of each layer with the plane. As far as FAST is concerned, the approach has been slightly modified: two stereo layers have been coupled to each of the axial ones, building a triplet of layers very near one to the other, as the next section will describe. The passage of a particle generates a hit in every layer, resulting in a triple hit. If there are problems of crosstalk and more than three fibers are over threshold, this configuration allows to find the real hit, as it will be demonstrated.
The constraints on the spatial resolution are less stringent than the ones on the time resolution. To compute the $\bar{p}p$ annihilation cross section σ_{ann}, the reconstruction algorithm goal is to distinguish between the vertices in the target (with a dimension in the z direction of several cm for the gaseous ones and a few tenths of μm for solid

targets such as platinum) and the ones on the walls of the beam pipe. In the case of solid targets, the target spot is much smaller than the pipe (1 cm with respect to 8 cm) and the real difficulty lies in the distinction between the annihilations in the target and in the mylar support of the target itself (see next Chapter), while in the gaseous case, the target extends to the pipe walls. Moreover, given the momentum of the charged particles produced in the annihilation (200–800 MeV/c), multiple scattering would play a non negligible role on the spatial resolution. In both cases, a spatial resolution of several mm is enough to allow a good reconstruction efficiency.

3.1.2 The detector

In Fig. 3.1 the FAST detector scheme is shown. The considerations of the previous

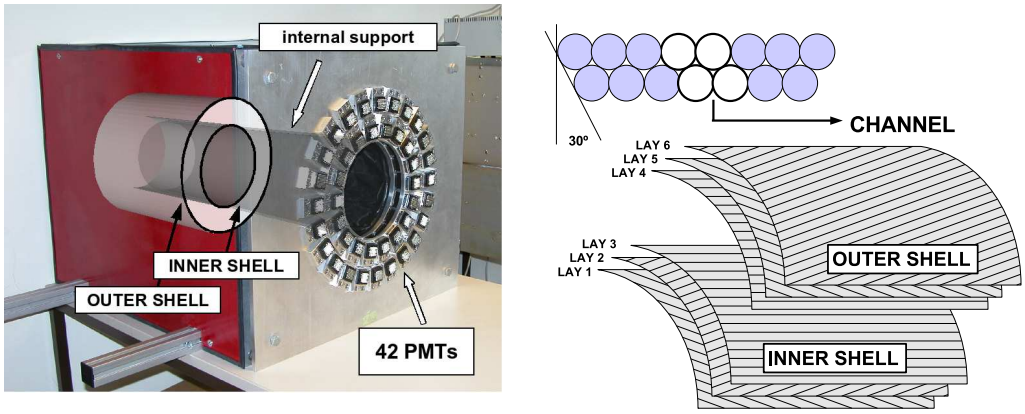

(a) (b)

Figure 3.1: (a) Scheme of the FAST detector. (b) Layout of the six layers; the direction of the fibers is indicated.

section has led to the final configuration of the FAST tracker:

- 6 layers of scintillating fibers organized in two "shells": an inner shell and an outer shell, each made of 3 layers (1 axial and 2 stereo at ±20°). The geometrical data are shown in Tab. 3.1 while the fiber characteristics will be described in Sec. 3.1.3. The total number of channels is 2405. Fig. 3.1(b) shows in the top part the fibers layout: 4 fibers are readout by a PMT channel. The lower part of Fig. 3.1(b) presents the layout of the two shells, indicating the fiber direction in each layer;

- the light produced in the fibers is readout by 42 Hamamatsu R7600-M64 multianode photomultipliers (Sec. 3.1.4);

- the PMTs are connected to 21 frontend boards where the output signals are amplified, shaped and discriminated by two VLSI ASICs before being sent to 4 repeater boards. Each repeater board is connected to an I/O VME board for the digital readout. The frontend and readout electronics are presented in Sec. 3.1.5.

Shell	Layer	mean radius (mm)	stereo angle	number of channels
1	1	117.9	+20°	334
	2	121.7	-20°	345
	3	125.5	0°	377
2	4	151.8	0°	461
	5	155.6	+20°	437
	6	159.5	-20°	451

Table 3.1: Scintillating fiber layers features.

Fig. 3.2(a) presents a photo of the final detector (without the readout electronics) during its assembly.
The two 3-layer shells are positioned on support plexiglass cylinders, 50 cm long and 3.4 mm (the inner one) and 4.4 mm (the outer one) thick. The first cylinder has a radius of 11.5 cm and the second one of 15.0 cm.
During the assembly phase, the fibers have been glued in bundles of 16 fibers each, which have then been positioned on the plexiglass support and fixed with glue and bi-adhesive tape.
Every layer on each shell is wound by a 250 μm thick polycarbon layer to create a smooth surface for the gluing. Each shell is covered by black tape to screen the fibers from light.
The fiber bundles have been aligned with the PMTs using dedicated iron alignment masks (Fig. 3.2(b)) produced by means of electrophoresis. Once inserted in the mask, they have been glued, cut and polished (Fig. 3.3(a)). The 42 masks have been aligned with the PMT support plane, an Al plate 2 cm thick where the PMT holders are screwed. Once the alignment between the masks and the PMTs had been concluded, the frontend and readout electronics have been positioned and connected (Fig. 3.3(b)).

(a) (b)

Figure 3.2: FAST tracker assembly: (a) all scintillating fibers have been placed on the supports and grouped to match the 42 PMTs; (b) detail of the iron mask to couple the fibers to the 64 PMT anodes.

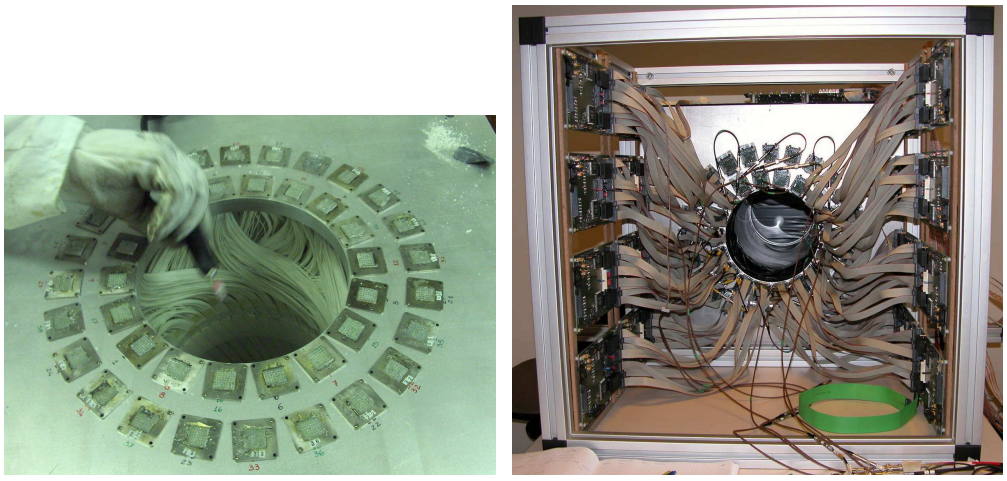

(a) (b)

Figure 3.3: FAST tracker assembly: (a) after cutting and polishing, the fibers are ready to be coupled to the PMTs; (b) assembly of the frontend electronics.

The sensitive part of the FAST detector is enclosed in an Al box with 4 removable panels to access the fiber themselves.

3.1.3 The scintillating fibers

Since the main constraint of the FAST tracker is the time resolution, a very fast detector has been chosen: scintillating fibers readout by multianode photomultipliers. Given that the PMT anode size is 2×2 mm^2, the fiber diameter has to be 2 mm at maximum. Two possible configurations have been tested for the single channel: a first one with 1 fiber with a diameter of 2 mm and a second one in which the channel is made of 4 fibers as shown in Fig. 3.1(b). This second configuration has allowed to reach a 99% efficiency [67], demonstrating to be the right choice. The fibers used for FAST are 1 mm diameter BCF-10 multiclad fibers with white EMA (Extra Mural Absorber) by Bicron, whose features are listed in Tab. 3.2.
The EMA limits the dispersion of light from the border of the fiber to the neighbouring ones. The fiber end not coupled to the PMT has not been polished so that it acts as a dumper, absorbing all the photons arriving on this side.
A total of about 10 km of BCF-10 fibers has been used to assemble the FAST detector.

fiber type	BCF-10
emission peak	432 nm (blue)
decay time	2.7 ns
1/e length	2.2 m (1 mm diameter)
no. of photons/MeV	~8000 (mip)

Table 3.2: BCF-10 scintillating fiber data relative to 1 mm diameter fibers (from Saint-Gobain web site, http://www.saint-gobain.com)

3.1.4 The photomultipliers

The need of a good time resolution together with the large number of readout channels and the desire of compactness, has led to the choice of a multianode photomultiplier whose details are described in Tab. 3.3. It has 64 2×2 mm^2 anodes (Fig. 3.4) with a quantum efficiency greater than 20% in the 300–650 nm range; it is endowed with an insulated plastic case with an integrated voltage divider. Its gain goes from 2.5×10^5 at 775 V to 7×10^5 at 850 V; the gain of the 64 channels of the PMT is not uniform: if the maximum gain anode has a value of 100, the rest of the channels spreads over a range whose average value[1] is 79±10. Anyway these fluctuations are of the same order of the ones due to the number of photoelectrons

[1] data of 30 PMTs; the anodes gain values are provided by Hamamatsu.

produced at the photocathode window as it will be shown in the Montecarlo simulation (Sec. 3.3.1); thus no corrections were made offline on the output signals.
The total number of PMT anodes is 2688, while the total number of readout chan-

anode size	2×2 mm^2
effective area	18.1×18.1 mm^2
spectral range	300–650 nm
peak wavelength	420 nm
quantum efficiency at 390 nm	0.21
window material	Borosilicate glass
maximum HV	-1000 V
gain	3×10^5 (at -800 V)
anode gain uniformity	1:2.5
transit time	12.0 ns
transit time spread	0.38 ns
dark counts per ch.	~50 Hz (at 25°C)

Table 3.3: Hamamatsu R7600-M64 photomultiplier characteristics [45].

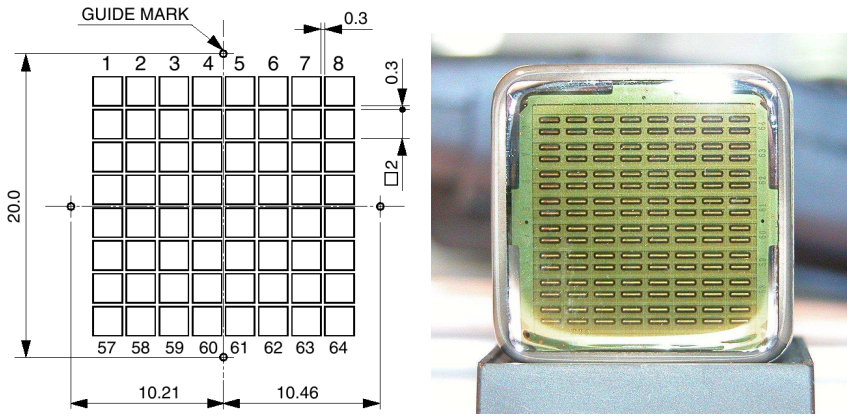

(a) (b)

Figure 3.4: Hamamatsu R7600-M64 photomultiplier anodes scheme (a) and photo (b).

nels is 2405, which means that not all the anodes are coupled to fibers. Moreover, given the structure of the tracker, the coupling is not ordered but determined by the bending of the fiber bundles. This has required the use of a map to arrange the readout channels in terms of the fiber number.

3.1.5 The electronics

The FAST electronics chain has to cope with a bunched beam with a period of 120 s and lasting 200 ns. In the 200 ns interval it has to assign a time stamp to every fiber over threshold and to transfer data in the time between bunches.
From the practical point of view, this is the sequence of the events:

- the detector is configured at the beginning of the run and a threshold is set for every discriminator connected to the PMT anodes;
- a trigger signal is generated by AD, that in turn starts the data taking gate; during this gate, the discriminated signals are sampled with a 320 MHz clock. Since both the rising and the falling edge of the clock are used for the sampling, it is equivalent to the use of a 640 MHz clock. The gate lasts in fact 800 ns, to be sure to sample the bunch inside the window given by AD;
- once the acquisition is finished, the sampled bits, stored in a local memory, are transferred to the DAQ PC. Since in a 800 ns window each channel is sampled 512 times and the total number of channels is 2688 (also the PMT anodes with no fibers are read), 172 kB have to be transferred for each bunch.

The different parts of the electronics chain are shown in Fig. 3.5. It can be divided in two main items: the frontend part and the readout one.

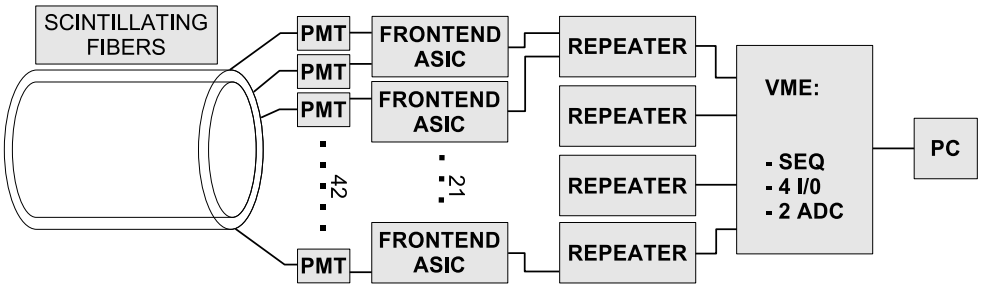

Figure 3.5: The FAST electronics chain.

The frontend

It consists of 21 FR4 PCBs (Printed Circuit Boards) of 125×230 mm^2 able to control 2 PMTs each (Fig. 3.6). The 64 PMT signals, which are brought to the board with 4

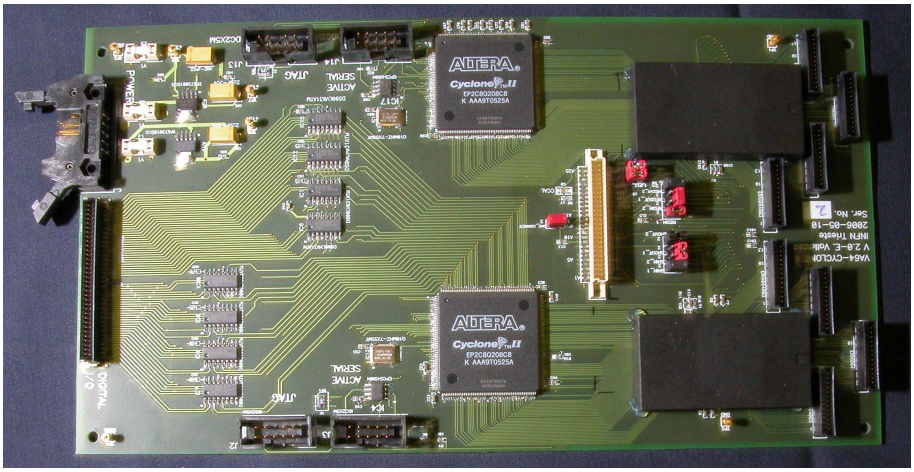

Figure 3.6: The FAST frontend board.

26 pin ERNI cables, are amplified, shaped and discriminated by the VA64TAP2.1 ASIC[2]. The VA64TAP2.1 is built in 0.35 μm N-well CMOS double-poly triple metal technology and consists of a preamplifier with pole zero cancellation to minimize pile-up effects, a CR-RC fast shaper (50-75 ns of peaking time) and a discriminator with a global threshold for all channels and a 4 bit trim DAC per channel to minimize the offset spread. The VA64TAP2.1 channel architecture is shown in Fig. 3.7. The ASIC can be read in an analog mode, connecting the output of each

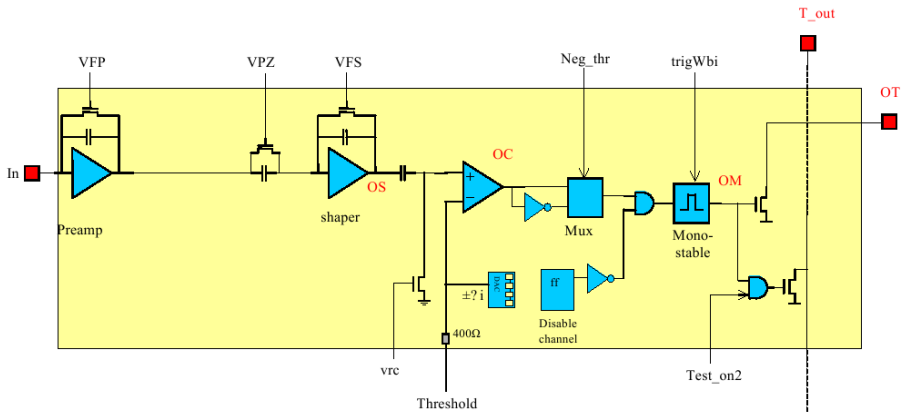

Figure 3.7: The VA64TAP2.1 ASIC channel scheme (from IDEAS datasheet).

[2]IDEAS - Norway

shaper, after having sampled it with the hold signal (the sample and hold circuit is not shown in Fig. 3.7), to the analog output buffer; the analog readout is a multiplexed one, that is the sampled signals are sent out one after the other on the differential output buffer thanks to a clock signal (with a maximum rate of 10 MHz).
As far as the digital mode is concerned, when the digital outputs are enabled, the discriminators generate a square pulse (trigger output), whose length is tunable in the sub-μs range, if the shaper output is over threshold. The discriminated signal duration is fixed by a monostable, thus there is no correlation between its value and the pulse height of the shaper output. The parallel trigger outputs are open drain and should be terminated with low impedance in order to avoid pile-up effects in the other channels. This is accomplished by another ASIC the LS64_2[3]. In order to work properly, the VA64TAP2.1 has to be configured by loading a register of 396 bits, which sets the trim DACs, enables the digital outputs, chooses between positive and negative (like the PMT ones) input signals, enables the test mode and the channel to be tested (each channel can be calibrated for test purposes).
The 2 VA64TAP2.1s on each frontend board are connected in daisy chain, which means that the control signals are the same, they are read one after the other and the calibration register is a unique register 396×2 bit long.
The digital outputs of the 2 LS64_2s are the inputs of two Altera Cyclone II FPGAs[4]. These chips are low power low cost devices featuring a ~164 kbit RAM memory on board able to store more than 2000 sampled bits per channel. The 320 MHz sampling clock is generated by the FPGAs themselves starting from the 10 MHz clock of the quartz on the board.
Several prototypes of the frontend have been designed and tested. The final time resolution reached with a 30 cm long module with 1 mm BCF-10 fibers and a R7600-M64 PMT is 3.5 ns [67].
The final production consisted in 24 boards corresponding to 3200 channels with the following results:

- the number of dead channels is lower than 10;
- the gain spread for the ASICs is around 4%;
- the offset spread (where the offset is defined as the value in DAC units at which the threshold is zero) corresponds to 0.1 fC, that is a few percent of a one photoelectron signal.

[3] IDEAS - Norway
[4] model EP2C8Q208C7

The readout

The readout electronics is composed of two blocks: the repeater boards, which are the interface between the frontend boards and the DAQ, and the DAQ itself.
REPEATER BOARDS:
they are shown in Fig. 3.8. Each board controls up to 6 frontend boards performing the following tasks:

- it provides the biases and control signals to the ASICs and sets the thresholds;
- it demultiplexes the analog signals coming from the frontend and amplifies them through a NE592;
- it manages the trigger signal and synchronization one, which is a debug signal to check that the boards are sampling the same clock pulse (the clock is generated locally on each frontend board);
- it handles the communication between the FPGAs and the VME DAQ system.

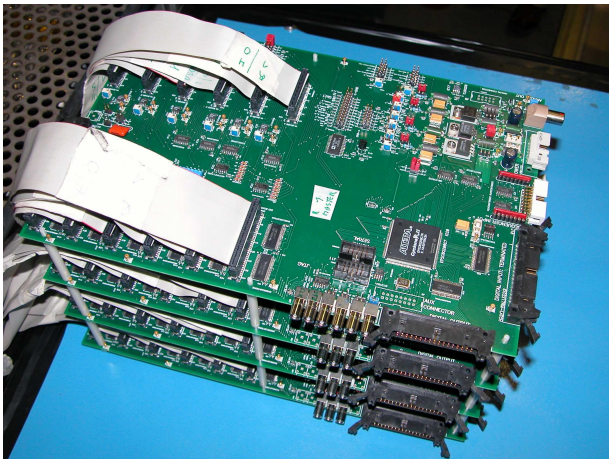

Figure 3.8: The FAST four repeater boards in their final configuration.

DAQ:
the DAQ scheme is shown in Fig 3.9. It has been developed to allow both the analog and the digital operation of the FAST tracker.
The VME sequencer[5] (SEQ) is connected to the 4 repeaters in parallel and generates the analog readout sequence. Once an event is triggered (or a random trigger is

[5]INFN - Trieste

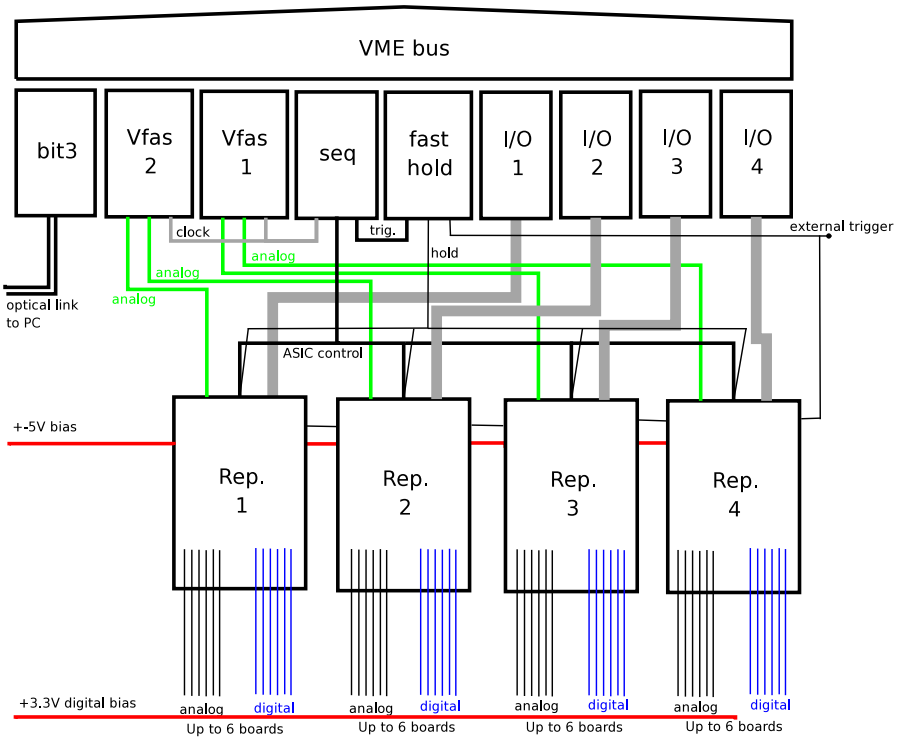

Figure 3.9: Data acquisition scheme.

generated directly from the SEQ for what is called a pedestal run), the fast hold board generates the hold to sample the ASIC shaper outputs. The SEQ sends 768 clock pulses to each repeater, which addresses in turn each ASIC on each frontend board. The differential outputs are multiplexed and sent to the VME 12 bit flash ADCs[6]. The fast hold is busy till the end of the analog readout and then has to be reset via software. The SEQ is dummy during the digital operation mode.
The 4 I/O boards[7] are the responsible of the digital operation. They are used at the beginning of the run to load the configuration registers (through the repeaters) and during the data taking to read the sampled bits stored in the FPGAs.
The maximum data taking rate is 3 kHz (with no dead time) in analog mode and 1 Hz in digital (but given the bunch structure of the beam, there is time enough to transfer all the data without losing events).
The VME system is interfaced with the DAQ PC through a SBS Bit3 model 620

[6]VFAS, LEPSI - Strasbourg
[7]INFN - Trieste

VME bridge [68] . The DAQ software is written in C, while the output data are PAW ntuples. The user interface is written in Tcl/Tk [69] and is shown in Fig. 3.10.

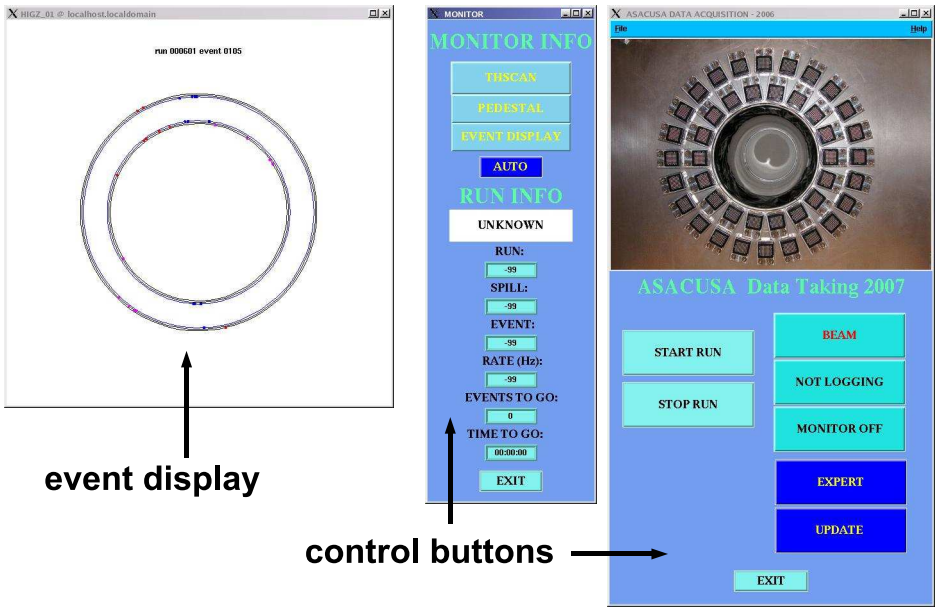

Figure 3.10: DAQ user interface.

3.2 The prototype

The design and assembly of a detector such as FAST have required the development of several prototypes, both from the mechanical and electrical point of view.
As far as electronics is concerned, three steps, corresponding to three different detectors, have been undertaken:

- the first one consisted of 16 2-mm-diameter fibers readout by a 16 channel multianode PMT[8];
- in the second prototype the fibers were those used in the FAST tracker. 16 groups of four 1-mm-diameter fibers were coupled to the same multianode photomultiplier;

[8]MA-PMT H8711 by Hamamatsu, which has the same features of the 64 channel PMT apart from a higher gain.

- a complete prototype with 64 channels (1 PMT) organized in 3 layers as in one of the two ASACUSA cylindrical shells was the last step.

The first two detector tests were performed with standard NIM electronics and a commercial TDC to measure the time resolution; the following results have been obtained [67]: a time resolution of ~3 ns (measured with both a ^{60}Co source and a 500 MeV electron beam), and an efficiency of ~80% for the first prototype (averaged over the fiber width, but if only particles passing through the fiber center were selected the efficiency became ~90%) and 99% for the second one. The results on the timing performance of these two assemblies have been fundamental for the final design of the tracker, allowing to define the layout of the frontend electronics, the number of channels and the number of fibers per channel.
The third prototype has allowed the test of the complete electronics chain in analog and digital (as used in ASACUSA) mode and the measurement of the final spatial and time resolution. The results have been used in the Montecarlo simulation and have validated the hardware choices.
In the following the characteristics of this prototype and the tests on the beam are described.

3.2.1 Prototype characteristics

The prototype consists of 256 scintillating fibers readout by one 64 channel photomultiplier (see a photo in Fig. 3.11); its geometry is sketched in Fig. 3.12.
The goal was to reproduce the geometrical structure of the final detector, therefore 3 layers of scintillating fibers (1 mm of diameter) have been placed respectively at 0° (16 channels), +20° (24 channels) and -20° (24 channels) with respect to an arbitrary direction. Each channel deals with 4 scintillating fibers as in the FAST tracker. The stereo planes (±20°) have been assembled above the "longitudinal" one (placed at 0° with respect to the direction orthogonal to the PMT window plane). In this way, the sensitive area of the prototype was ~31 cm^2. The schematic map of the correspondence between the channels and the PMT pads is shown on the left of Fig. 3.12.
The signals of the 64 channels were processed by the same electronics chain of the FAST tracker: they were amplified, shaped and discriminated by the VA64TAP2.1 and LS64_2 ASICs, sampled by the Cyclone II FPGA and then sent to the VME I/0 (see Sec. 3.1.5).
The fibers were coupled to the PMT window using the same iron mask developed for the tracker and glued on a 5 mm PVC support for a total thickness of the detector of ~6 mm.

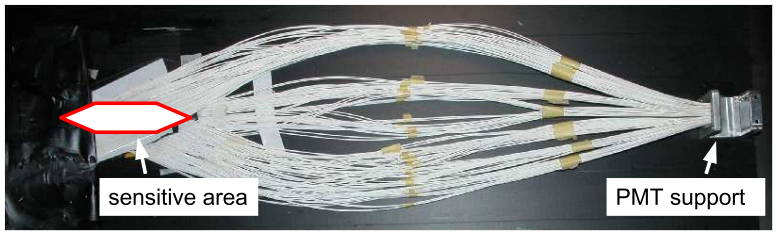

Figure 3.11: Tracker prototype photo. The 3 layers of 1 mm scintillating fibers overlap on the left defining a sensitive area of ~31 cm^2. On the right: a PMT aluminum support is used in order to host the fiber mask.

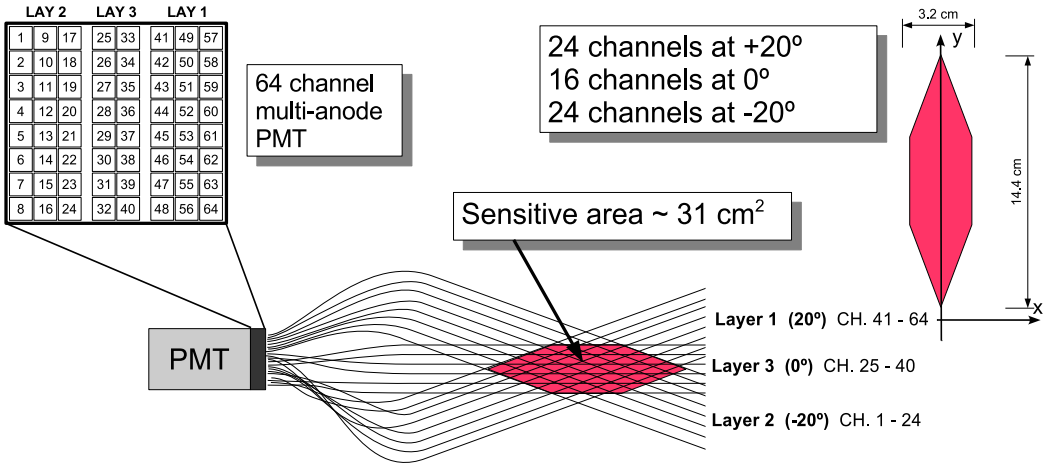

Figure 3.12: Tracker prototype scheme. It consists of 256 scintillating fibers with a diameter of 1 mm, 4 fibers per channel, 16 channels on the longitudinal plane at 0°, 48 channels on the 2 stereo planes at ±20°. The three planes displacement creates an active surface of 31 cm^2. The 64 channels are readout by a single multianode photomultiplier as indicated on the 8×8 array on the left.

3.2.2 Tests with an electron beam

The prototype has been tested at the Beam Test Facility (BTF) at the National Laboratories of INFN in Frascati (Rome).

The Beam Test Facility beam

The DAΦNE (Double Anular Φ-factory for Nice Experiments) e^+e^- collider, located at the National INFN Laboratories in Frascati[9], is a high luminosity source for precision experiments as FINUDA or KLOE (for both experiments see INFN National Laboratories homepage). In Fig. 3.13 a view of the whole facility is shown.
A secondary beam transfer line (BTF) takes electrons or positrons directly from the

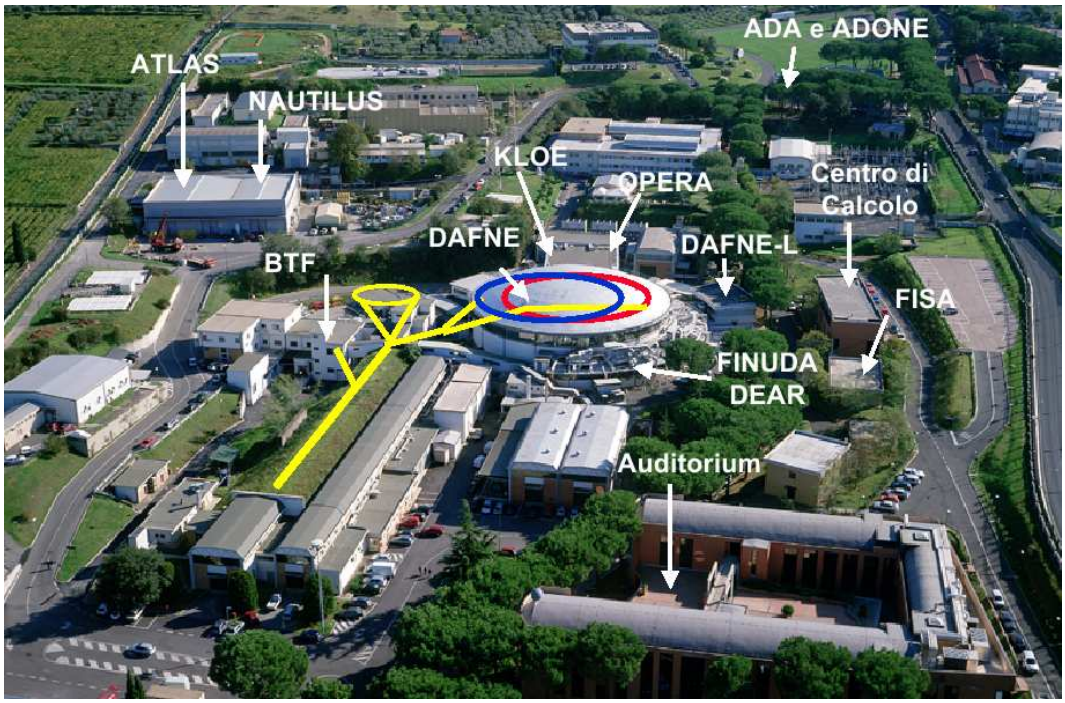

Figure 3.13: Aerial view of the National Laboratories at Frascati, Rome.

linear accelerator with a kinetic energy up to 750 MeV; the BTF has been designed in order to have, by means of movable slits and focusing magnets, an operational mode in which single electrons (or positrons) are stochastically produced for detector calibration purposes. In such a way it is possible to control the beam multiplicity in a wide range (from $\sim 10^{10}$ down to 1 particle per extraction). The repetition rate is 50 Hz. In Tab. 3.4 some beam parameters are shown.

[9] http://www.lnf.infn.it

Energy range	25-750 MeV e^-/e^+
Max repetition rate	50 Hz
Pulse duration	~10 ns
Current/Pulse	1 - 10^{10} particles

Table 3.4: Typical electron/positron beam parameters at the BTF - INFN National Laboratories.

Test results

Several tests have been performed in order to characterize the prototype behaviour:

- detector efficiency;
- crosstalk;
- spatial resolution.

The beam energy was maintained almost fixed at 500 MeV[10]. The spatial resolution has been computed using, as a tracking reference, two x-y silicon strip detectors with a spatial resolution of ~40 μm [70] whose details will be given in Sec. 4.1.2. The experimental setup is shown in Fig. 3.14. The PMT bias has been chosen in the range 700–850 V (negative polarity).
It must be noticed that, although the electronics can work both in analog and digital mode (as already illustrated in Sec. 3.1.5), the data were taken only in analog mode for the spatial resolution and efficiency evaluation. A dedicated digital run has been performed with different thresholds to check the whole readout chain, but the results will not be presented here.
The data taking/analysis procedure was the following:

- acquisition of a *pedestal run*, that is acquiring data with a random trigger, in order to compute the baseline (Fig. 3.15(a), Fig. 3.16(a)) and the noise (Fig. 3.15(b), Fig. 3.16(b)) of each channel. The noise value is the one obtained after the common mode subtraction, that is the noise contribution due to noise on the bias line of the detectors. The common mode noise varies on an event by event basis and is computed as the variation of the baseline common to all channels each event;

[10] In this energy range electrons can be treated as minimum ionizing particles; therefore their energy loss inside matter is 1.936 MeV g^{-1} cm^{-2} [41].

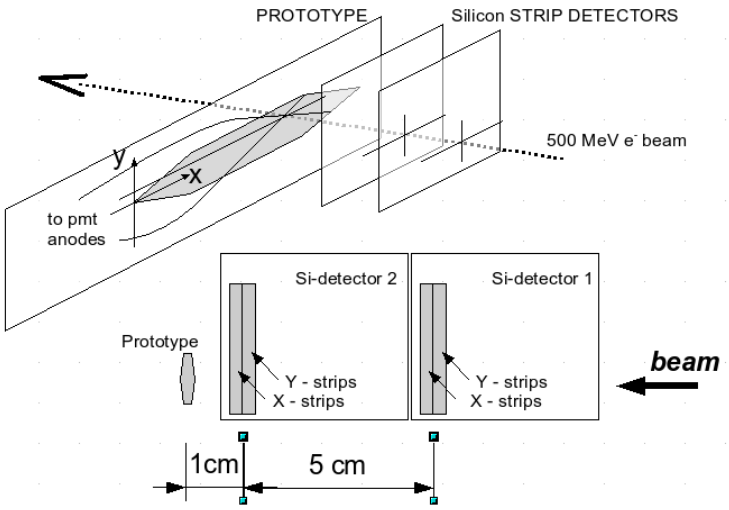

Figure 3.14: Experimental setup at the BTF. Si-strip detectors were used as a reference tracking system (spatial resolution $\sim 40\mu$m) in order to evaluate the prototype spatial resolution.

- data acquisition (DAQ); the DAQ setup is shown in Fig. 3.17. It is a VME based system, featuring two 12 bit flash ADC units (LEPSI, Strasbourg) for the analog readout and several control boards (SEQ, fast HOLD, I/O; INFN - Trieste). The DAQ readout sequence is generated by the SEQ once it receives the trigger. The trigger was taken from the LINAC itself and shifted in time in order to sample the PMTs and strips signals at the right time. From the analog point of view, the silicon detectors and the prototype need the same readout sequence: the *hold* signal samples the analog output of each channel shaper; the sampled levels are multiplexed on the output lines with a 2.5 MHz clock, further amplified by a NE592 amplifier on the so called repeater boards and sent to the ADC.
  Since the signal shaping constant is much lower in the fiber case (~50 ns) than in the silicon detectors (~1.5–2 μs), a dedicated board (fast HOLD) generates the hold signal for the prototype.

  As already described in Sec. 3.1.5, a register has to be loaded in the VA64TAP2.1 ASICs. This task is accomplished by the I/O, which also reads the digital out when the prototype is operated in digital mode.
  Apart from the second level amplification, the repeater boards transform the control signals from differential to single ended (when needed), shift them to

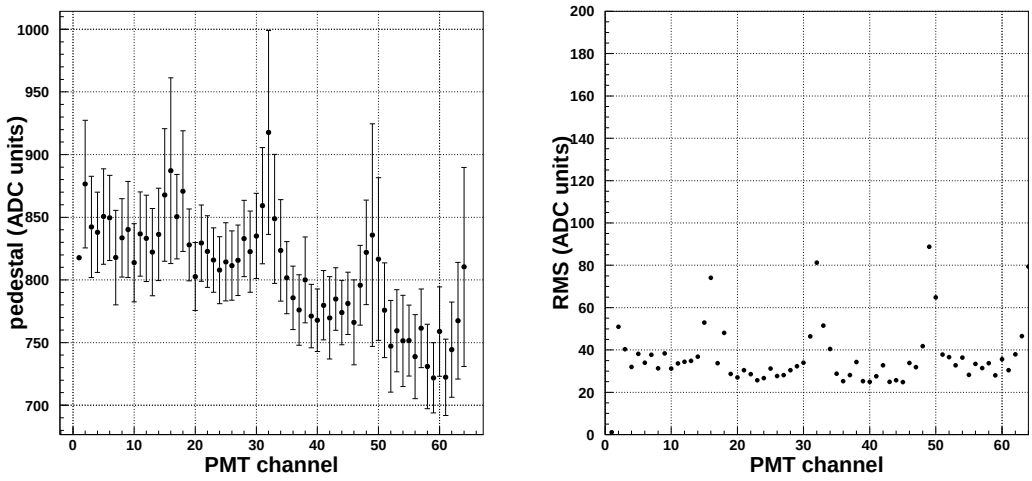

(a) Pedestal of the prototype. The correspond- ing noise RMS values are shown as error bars

(b) Noise RMS values for the 64 channels of the prototype

Figure 3.15: Prototype pedestal and noise RMS values. The periodicity of the noise RMS is due to the routing on the frontend board of the connections between the PMT channels and the ASICs input pads and to the ERNI cables to connect the PMT to the frontend board.

the right voltage level (from 0/5 V to -2/+2 V for the silicon and -2/+1.5 V for the VA64TAP2.1), generate the biases for the ASICs and the threshold for the ASICs discriminator.
The connection between the VME and the PC is performed through a BIT3 SBS 620 bridge [68]. The DAQ software is written in C, with Tcl/Tk [69] for the user interface;

- once offline, the pedestal value is subtracted from the raw data determining the channel response in ADC units. In Fig. 3.18 two "pull" plots are shown. The pull is defined as the ratio between the pulse height of the channel with the maximum signal in the event and its corresponding noise RMS; it is used to define an event as good: in the silicon detectors case, a pull greater than 10 means that a particle has crossed the strip. For the analysis, all the events with one single track have been selected, that is all the 4 planes have a strip with a pull greater than 10 and one single hit only[11]. The prototype pull plot

[11]For each event and each plane, clusters are looked for to define a hit. A cluster is a group of

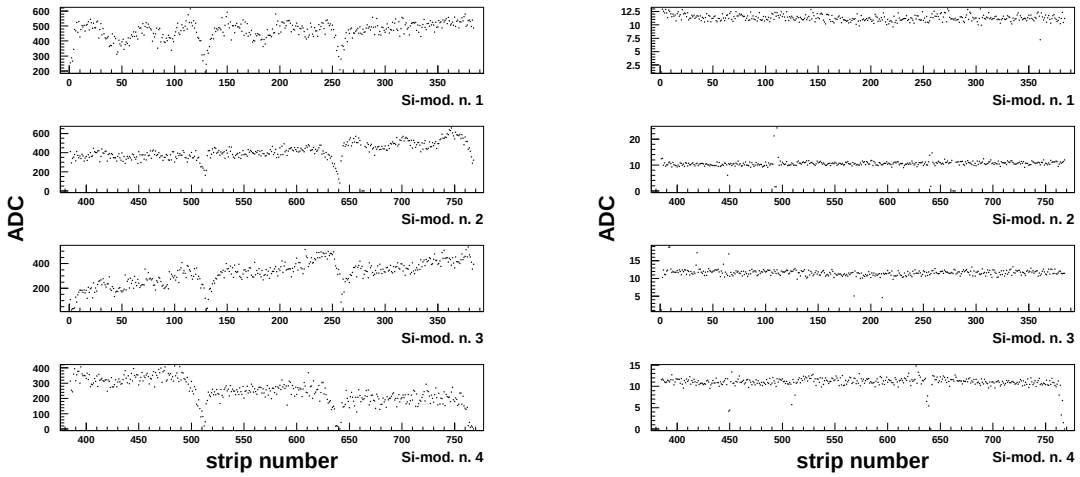

(a) Pedestal values of the 4 silicon detector modules

(b) Noise RMS values of the 4 silicon detector modules

Figure 3.16: Pedestal and noise RMS values for the 4 silicon detector modules. The total number of channels is 1536 (4×384).

(Fig. 3.18(b)) is quite different from the silicon detectors ones. This was due to several factors:

- ▷ The optical crosstalk between different PMT pads; given that the number of photoelectrons is small, the result is a large statistical fluctuation of the readout signal pulse heights.
- ▷ The noise RMS distribution of the PMT channels (Fig. 3.15(b)) that had an irregular behaviour (as a comparison in Fig. 3.16(b) the one of the silicon modules is shown). The 16 channel periodic shape was due to the capacitance of the lines connecting the PMT channels to the ASIC input pads on the frontend board and to the ERNI cables connecting the PMT PCB base to the frontend board. The channels that showed the highest RMS values were those with the longest routing on the board or those located on the borders of the cables.

Thus a more complicate set of cuts had to be defined to select good events:

nearby strips that have collected the charge deposited by the particle. The cluster must have 1 strip with the pull greater than 10 while the nearby ones cut on the pull is 5. Two clusters are considered separate if the distance between their maximum is greater than 2 strips.

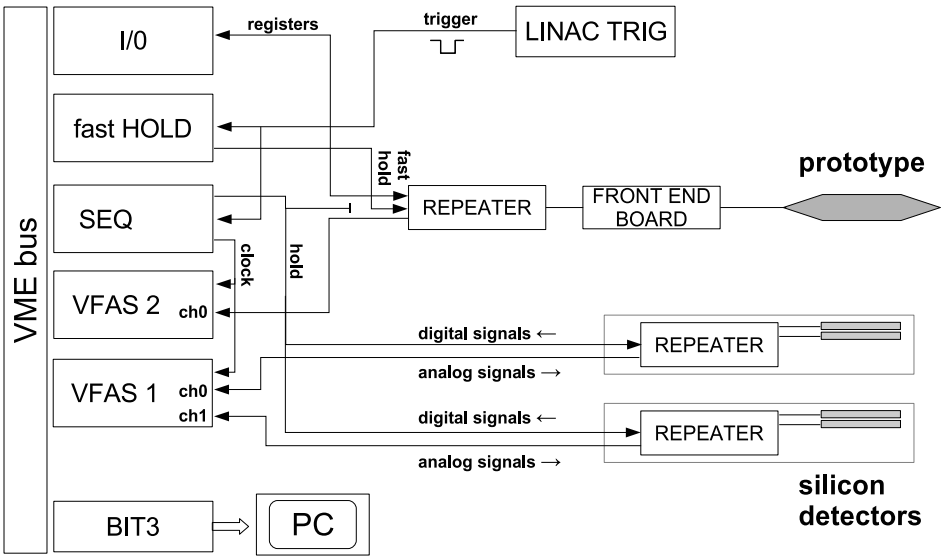

Figure 3.17: Data acquisition scheme for the prototype at the BTF. The analog signals coming from the prototype and the silicon detectors repeaters are sampled at a given time fixed by the hold signal; the hold value is different for the two types of detectors: the prototype signal formation is very fast (~50 ns) compared to the silicon detector one (~ 1.5–2 μs), therefore the prototype repeater has a shorter dedicated *fast hold* signal.

an *or* condition has been applied requiring a pull of at least 20 or a pulse height greater than 700 ADC units. The pulse height plot is presented in Fig. 3.19 together with a Montecarlo simulation. The comparison of the two plots demonstrates that in the prototype case, the number of photoelectrons produced in the fibers generate a PMT signal high enough to saturate the ASIC dynamic range. This is demonstrated also in Fig. 3.20 where the pulse height plot has been considered as a function of the PMT bias voltage: going from 850 V to 775 V (that is reducing the gain of a factor 3), no difference in the pulse height peak value is present. The cuts have been verified considering the beam profile distribution (Fig. 3.21; a non optimal selection on the events would generate "holes" in the beam profile, due to the artificial depletion of some of the noisy fibers) and the correlation with the silicon detectors.

Once completed the selection of events, a 64 character string is written, for each good event, with a 1 for the hit fibers and a 0 for the not hit ones: the FAST

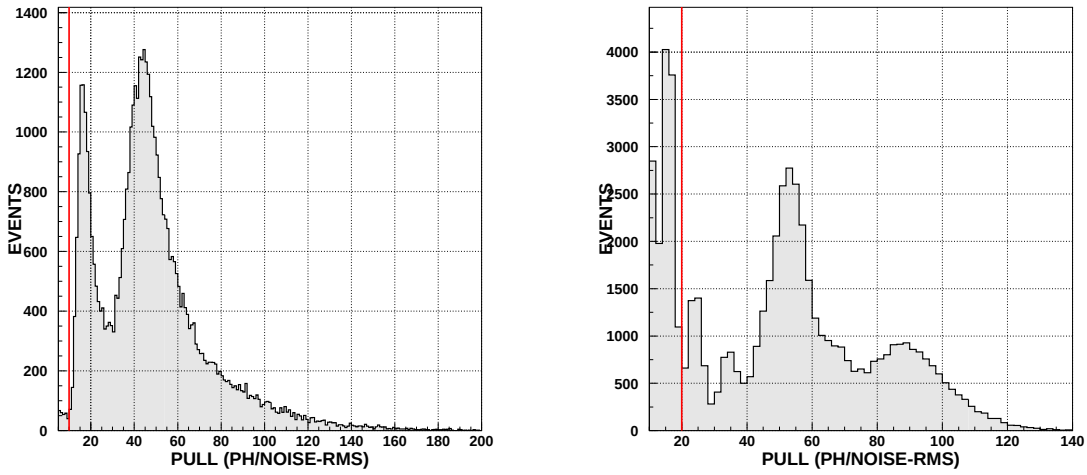

(a) One silicon detector module (b) Prototype

Figure 3.18: Plot of the pull, defined as the ratio between the pulse height (PH) of the strip/channel with the maximum signal in the event and its corresponding noise value (RMS); these plots can be used to fix an ADC value below which an event is "noise" and above which the event has to be stored as good. As an example, two possible choices of this value are shown with the vertical line (drawn at a pull value of 10 for the silicon detector and at 20 for the prototype). The double-peak shape of the silicon module pull is due to the presence of a floating strip. In fact, the readout pitch of these detectors is 242 μm with a physical pitch of 121 μm, that is one every two strips is connected to the readout electronics. If the particle crosses the readout strip, the signal is completely collected, while if it crosses a floating one, the signal is induced on the nearby readout ones, that is each readout strip collects approximately 38% of the total signal [70].

prototype has become a digital detector. The analysis described in the following has been performed on the digital data obtained in this way.
Fig. 3.22 shows the graphical interface implemented to monitor the prototype behaviour during the data taking. Looking at the geometry, hit channels can build three different classes of intersections on the basis of what layer they belong to: the 12-type, the 13-type and the 23-type. These intersections will be called *doublets*. Another useful definition is the *triplet* (or *triangle*) which is made of 3 doublets of different kind. In the ideal case, when the electron passes through the scintillating fibers, 3 channels switch on and make a triplet. When this does not happen (because

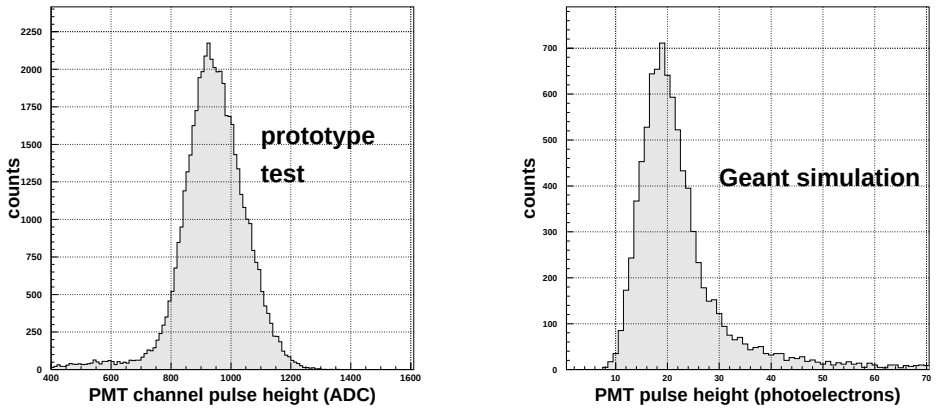

(a) (b)

Figure 3.19: Prototype pulse height distribution of the channel with the maximum signal as measured in the prototype tests (a) and as computed by the Geant simulation (b) that will be described in Sec. 3.3.1.

of detector inefficiencies or crosstalk, as will be discussed later on) the following algorithm decides what to do:

- all hit channels are considered and the so formed doublets (if there are any) are stored in memory;
- all possible triplets are built; at the end, only the "best" is kept, where the best means the triangle with the smallest height (as well as the smallest area which goes linearly with the height);
- the hit is positioned at the center of gravity of the best triangle.

It has to be noticed that if there were too many hits the event had to be rejected: the cut was put at 10 channels. In Fig. 3.23 an example of a hit reconstruction is presented.
In Fig. 3.24 the total number of hits (as a percentage of the total number of selected events) is shown. The analyzed events are those between 3 hits and 10 hits at maximum.

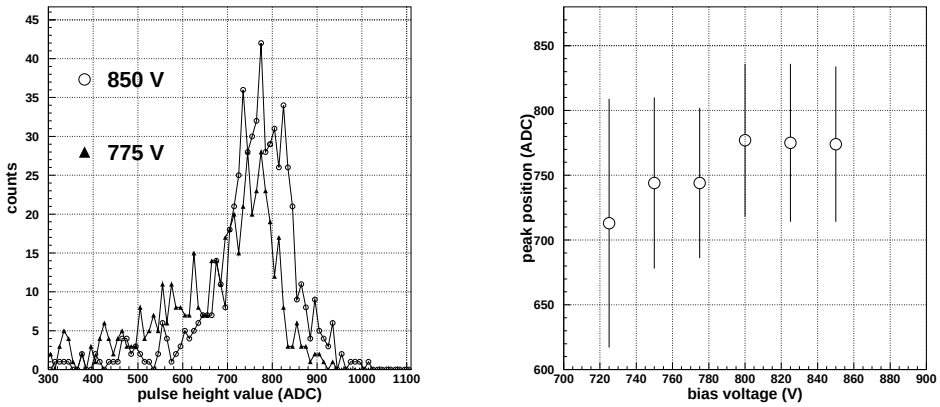

(a) (b)

Figure 3.20: Prototype pulse height distributions (a) (only two values of bias are shown; the statistics is poor due to the small number of events collected during the scan) and corresponding peak position (b) at different PMT bias values (the peak position and error are, respectively, the mean peak position and the sigma parameter of a gaussian fit in the peak region). Even if the high voltage is lowered from 850 V to 775 V (that means a factor ~3 in the gain as seen in Sec. 3.1.4) the peak does not change its position showing that a saturation is occurring; this has nothing to do neither with the ADC (because saturation would be at 4096 ADC units apart from the pedestal subtraction), nor with the PMT (the amount of light involved is of the order of a few photoelectrons). The problem is that the PMT signal saturates the ASIC dynamic range.

Efficiency

As far as efficiency is concerned, a raw estimate of the single layer efficiency can be computed counting the hits on each layer (Fig. 3.21(a)) and comparing them with the incoming number of particles reconstructed by the silicon detectors and extrapolated on the prototype plane to be sure of the passage through the region covered by the prototype itself. The results are shown in Tab. 3.5 (Method 1). The second layer shows a poorer efficiency due to the worse optical coupling between the fibers and the PMT anodes, as a visual inspection after the test beam has revealed.

A second way of calculating the single layer efficiency is the following:

- the first step was to select, analyzing all the events, a fiducial region for the

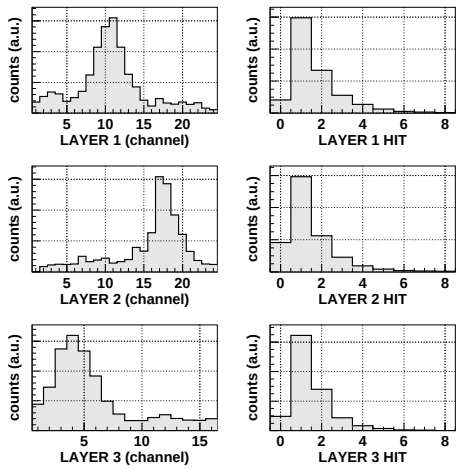

(a) Prototype beam profiles (left) and corresponding number of hits (right) for each layer.

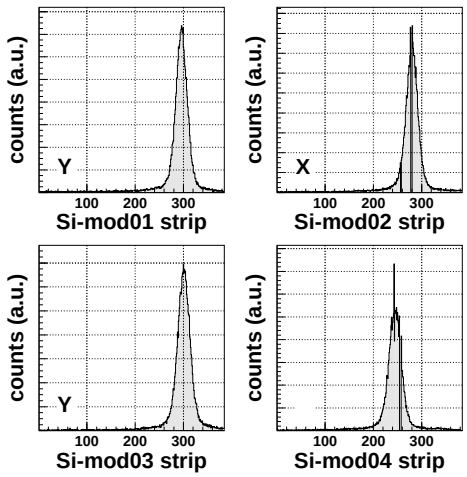

(b) Beam profile on the 4 silicon detector modules (2 x-y planes)

Figure 3.21: Beam profile plots of the 3 prototype layers and of the silicon detectors.

	Method 1	Method 2
LAYER 1	92.9%	91.4%
LAYER 2	84.4%	81.4%
LAYER 3	91.7%	93.3%

Table 3.5: Single layer efficiencies as computed with the two methods described in the text.

presence of the beam on the prototype fitting with a gaussian function both the x and the y hit positions as shown in Fig. 3.25;

- the region is defined as an ellipse whose center coordinates are the x and y mean values (as found with the fit) and whose axes lengths are given, respectively for the x and the y one, by $3\times\sigma_X$ and $3\times\sigma_Y$[12];
- once the region contours have been marked, the 12-doublets (inside that region) that did not have a corresponding hit channel on layer 3 have been counted; in other words, what one measures is the inefficiency of layer 3. The

[12]It has been chosen a factor 3 in order to take into account all the incoming particles, in fact in a gaussian distribution 99.7% of the events are inside the so called *confidence interval* of 3σ.

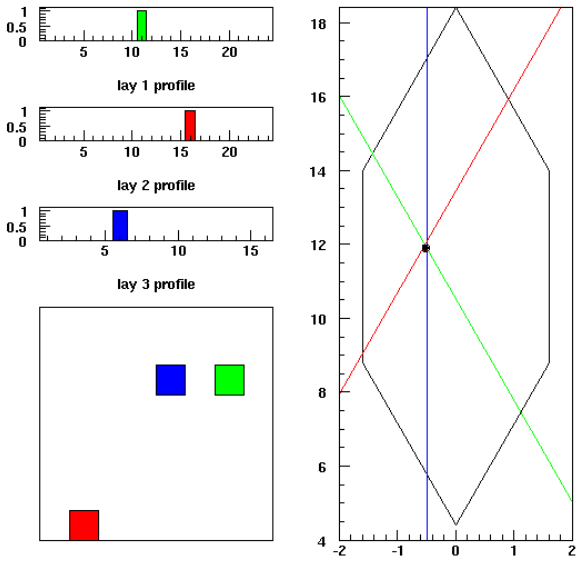

Figure 3.22: Graphical monitor for the prototype event display during the test beam at the BTF. On the left: the channel profiles (lay1 and lay2 are the stereo layers, while lay3 is the one placed at 0°, which in this scheme is the vertical one) and the PMT 8×8 pad array (see the pad map on the left of Fig. 3.12). On the right: a representation (not to scale) of the sensitive area with the hit channels. In this "good" event the reconstructed position of the particle track on the prototype (given by the interception of the three drawn fibers) and the track as computed by the silicon strip detectors projected on it (represented by the dark dot) are perfectly superimposed.

same was done for layer 1 (counting the 23-doublets without a corresponding hit channel on layer 1), and layer 2;

- after having determined the fraction of events in which this occurred, the single layer efficiencies have been calculated and the values are shown in Tab. 3.5 (Method 2).

The two methods are in agreement and show a poorer efficiency for layer 2 with respect to the other two.

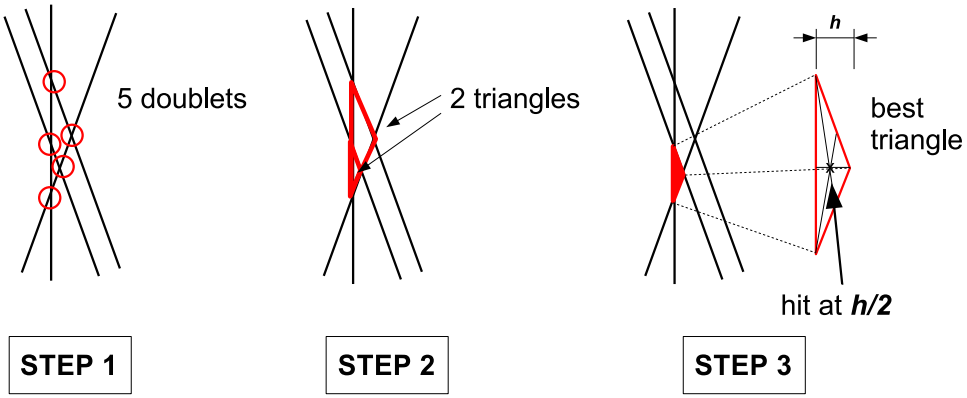

Figure 3.23: Scheme of the reconstruction of a hit. Among all hit channels, all doublets are considered (STEP 1), then all the possible triangles (triplets) are computed (STEP 2) and the one with the minimum height (h) is kept: the hit is positioned at the center of gravity of this triangle (STEP 3).

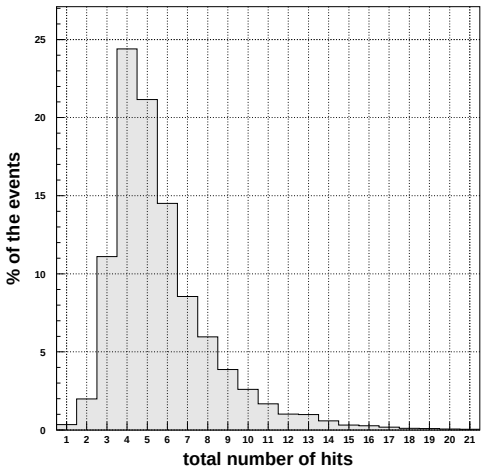

Figure 3.24: Prototype total number of hits normalized to the number of events. When hit channels are less than 3 no analysis was performed, as when hit channels were more than 10.

Crosstalk

The optical crosstalk occurs when the light carried by the scintillating fibers hits not only the PMT pad corresponding to the hit fibers but also one of the 8 surrounding

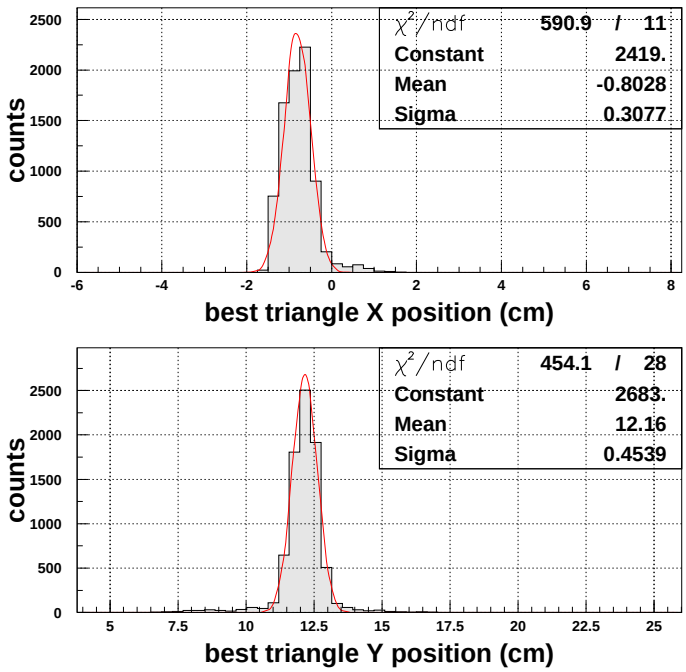

Figure 3.25: Reconstructed hit x and y position. The gaussian fit provides the boundaries of a fiducial region for the presence of the beam on the prototype.

pads. An example of this kind of event is shown in Fig. 3.26. As shown in the following, if the efficiency is high enough, the crosstalk does not prevent a correct reconstruction; in fact a false hit (i.e. a signal that does not come from the real passage of a particle in any of the 4 fibers of that channel but from the light of some nearby pad) creates one or more false doublets and consequently one or more false triangles, but, once offline, the search for the best triangle recognizes the "ghosts" (as it can be seen in Fig. 3.26 where the passage point is reconstructed in the correct position).
In order to evaluate the amount of hits with crosstalk, every time a channel (a pad) was hit, all 8 nearby pads were sampled and a 3×3 grid was filled. At the center of this grid there is the hit pad, the other cells correspond to the nearby pads; for this purpose only the central region of the PMT was considered (as shown in Fig 3.27(a)) because the border pads are not completely surrounded by other pads. The results are shown in Fig. 3.27(b).

Even if this method has a "forced symmetry" drawback[13], some considerations can be done: the asymmetries are mainly due to border effects (considering only the central region, all crosstalk events have a symmetric pair causing a double count as explained in the note below). This does not happen for the pads at the edge of the evaluated region, meaning that only when the sampled pad is at one of the borders of the considered region (see Fig. 3.27(a)) there can be an asymmetric contribution to the crosstalk counts. The fact that the values above and below the central cell are greater than those of the left and right cells is due to the channel connection map of the PMT pads (see Fig. 3.12 on the left). Consecutive channels are placed along the vertical direction, therefore, in this kind of analysis, when two channels are hit they are considered as crosstalk even if it is not so; these values will not be considered in the following evaluation of the crosstalk. Moreover, the light asymmetry of the right pads with respect to the left ones is due to the poorer efficiency of layer 2 channels (as already seen in Tab. 3.5) that are connected to the left region of the PMT (see the pad map in Fig. 3.12). This is more evident in the same calculation performed considering different regions of the pad array (Fig. 3.28) whose results are shown in Fig. 3.29: in the LEFT region the asymmetry is much more evident confirming the fact that the cause is the low efficiency of the second layer.

At last, the smaller values found for the corner cells are reasonable due to geometrical considerations.

After these remarks, the crosstalk can be estimated considering the true contribution of up-down-left-right nearby pads as that indicated in the two left and right cells of Fig. 3.27(b) and dividing the average value by a factor 2 (because of the double counting explained before) thus obtaining $\sim 3.6\%$. As far as the corner pads are concerned, the same averaging and division by a factor 2 gives a value of $\sim$2.2%. Summarizing, it could be said that, when a pad is hit, the probability that one of the nearby pads is hit too is $\sim$23%.

Spatial resolution

The spatial resolution in a tracking detector is the precision with which the device can reconstruct the hit position. In a digital detector, that is a detector which gives no information on the energy deposited by the particle but just a yes/no flag for the particle passage, the expected resolution is given by the spread of the

[13] For example, if channels 19 and 27 are hit, this will result, numbering the 3×3 array of cells from 1 to 9 starting from the upper left corner, in a count in cells 5 (the central cell) and 6 when the pad number 19 is considered, and a count in cells 5 and 4 when the considered pad is the 27. There should be always a symmetrical counting, also for the up-down direction; the same is valid for three (or more) hit pads.

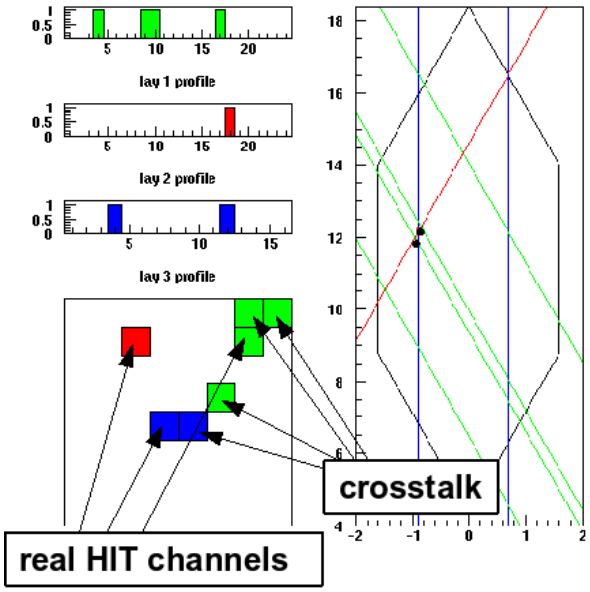

Figure 3.26: Example of an event with crosstalk. The presence of false hits does not prevent the right reconstruction of the hit; the two dark dots represent the two possible triplets reconstructed by the analysis, one true and one induced by the crosstalk: the best triangle (minimum height) will be kept.

reconstructed hit over the channel width (commonly called *pitch*) as sketched in Fig. 3.30. The reconstructed position will have an imprecision given by the variance of the probability distribution of the hit over the channel pitch; if the pitch is d the RMS s is:

$$s = \sqrt{\overline{x^2 - \overline{x}^2}}$$

where the overline indicates the average values. Being $\overline{x} = d/2$, the result is given by the integral:

$$s = \sqrt{\frac{1}{d}\int_0^d (x^2 - d^2/4)\, dx} = d/\sqrt{12}$$

This gives an expected x resolution (the readout pitch is the channel width, so d=2 mm) of 577 μm. As far as the resolution in the y direction is concerned, it can be obtained projecting the x resolution in the y direction (dividing 577 μm by $\tan 20° = 0.364$) which gives a value of 1.59 mm.
The spatial resolution of the prototype was computed selecting the events with one cluster on each silicon plane. In Fig 3.31 the x and y residuals (defined as the

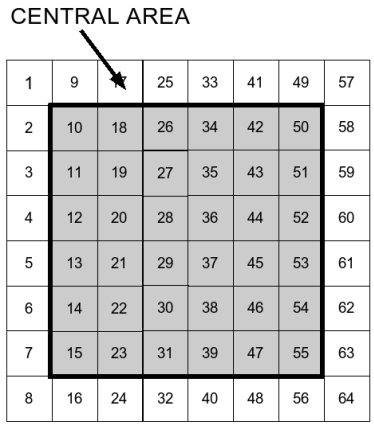

(a) The coloured region shows the pads used for the crosstalk calculation.

(b) The data are normalized to the central cell. Given a hit pad, the surrounding 8 ones are sampled and their readout signal is put in the corresponding position (the criteria to define a channel as "hit" were those described before, that is a cut on the pulse height and a threshold value for the pull).

Figure 3.27: Crosstalk in the central region of the PMT.

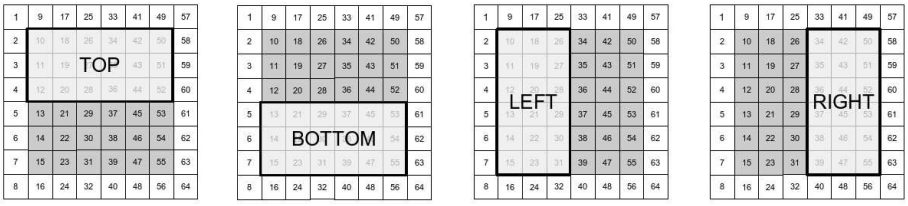

Figure 3.28: Region subsets considered in the crosstalk analysis of Fig. 3.29.

difference between the reconstructed hit and the projection of the silicon detector hit on the prototype plane) are shown: the spatial resolution, which is given by the RMS value of the gaussian fit of the residual distribution, is ~570 μm in the x direction and 1.6 mm in the y one (see Fig. 3.14 for the coordinate system); both the resolutions are in perfect agreement with the expected values.

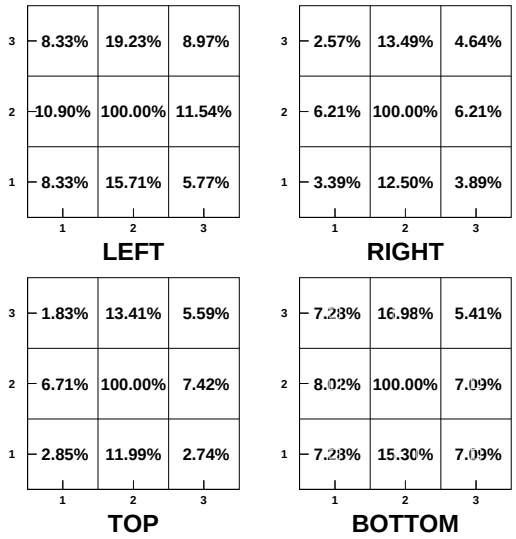

Figure 3.29: The same analysis of Fig. 3.27 has been performed for 4 different regions of the PMT pads. The asymmetry of the LEFT region is due to the poorer efficiency of layer 2.

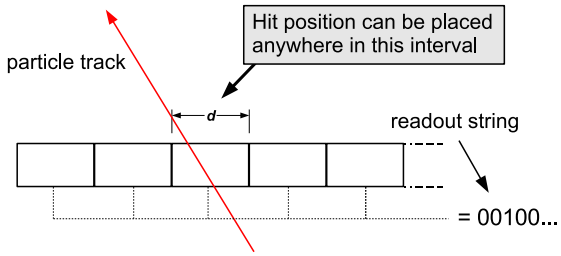

Figure 3.30: Scheme of a (monodimensional) tracking detector with a digital readout. Since the channel pitch is d, the expected spatial resolution is $d/\sqrt{12}$.

3.3 Montecarlo simulation

The Montecarlo simulation of the FAST detector has been performed using the *Geant3.2.1* simulation tool [71]. It is based on the Fortran programming language. In the following some introductory notes will be discussed, while for the complete results see next Chapter.

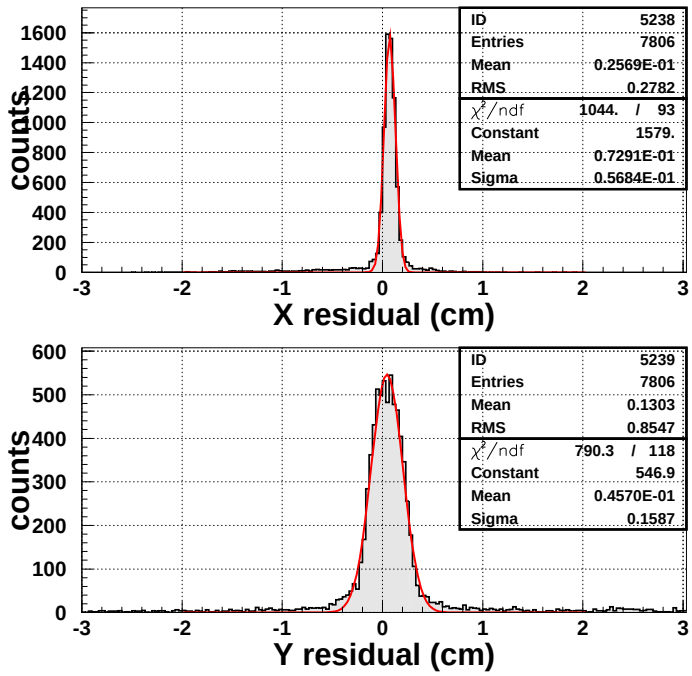

Figure 3.31: Prototype residual distribution. The residual is defined as the difference between the reconstructed hit on the prototype and the projected interaction point obtained with the silicon detectors. The gaussian fits show a x resolution of 570 μm and a y resolution of 1.6 mm; these values are in complete agreement with the expected ones (respectively 577 μm and 1.59 mm).

It should be remarked that, as far as hadronic interactions are concerned, no deep investigation has been done on the accuracy of the *GHEISHA* and *FLUKA*[14] packages that are used in the Geant3 subroutines, nor about the physical models involved: this was not necessary because the aim was to characterize the detectors from a **geometrical** point of view. Anyway some basic validation comparisons have been performed obtaining satisfactory results.

[14]http://www.fluka.org

3.3.1 Passage of particles in the fibers

When charged particles cross matter they lose energy through different processes. Focusing on the energy loss of electrons at 500 MeV of kinetic energy (or 800 MeV/c charged pions), i.e. mips, in thin absorbers (as the scintillating fibers are), the main process by which they lose energy is the collision with the electrons of the atoms. Due to the statistical nature of these processes, large fluctuations can occur in the amount of energy deposited by a particle crossing an absorber element. The Geant routines simulate these fluctuations by using different theories depending on the energy range of the particles and on the characteristics of the absorber: in the case of mips through a thin absorber, Geant computes energy fluctuations according to the Landau theory [72]. The theory generates a probability density function characterized by a narrow peak with a long tail towards positive values; the explicit expression involves a complex integral which will not be treated here; a commonly used parametrization for this distribution is [73]:

$$\Psi(\lambda) = \sqrt{\frac{e^{-(\lambda+e^{-\lambda})}}{2\pi}} \tag{3.1}$$

where $\lambda = R(E - E_p)$, E is the energy (with E_p most probable value of the distribution) and R a constant depending on the absorber. In Fig. 3.32 the energy loss of electrons and negative pions in ~1 mm of scintillating fiber fitted with the function 3.1 is shown; being both mips, the most probable values (the P3 parameter of the fit) are similar within 4% as expected. This fact demonstrates that the use of an electron beam of 500 MeV to test the prototype can be considered a good test for the whole tracker (that will detect charged pions in the momentum range 200 MeV/c – 800 MeV/c).
As far as materials are concerned, Geant provides a set of default materials to build objects; all the others (for example many compounds) are not present and must be defined setting some parameters (composition, density, etc. . .). Both the FAST prototype and the final tracker are built with standard materials apart from the plastic scintillator (polystyrene) for the fibers: in Tab. 3.6 the parameters used for the scintillating fibers are shown.

Channel geometry

A detailed Montecarlo simulation of the 4-fiber channel geometry has been performed. In Fig. 3.33 the scheme and the position of the fibers of a single channel are shown. Fiber centers are positioned at 30° as in the FAST tracker layers, the diameters are 1 mm with 30 μm of cladding, which means that the scintillating

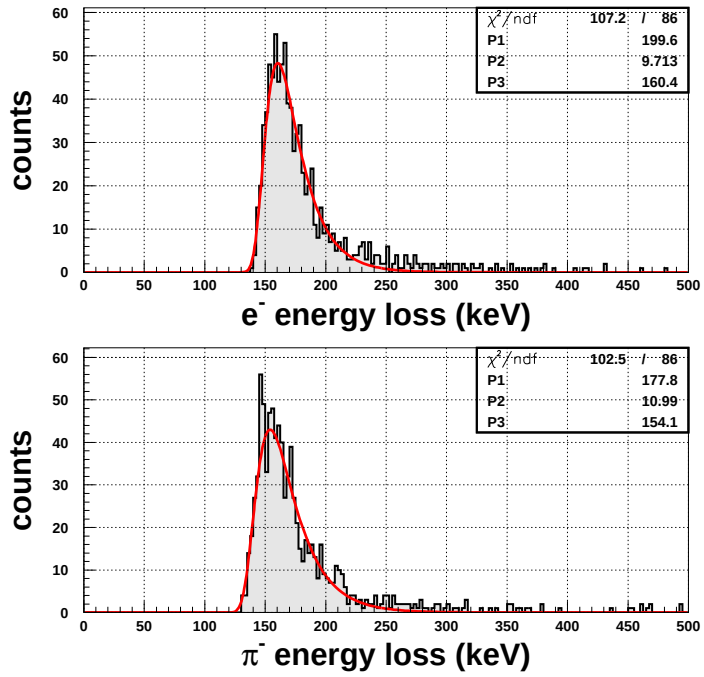

Figure 3.32: Energy loss of 500 MeV electrons and negative pions in 0.94 mm of plastic scintillator fitted with the simplified version of a Landau distribution (Eq. 3.1). The most probable values (P3) differ of only 4%.

material name	Polystyrene
atomic number Z	1 and 6
atomic mass number A	1.00794 and 12.0107
relative weights (%)	7.7418 and 92.2582
density (g/cm^3)	1.06

Table 3.6: Plastic scintillator (polystyrene) parameters set for the Montecarlo simulation. Data from NIST (National Institute of Standards and Technology) database (http://www.physics.nist.gov).

fiber inner diameter is 0.94 mm. The material properties are those of Tab. 3.6. The beam has been chosen as the one used for the prototype tests, that is electrons with a kinetic energy of 500 MeV; the beam incoming direction (z) has been spread with a gaussian distribution with $\sigma_y \sim \sigma_x \sim 1.5$ mm in order to hit all the fibers in the

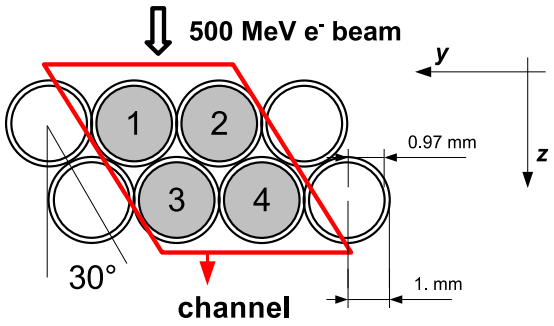

Figure 3.33: Scheme of the 4 fiber layout for a single channel.

same way.
A first result is shown in Fig. 3.34 where in the upper plots the amount of energy deposited within each single fiber of the readout channel is presented. The shape is not a Landau distribution because of the different thickness of the fibers seen by the incoming particles: when the electron passes close to the center of the fiber it will cross 0.94 mm (the inner fiber diameter, the remaining 30+30 μm are the cladding) of plastic scintillator, while this value approaches zero when the hit occurs near the edge of the fiber. There is a most probable peak at ~150 keV that is consistent with the expected average value[15] of 172 keV; there is also a second peak at ~80 keV (less evident in the single fiber plots than the first one) due to a border effect that will be explained in the following. In Fig. 3.35 two detailed plots of the deposited energy as a function of the beam position in the fiber are presented: it can be seen that when the particle crosses the fiber far from the center its average deposited energy is less than when it crosses at the center; moreover the Landau energy loss spread, as computed by Geant, is narrower causing a sum effect in this energy range; in other words, in those regions the spectrum of absorbed energy has a sharper peak. Both slices of Fig. 3.35 have been fitted with the parametrization of Eq. 3.1:

$$f(\lambda) = P_1 \sqrt{\frac{e^{-(\lambda+e^{-\lambda})}}{2\pi}} \tag{3.2}$$

where λ is defined as

$$\lambda = (x - P_3)/P_2$$

and x is the energy. The results are, respectively for the three parameters, 290.0/8.2/67.2 for the slice closer to the edge and 199.6/9.7/160.4 for the central one: as said above,

[15] It is obtained starting from the 1.936 MeV g^{-1} cm^{-2} reported in [41] multiplied by the 0.94 mm thickness and divided by the scintillator density of 1.06 g/cm^3.

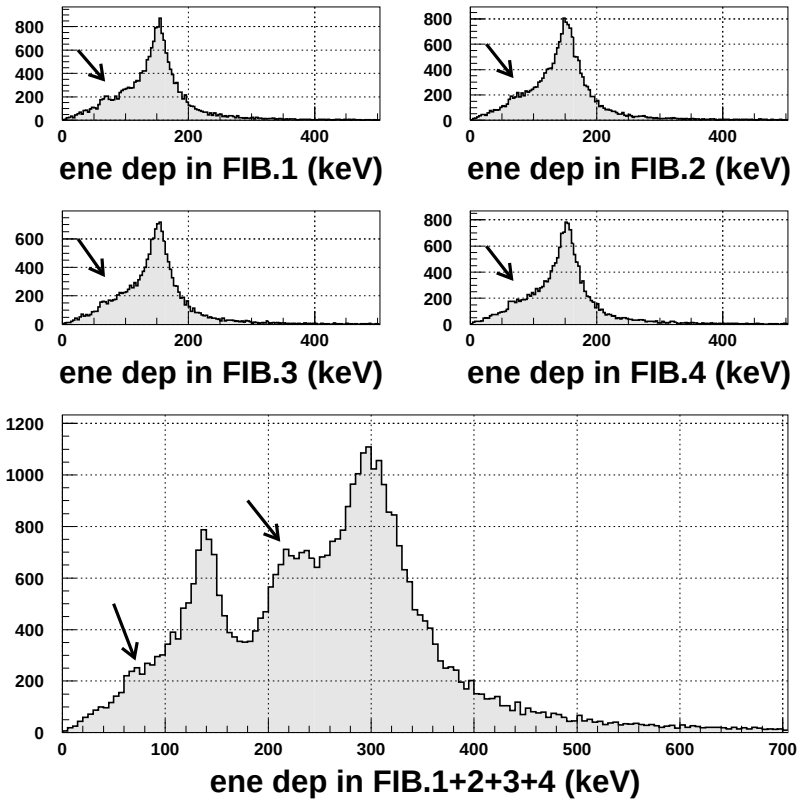

Figure 3.34: Energy deposited in the 4 fibers by the electrons as computed by the Geant simulation (upper plots): their sum event by event (lower plot) is the total energy in the channel. The black arrows indicate the secondary peaks due to the border effect explained in the text.

the slice farther from the center has a narrower peak (P_2 = 8.2). It is interesting to check how this effect causes a non trivial shape of the sum signal plot (lower part of Fig. 3.34): the two main peaks (~300 keV and 150 keV) correspond to 2 times and 1 time the main peak position of the single fiber plot (~150 keV); in fact the particle can cross one or two fibers (see the scheme in Fig. 3.33). As far as the secondary peaks of the fiber plots are concerned, summing the energy of all the 4 fibers event by event, they generate two secondary peaks because of the fiber displacement: the one at ~80 keV is at the same position as the single fiber (the

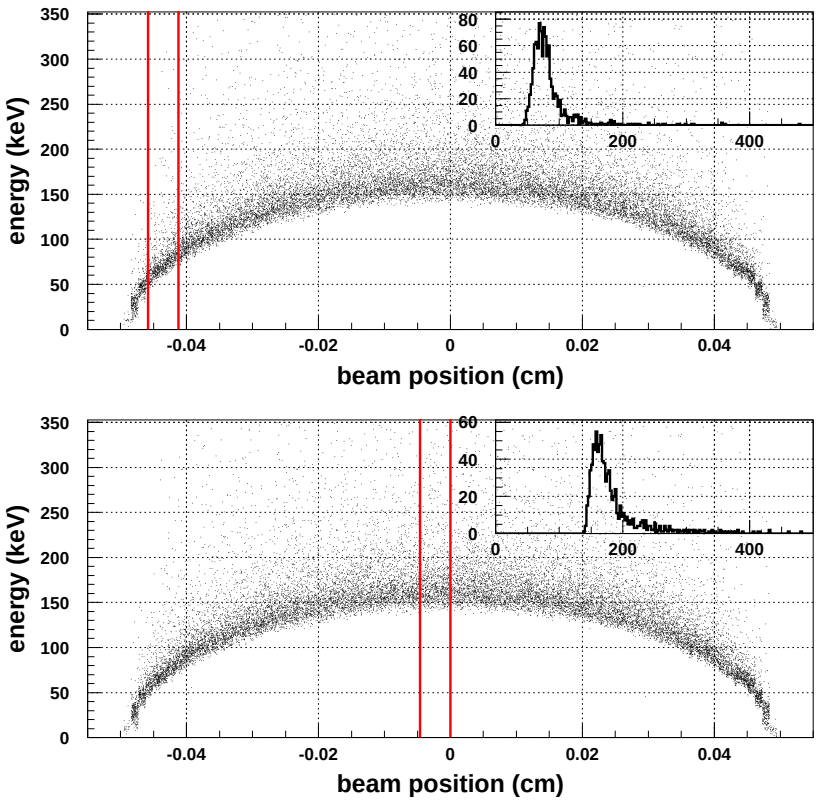

Figure 3.35: Energy loss of a 500 MeV electron through a 0.94 mm diameter scintillating fiber as a function of the incoming position as computed by the Geant simulation. The two slices (the regions between the lines) are shown in the upper right corner of the 2D distribution. It can be noticed that at low energy losses (that is close to the end of the fiber where the average energy loss lies between 50 keV and 100 keV), the Landau distribution is narrower (P1=290, P2=8.2) than the one corresponding to the passage at the center of the fiber (P1=199.6, P2=9.7); this is the cause of the second peak at low energy in the single fiber energy loss 4 plots in Fig. 3.34.

electron has passed at the edge of the channel, that is the left edge of fiber 1 or right edge of fiber 4 in Fig. 3.33); the second one has the energy sum of a fiber secondary peak plus a fiber main peak resulting in a total amount of energy of ~230 keV.

Apart from the secondary peaks, the lower plot of Fig. 3.34 should correspond to the pulse height for the single channel, but the real shape is very different from this one (see as a comparison Fig. 3.19(a)). In fact, the energy released in the fiber produces a certain number of visible photons that travel along the fiber; the ones that reach the PMT anode window will produce a certain number of photoelectrons that are multiplied and generate the output signal. This process depends on, at least, 3 fundamental parameters:

- number of photons produced per unit of energy deposited in the scintillator. As seen in Sec. 3.1.3 this value is 8000 photons per MeV of deposited energy (ph./MeV);
- light collection efficiency. It depends on the fiber macroscopic structure, it has been discussed in Chapt. 2 and a reasonable value lies between 0.03 and 0.04;
- quantum efficiency of the PMT anodes. This value, as described in Sec. 3.1.4, is of the order of 0.2.

Moreover, the photon production in the fiber is a statistical process, whose average value is 8000 ph./MeV; being this a discrete process and since there is no correlation between the production of different photons, the probability distribution is the Poisson one[16]. Considering the probability and the factors described above and inserting them in the simulation, the plots of Fig. 3.34 become the ones shown in Fig 3.36.

3.3.2 FAST tracker simulation

The FAST tracker has been simulated with the already described Geant tool. As previously said, some detector parts and materials have to be defined in order to be as close as possible to the real detector characteristics (first of all the composition of compounds as the polystyrene of the scintillating fibers), some others are simulated with the help of default routines. Two main aspects will be treated before starting analyzing the simulation itself:

- the stereo layer geometry problem;
- the reliability of some physical parameters.

[16]The probability that n independent events, whose average value is λ, occur is given by the Poisson distribution $P(\lambda, n) = \lambda^n / n! \exp(-\lambda)$.

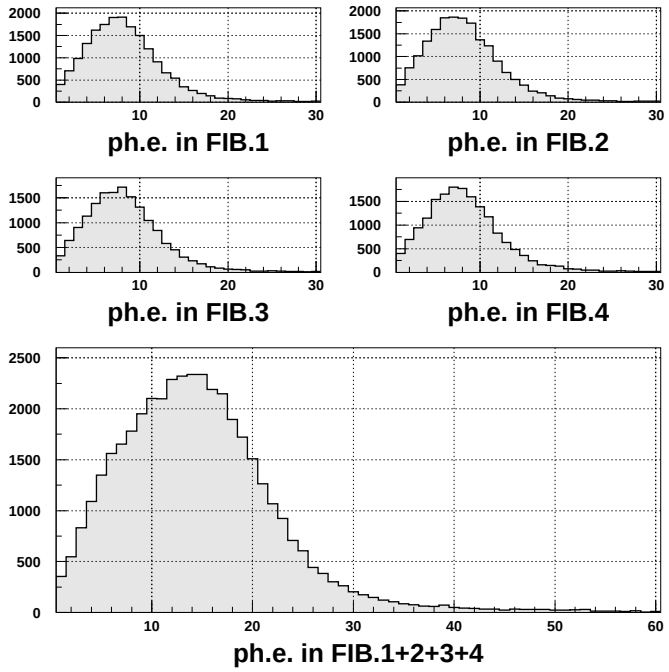

Figure 3.36: Number of photoelectrons produced at the PMT anode due to the 4 fibers (upper plots) and for the readout channel (lower plot).

Layer geometry

In the Geant tool a single scintillating fiber can be easily built setting three basic parameters: inner radius, outer radius, length (due to the geometry layout the z axis will be always used to indicate the beam direction and also the symmetry axis of the detector). The entire layer 3 and 4 (the longitudinal ones) can be fully reproduced, that is all the 1 mm diameter fibers are built and placed at the correct position. In Fig. 3.37(a) a small section of layer 4 is presented. As far as the stereo layers are concerned, the Geant package does not provide any useful pre-built geometrical shape. These scintillating fibers have to be placed along a cylindrical surface (as was clearly sketched in Fig. 3.1); in order to simulate them, a first trial consisted in slicing a single fiber in a set of little cylinders whose centers should have been placed along rotating coordinates just as in the stereo fiber. Obviously this system is useful only if the slices are small enough, that is every cylinder should not have a height greater than ~1 mm; given that there are more than ~1200 fibers

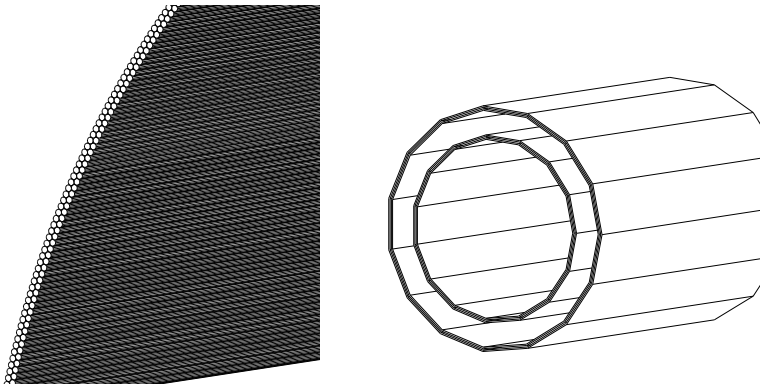

(a) (b)

Figure 3.37: Layer geometry as reproduced with the Geant simulation toolkit. The longitudinal layers are completely designed as the real ones (a), while the stereo layer geometry (b) has to be approximated by a unique scintillator cylinder due to limitations in the provided geometrical shapes.

per layer, if each fiber must be sliced in, at least, 600–800 cylinders, this means ~800000 volumes for a single layer. Each volume has to be stored in memory and processed during the simulation by the Geant program. From the point of view of computing, this approach would have been overwhelming.
Therefore the stereo layers have been reproduced with a unique cylinder, whose radius was the average radius of the layer. In Fig. 3.37(b) a scheme of the stereo layers so simulated is presented.
As will be explained in the following, the main consequence of this difference in the simulated layer structure led to a different way of computing the hit channel: in the longitudinal case it is similar to the real detector (the hits on the fibers are stored, then fibers are grouped and summed to build the channels), while for the stereo ones the hits occur on a cylindrical surface and then their coordinates allow to compute analytically the corresponding channel in each stereo layer.

Note on hadronic interaction

As far as QED (Quantum ElectroDynamics) physics is concerned, the Geant software was studied and developed during the '80s and '90s, that is to say that, as far as interaction between high energy leptons and matter is concerned, the simulation results are completely reliable.
It has already been stated than no deep investigation on some of the physical pro-

cesses, such as hadronic interactions, was done. This was due mainly to the fact that the aim of the simulation was to characterize and validate the geometry of the detector. Moreover, the physical processes under investigation, $\bar{p}p$ annihilation cross section in gases and solids (and corresponding material stopping powers), involve non trivial QCD models that are far from being treated in this work. Anyway some basic comparisons between the Geant simulation and the available data have been done to be sure to be on the right track.
The data taking that will be described in Chapter 4 has been planned to detect charged pions coming from $\bar{p}p$ annihilations inside a gaseous target (hydrogen, helium, etc. . .); therefore a fundamental parameter is the number of pions produced in such a process. The most recent reviews report an average total number of produced pions per annihilation at rest in hydrogen of [18]:

$$n(\pi^{\pm})/\text{annihil.} = 3.05 \pm 0.04$$

$$n(\pi^{0})/\text{annihil.} = 1.93 \pm 0.12$$

The Geant simulation gives:

$$n(\pi^{\pm})/\text{annihil.} = 3.05$$

$$n(\pi^{0})/\text{annihil.} = 1.84$$

In Fig 3.38 the total pion multiplicity arising from a single $\bar{p}p$ annihilation at rest in hydrogen, both from the experimental data and from the Geant simulation, is shown. The details of the simulation setup and settings will be given afterwards. Since the two distributions are different, it is clear that the simulation has to be tuned, but this goes beyond the goal of this work.
Another possible comparison can be performed on the charged pion momentum distribution; in Fig. 3.39 the data from [18] and the Geant simulation are presented. The two distributions are very similar.

Geometrical efficiency of the tracker

It is important to compute the expected tracker geometrical efficiency because the reconstruction efficiency (it will be discussed in the next Chapter) is strictly connected with it.
The geometrical efficiency is defined as the fraction of events (in this case an event is represented by the generation of a charged pion in the sensitive volume) that is within the solid angle covered by the detector; in other words, dividing the number

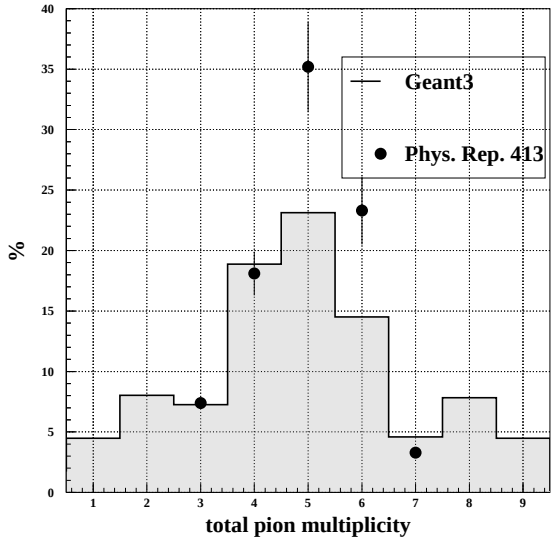

Figure 3.38: Results for the Geant simulation of $\bar{p}p$ annihilation at rest in hydrogen: (a) total pion multiplicity (line) compared with the results reported in [18] (dark dots).

of charged pions that have crossed all the 6 layers by the number of the generated ones will result in the geometrical efficiency.
In Fig. 3.40(a) a scheme of the relevant details of the layers is shown; the so called dead zones are the two spherical caps (referring to Fig. 3.40(a)) at the sensitive volume edges; each of these areas has a surface:

$$A_{sph.cap} = 2\pi r$$

where r and h are the corresponding radius and height (its value depends on the z position) of the spherical caps (left and right). Thus the geometrical efficiency, as a function of the z coordinate, is:

$$\begin{aligned} \epsilon_{geom} &= \frac{A_{tot}/2 - A_{sph.cap\ LEFT}}{A_{tot}/2} + \frac{A_{tot}/2 - A_{sph.cap\ RIGHT}}{A_{tot}/2} \\ &= \frac{R_2(L-2z) + R_1(L+2z)}{4R_1R_2} \end{aligned} \tag{3.3}$$

where

$$R_1 = \sqrt{(L/2-z)^2 + r_{out}^2} \qquad ; \qquad R_2 = \sqrt{(L/2+z)^2 + r_{out}^2}$$

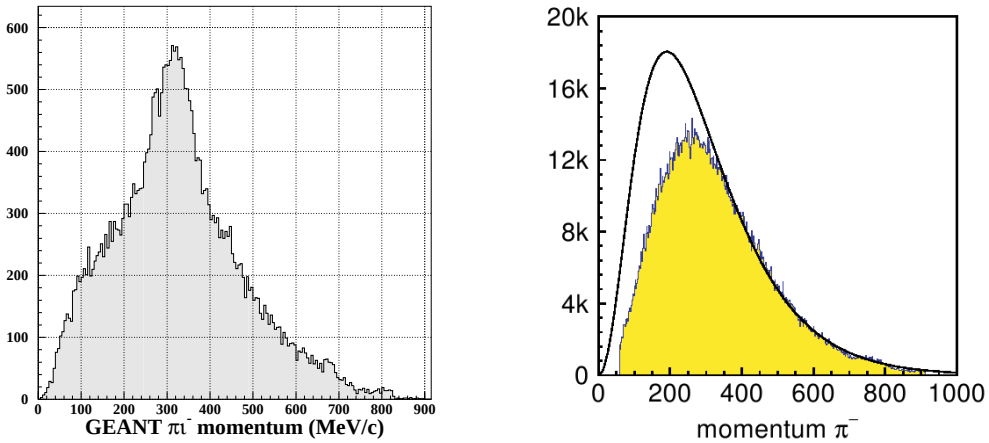

(a) (b)

Figure 3.39: Momentum distribution of charged pions produced in $\bar{p}p$ annihilations at rest in hydrogen as computed by the Geant simulation software (a) and as reported in [18] (b) (the superimposed line is a fit with a Poisson distribution).

If pions (from $\bar{p}p$ annihilations) are generated at the center of the tracker (z=0) then ϵ_{geom}=85%, while at the edges of the sensitive volume (z=±25 cm) the value becomes 48%.
A comparison has been done with the value obtained with the Geant simulation; placing the antiprotons at rest along the z axis and filling the volume with low pressure hydrogen (these setup details will be discussed in the next Chapter), an evaluation of the geometrical efficiency can be performed counting how many charged pions cross all the 6 layers with respect to the produced ones. The results are presented in Fig. 3.40(b) showing an optimum agreement apart for the border region ($|z| > 25$ cm) due to the correction for the finite thickness of the layers that is not taken into account in the theoretical calculation; anyway that region is far away from the center of the tracker where all the events will be searched for. This demonstrates the reliability of the Geant simulation, especially as far as the geometrical parameters are concerned.

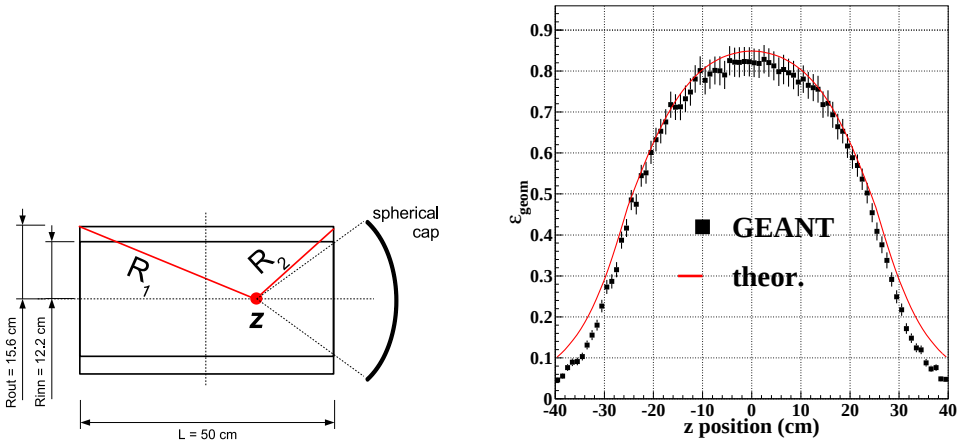

(a) (b)

Figure 3.40: (a) Schematical view of the FAST tracker; (b) geometrical efficiency ϵ_{geom} computed with the Geant simulation (black squares) with the superimposed line indicating the theoretical values of Eq. 3.3 (the error bars are computed as the poissonian spread of the counts of charged pions).

Chapter 4

FAST commissioning and physics run

The commissioning of the FAST tracker, described in the first part of this Chapter, has been performed with cosmic rays, in order to evaluate the global behaviour of the detector and to measure its spatial resolution. This commissioning has been continued also after the first data taking period (September 2006), whose beam conditions have not allowed to collect any data for physics. The results of the cosmic ray run will be presented and compared with the simulation.
The second part of the Chapter will present the data taking for physics at the CERN AD. As already said, the experiment started in September 2006 and, at present, two data taking runs have been concluded with two different goals:

- the first one has focused more on the detector performances than on physics results because of the AD beam conditions;
- in the July 2007 run, the beam problems have been solved and data for physics could be collected; since the analysis is still ongoing, only preliminary results will be presented.

4.1 Cosmic ray data taking

The commissioning of the FAST tracker started in August 2006. After having completed the detector assembly, two cosmic ray data taking periods of around 20 days each (the first one took place just before the September 2006 run, while the second one in April 2007) allowed a deep analysis of the tracker performances by means of other reference detectors (plastic scintillators and silicon detectors). As far as the electronics is concerned, both the analog and digital operational modes have been used.

The goal of the cosmic ray run was to characterize the FAST tracker especially concerning:

- the spatial resolution;
- the synchronization of the whole system (frontend and repeater boards);
- the crosstalk;
- the efficiency.

This first run has also helped in understanding some assembly problems that will be described in the following sections.

4.1.1 Final assembly

The commissioning of the FAST tracker started in August 2006. The detector assembly has been concluded with the connection of the whole electronics system to the tracker (Fig. 4.1(d)). At first the frontend boards have been placed in front of the PMT side of the tracker by means of a custom aluminum support (Fig. 4.1(a)); then the PMTs have been connected to the frontend boards with 26 pin ERNI cables (Fig. 4.1(b)). All the cable lengths have been studied in order to leave as much free space as possible in the inner region of the tracker where, in the final configuration, the target vessel should be placed (see Sec. 4.2). The darkening, as well as the electromagnetic shielding, was provided by a metallic structure covered by black tissue surrounding the frontend boards (Fig. 4.1(c)). At last, the whole electronics readout system was connected to the detector (Fig. 4.1(d)); the repeater boards have been placed above the tracker box, while the rest of the electronics was hosted in a rack close to the detector. All the positions, from the frontend boards to the DAQ PC, have been studied taking into account what would be the available space in the AD experimental area (see Sec. 4.2).

4.1.2 Experimental setup

The cosmic ray data taking setups are shown in Fig. 4.2. Three main configurations have been used: in all of them the detector tests were performed with the help of other detectors among which plastic scintillators (mainly as a triggering system) and silicon strip detectors (as a reference for the tracking). In the following, a brief description of these detectors will be reported, together with the analysis software developed for this run.

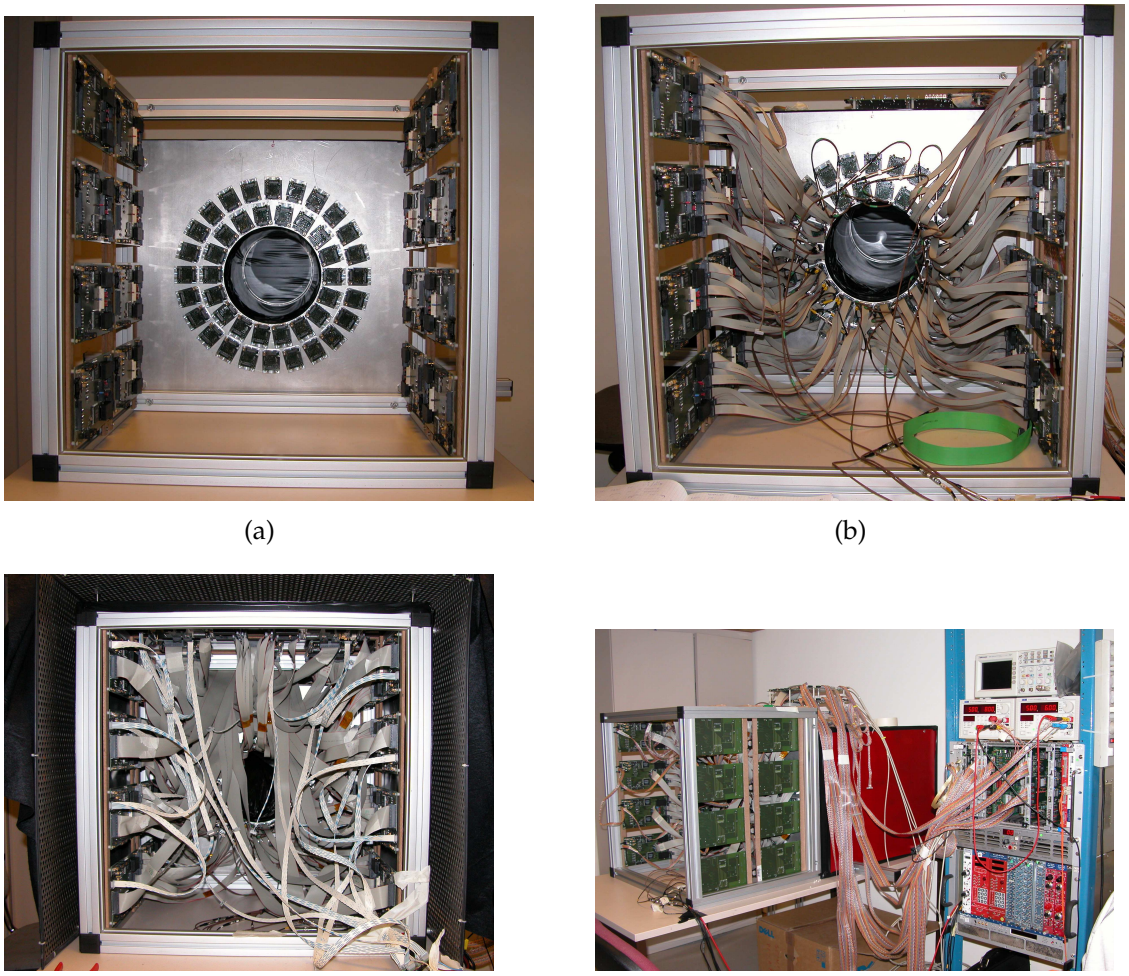

(a) (b)

(c) (d)

Figure 4.1: Final detector assembly before the cosmic ray data taking. (a) Al support hosting the frontend boards facing the PMT side of the tracker. (b) Cabling phase. (c) Electromagnetic shielding and darkening. (d) Complete electronics system connected to the detector. The DAQ PC was close to the rack.

Plastic scintillator counters

As already seen in Chapt. 2, in organic scintillators crossed by a high energy particle, visible photons are produced by means of the fluorescence mechanism. This occurs in a very short time (~10–100 ns), thus providing an optimal timing reference. Scintillators are typically used as a triggering device.

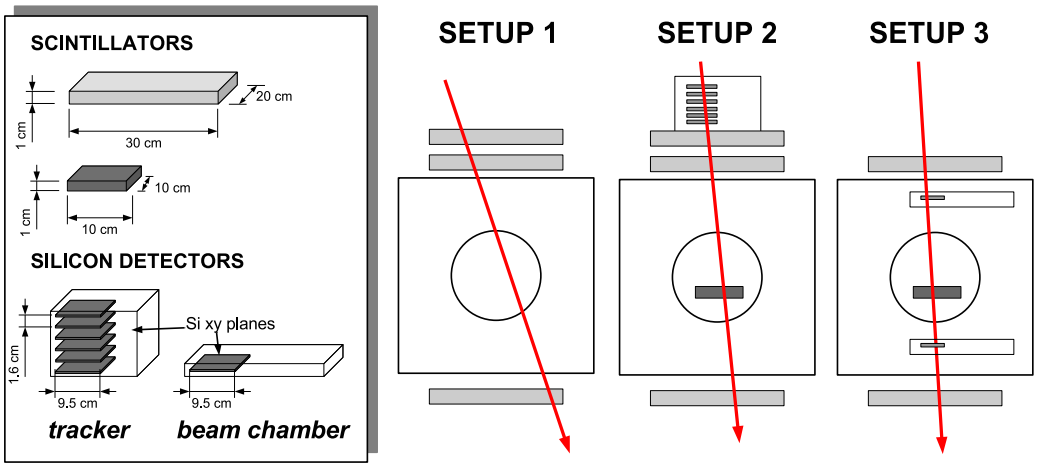

(a) Overview of detectors and setups layouts.

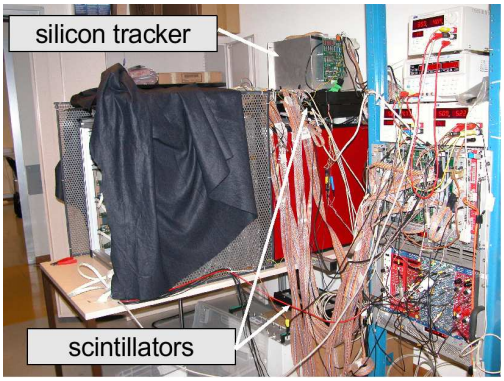

(b) Setup 2

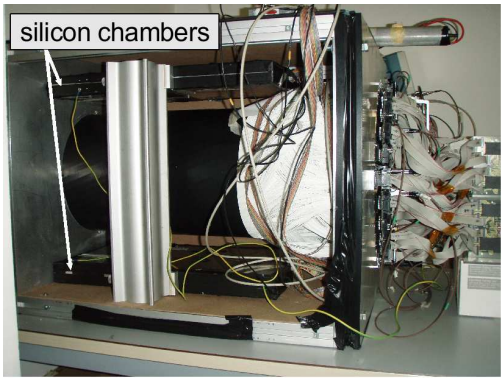

(c) Setup 3

Figure 4.2: Cosmic ray data taking different setups.

In the FAST cosmic ray data taking, two types of plastic scintillation detectors were used:

- the first one consists in a 1×20×30 cm^3 scintillator (polystyrene) readout by an Electron Tubes P30CW5 photomultiplier. The scintillator and the PMT are positioned in a PVC box (Fig. 4.3);
- the second scintillation counter is made of polystyrene as the first one. Two similar models have been used whose sensitive part dimensions were 1×10×10 cm^3 and 1×3×10 cm^3; the light produced by the crossing particles is readout by two photomultipliers.

(a) (b)

Figure 4.3: (a) Photo of two 1×20×30 cm^3 scintillators; (b) detail of the photomultiplier coupled to the scintillator.

Silicon detectors

In almost all physics experiments in which particle tracking is involved, a silicon tracker is present: it typically consists in two or more sensitive silicon planes, being each plane a high spatial resolution (strip or pixel) detector assembly.
The silicon detectors used in the FAST commissioning phase were the following:

- the first one consists in 12 9.5×9.5 cm^2 silicon strip detectors (6 x planes and 6 y planes) with a readout pitch of 242 μm and one floating strip, and polysilicon resistors for the bias (Fig. 4.4)[1]. Each tile is AC-coupled to the electronics and readout by three low noise self triggering ASICs[2] with full analog readout. The spatial resolution of each plane is 40 μm. The 12 detectors are organized in 6 x-y trays reproducing the AGILE satellite tracker tray structure. Each tray consists of 1.3 cm of Al honeycomb and 500 μm of carbon fiber on each side. On one of the tray sides, a tungsten layer of 300 μm is glued to allow the tracker to work as such for the photon detection. The pitch of the trays is 1.6 cm. The frontend electronics is positioned on the tray itself on a FR4 PCB. The readout electronics is the same of the silicon chambers used at the BTF line for the prototype tests. 10 of the 12 layers (5 x and 5 y) have been readout in the cosmic ray run since the VME ADC (V550 by CAEN) accepts a maximum of 2016 channels per ADC input (that is 384×5). This detector has been used in setup 2 of Fig. 4.2;

[1] It has been built for the AGILE satellite commissioning phase [70]
[2] TAA1 IDEAS - Norway

(a)

(b)

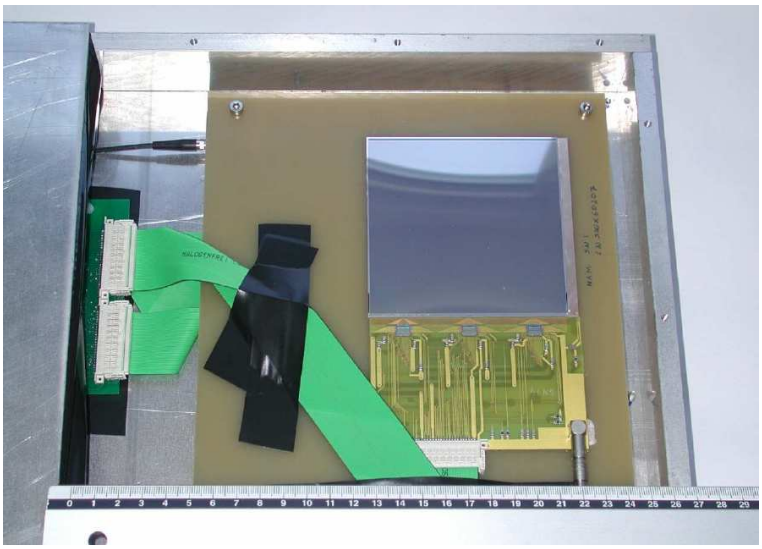

(c)

Figure 4.4: Photos of the silicon detectors used in the cosmic ray data taking: (a), (b) two photos (side, top) of the 12 microstrip planes of the tracker; (c) sensitive plane of the second detector type used in the cosmic ray data taking.

- the second silicon detector (Fig. 4.4(c)) is a beam chamber built for the AGILE satellite testing runs [70] based on the same tile and frontend electronics of

the silicon tracker described above. Two tiles, in a x-y configuration, are glued on the two sides of an epoxy fiberglass support, with the electronics located in front of them.

Electronics

The electronics acquisition system has been already described in Sec. 3.1.5 and sketched in Fig. 3.5.
The logic of the acquisition had to be tuned in order to cope with the different triggering system of this commissioning phase. In fact, when a muon crosses the scintillators, a trigger signal is generated; this signal is used by a VME sequencer to generate the hold for the silicon detector while it arrives after the signal generation on the FAST frontend boards. In other words, the acquired FAST events would be always empty because not properly synchronized with the trigger. In order to solve this problem the sampling logic loaded in the Cyclone II FPGAs is different from the one used in the final data taking. In the standard logic the shift registers which perform the sampling are activated only after the trigger signal is received. In the cosmic run logic the registers are always running, apart during the time needed for the boards readout by the VME system. Once a trigger is received, a counter, with the clock synchronous with the register one, is started: when the counter reaches 128, that is half of the registers depth, the clock to the registers is stopped and the boards wait for the readout.
This means that the fiber signal, if present, will be found somewhere before the half of the shift registers. One drawback of this logic is that the 320 MHz clock on the FPGAs is running most of the time, thus increasing by a factor 3÷4 the power consumption of the sampling system.

Analysis software

As previously described in Sec. 3.1.5, the DAQ software produces, at the end of each run, a set of PAW ntuples, that have been analyzed with a software written in Fortran[3].
The analysis software has been studied to cope with data taken in two different configurations, that is the analog operational mode and the digital one. The outputs of the two modes are very different (see Sec. 3.1.5) and have required the development of several packages of software. Moreover, during the commissioning phase, the two configurations have been used stand alone or in combination to

[3] http://www.fortran.com

define completely the tracker behaviour.
Among the goals of the cosmic ray run, the measurements of the spatial resolution and of the efficiency have been listed. This has required the use of other high precision detectors, such as the silicon tracker or the silicon beam chambers, whose output data had to be included in the ntuple. To cope with all these possibilities, a single analysis program capable to handle all the raw data formats and all the used detectors, and to compare the analog data with the digital ones and with the reference detector ones has been developed.
As far as the raw data format is concerned, the following items are contained in the two cases (analog and digital):

- analog raw data format
  The column-wise ntuple contains, event by event, the ADC counts of each channel of FAST and of the silicon tracker together with some general information such as the event number, the absolute time and the time from the beginning of the run;

- digital raw data format.
  As already explained in Sec. 3.1.5, the digital data are the result of the sampling of all the PMT channels for a 800 ns window at a sampling rate of 640 MHz. This means that, event by event, 512 bits are stored for each channel for a total of 172 kB. These data are packed in 32 words of 16 bits and stored in a dedicated column-wise PAW ntuple together with the run information (number of event, time of the event, etc.) as in the analog case.

The analysis software has been organized in independent blocks as sketched in Fig. 4.5. The aim was to separate the different parts of the program in order to obtain a more versatile program. All the steps of the analysis can be verified with dedicated graphical tools (see Fig. 4.6 and Fig. 4.7). The structure of the program can be roughly described in this way:

1. The raw data format is recognized (analog/digital)

2. The raw data are put together with the corresponding pedestal and/or RMS values (if necessary) and other detectors data outputs

3. The raw data of the tracker are transformed in a digital-like hit array; in other words, the event on the tracker is represented, being it a single trigger of a muon crossing the system in the commissioning phase case and one single sample in the final data taking configuration, by a 1/0 string for each layer where 1 stands for *hit* and 0 for *not hit*. This is achieved by means

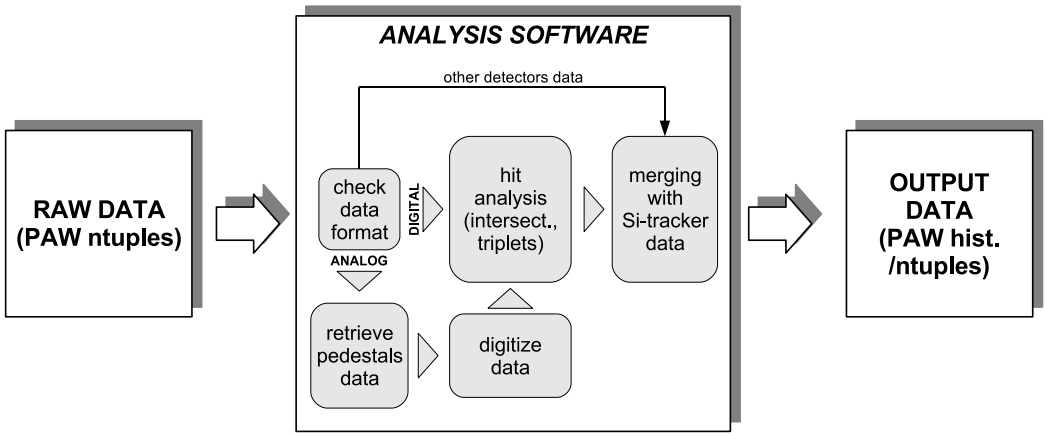

Figure 4.5: Analysis software block diagram.

of a "map file" that indicates which fiber corresponds to which electronics readout channel

4. The next step is the hit analysis, as described in the prototype case (see Sec. 3.2): all intersections are found to compute all the reconstructable triplets (see Fig. 4.6).

5. The data from the reference silicon tracker (see Fig. 4.7) are retrieved and merged with the FAST ones for the final analysis (residuals computation, efficiency, etc.)

6. The output of the analysis is stored in PAW histograms (or PAW ntuple) files.

4.1.3 Results

Layer alignment problem

In Fig. 4.8(a) a top view of one of the FAST tracker layers is sketched; from now on, the angle 0° (or channel number 0) of a layer, will represent the TOP of the layer, while 180° (or a channel number equal to half the total number of channels as reported in Tab. 3.1) will be the BOTTOM part of the layer.
The first step of the data analysis consisted in observing the layer profile plots, that is the spatial distribution of the hit channels on the single layer. In Fig. 4.8(b) the profiles of all the 6 layers are shown: as one should expect, since muons cross the

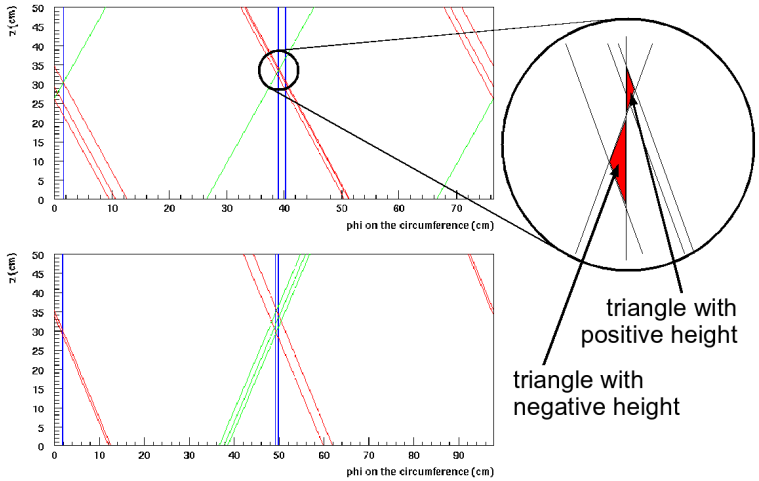

Figure 4.6: Graphic event display. The cylindrical surfaces of the two shells are shown: the inner in the upper part and the outer in the lower one. The units on both axes are cm. On the left the convention used for the triangle heights is shown: positive when the stereo intersection is at a larger ϕ than the longitudinal one (that is, in this representation of the surface of the cylinder, towards positive abscissa values), and negative in the opposite case.

tracker in the vertical direction[4], most of the hits are placed at 0° and 180°. Since the plots x axis is expressed in terms of channel number, this corresponds to the numbers around 0 and the maximum value (as shown in Tab. 3.1) for the top part, and to the ones in the middle for the bottom one. Moreover, it can be noticed that:

- layer 1, 2, 4 and 6 present a non perfect matching between the last channel and the first one (the empty zone corresponding to the first channels of layer 5 is due to a not working PMT): in fact, since the plots represent a cylindrical surface, the right edge should be in perfect agreement with the left one, which is not the case for these layers;
- apart from some isolated channels that show a very large number of counts (due to noise; these channels can be switched off offline), in all layers there are irregular shapes, that is small sets of channels whose trend is the opposite of the expected one: for example, in the region around channel 50 of layer 3, there is a group of ~20 channels whose hits are increasing moving toward

[4]The angular distribution of the cosmic ray muons is proportional to $\cos^2(\theta)$, where θ=0° represents the zenith direction.

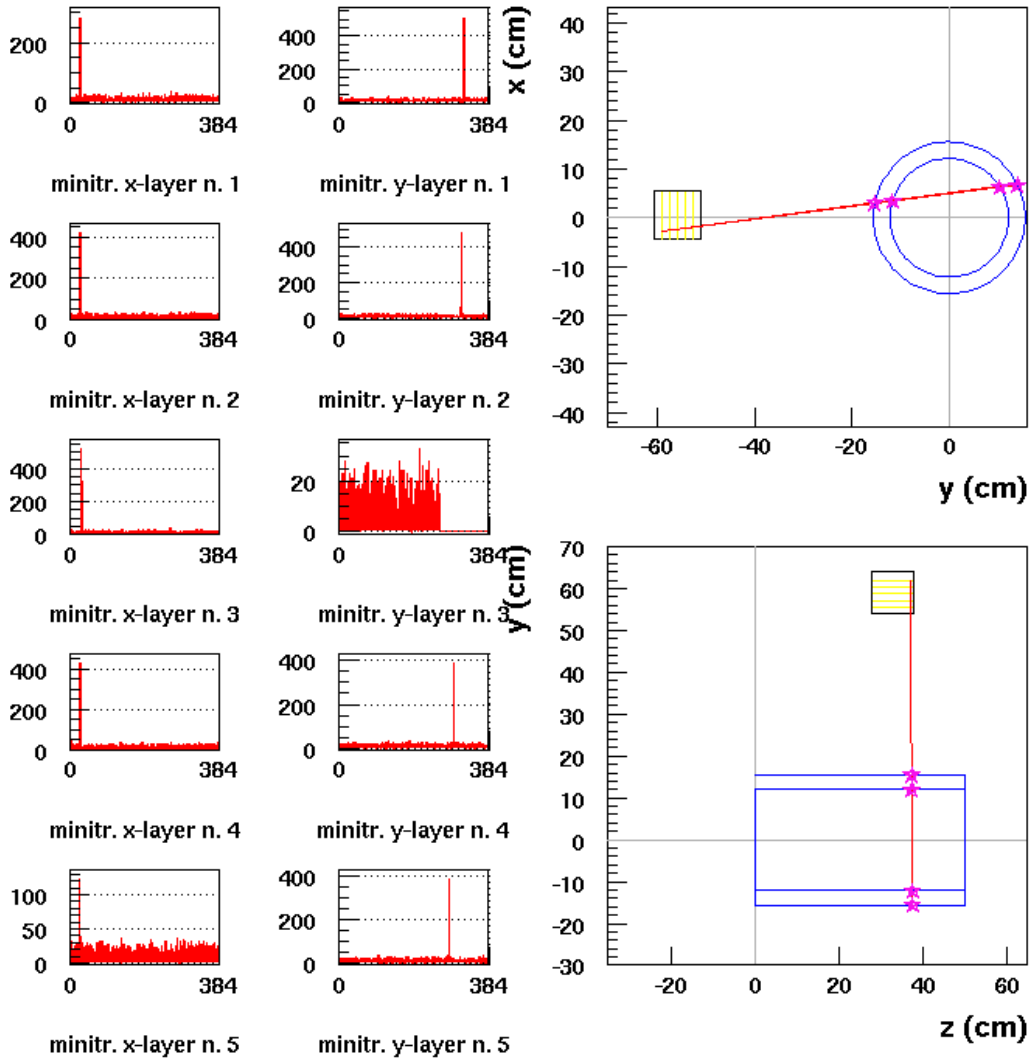

Figure 4.7: Analysis software event display. Left: muon hit on the 10 planes of the silicon tracker; if at least 3 x planes and 3 y planes have a signal, the trajectory can be computed by means of a linear fit. The x axis is the number of strip while the y axis is the ADC value of the strip (the absence of the event in layer 3 on the y side is due to a dead ASIC). Right: xy and yz projections of both the FAST tracker and the silicon tracker (see Fig. 4.8(a) for the coordinate system). The line represents the trajectory of the particle as reconstructed by the silicon planes; the crossing points on the FAST tracker are marked with a star.

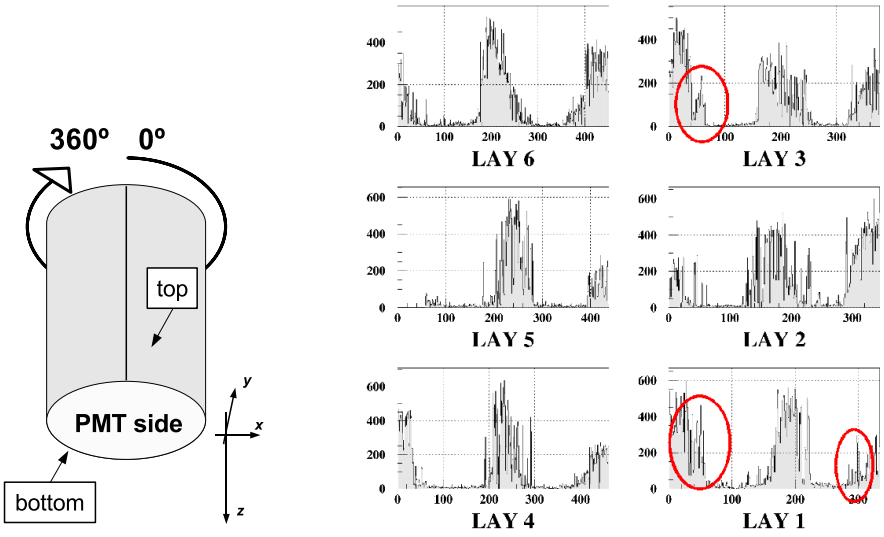

(a) (b)

Figure 4.8: The used convention for the angles (channels) is the one indicated in (a). (b) Profile plots of the 6 layers; on the x axis the number of channels is reported. Some regions are highlighted (circles) to indicate the misalignment discussed in the text.

the positive direction. This cannot be a physical effect and can be explained as an artifact due to a wrong mapping;

- as far as the axial layers (layer 3 and 4) are concerned, they should have a peak of counts centered at 0 (0°) and, respectively, 188.5 and 230.5 (180°).

These are all alignment problems which can be only partially solved; in fact, if layers are only globally shifted, clockwise or counterclockwise with respect to the zero position, they can be adjusted offline; but if only some subsets of channels are wrongly mapped the problem is not trivial. The mapping and misalignment effects are the result of an assembly procedure which could not be verified at each step since the electronics was not ready. To try to solve these inconsistencies, both analog and digital data have been used. Analog data have been acquired with setup 1 of Fig. 4.2, while in setup 2 and setup 3 FAST worked in digital mode. Setup 1 has a larger angle of acceptance than setup 2 and setup 3. This results in a wider spread of the hits over the channels as shown in Fig. 4.9, making any

alignment adjustment more difficult to perform.

The data taken with the other 2 setups (that is with the silicon detectors) have

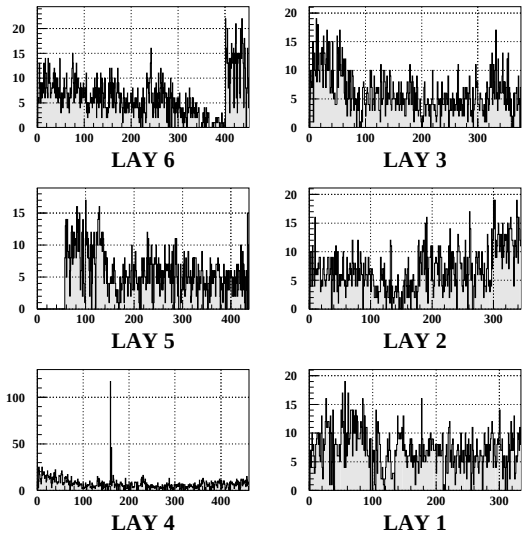

Figure 4.9: Profile plots of the 6 FAST tracker layers in the analog acquisition as arranged in setup 1 of Fig. 4.2.

been used to remove the alignment imperfections where possible. In Fig. 4.10(a) the profiles of layers 3 and 4 are shown: layer 3 is rotated towards the positive x direction of ~9-12 channels (that correspond to a rotation of 9–10°). Another proof of this fact can be found analyzing the hits on the layers. As already described, all stereo intersections are matched with the longitudinal channels in order to build the triangles (triplets); the smaller is the triangle height (that is the distance between the intersection and the longitudinal channel in the ϕ direction) the better is the triangle. In this way the plots in Fig 4.10(b) are obtained in which two kinds of triangle heights are shown: all the buildable ones (that means with no selection, apart for an obvious cut for heights greater than half the circumference) in light gray and the best one (that means, event by event, the smallest one) in dark gray. It is clear that the hits reconstructed on the inner shell present a systematic offset towards the negative values (the height has been defined as the result of the subtraction of the longitudinal channel position from the stereo intersection position as previously shown in Fig. 4.6).

At a first glance, one could say that rotating layer 3 of a suitable number of

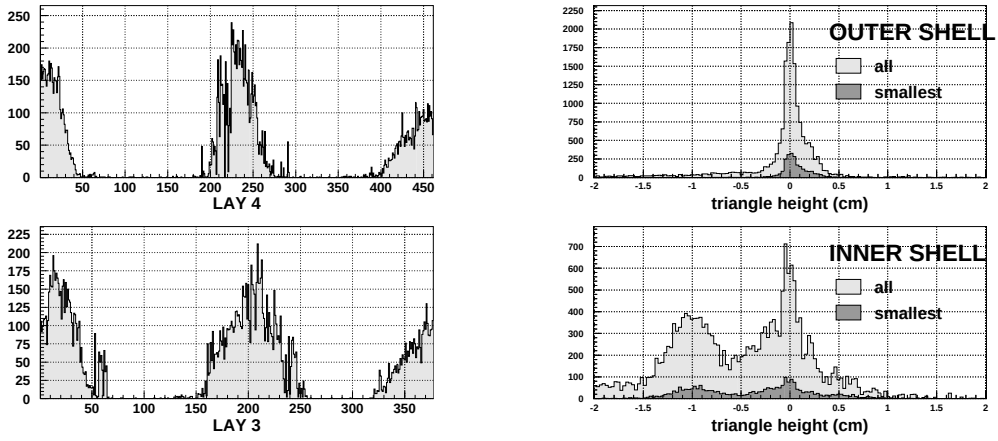

(a) (b)

Figure 4.10: Evidence of the misalignment of layer 3 and 4. (a) Profile plots; (b) all triangle heights are shown in light gray while the darker area represents the smallest one event by event.

channels would solve the problem. This would be true if only layer 3 and 4 were wrongly mapped, in other words, if the stereo layers are considered in the right position. On the other hand, with the help of the graphical event display (see Fig. 4.6) it has been demonstrated that, assuming that all layers can be rotated, the problem of minimizing the triangle heights is not trivial and has many possible solutions. Moreover, as far as the alignment is concerned, the available silicon detectors (the tracker and the beam chambers) can be used as a reference for the position of the hits, that is, also the triangle positions, and not only their heights, must be taken into account. In Fig. 4.11 the same plot of Fig. 4.10(b) is presented after having rotated layer 3 of a suitable value (it was found, observing the profile plot of layer 3 compared to that of layer 4 as in Fig. 4.10(a), that a good value was 11 channels towards the negative angles): the systematic error in the triangle heights has shifted to the right, but has not been removed. Therefore more than one layer needs to be rotated.

Considering all these facts, the alignment problem has been faced with the following constraints:

- Even if, from a theoretical point of view, all the layers can be rotated in the offline analysis, it is better to modify as few layers as possible. Thus, on the

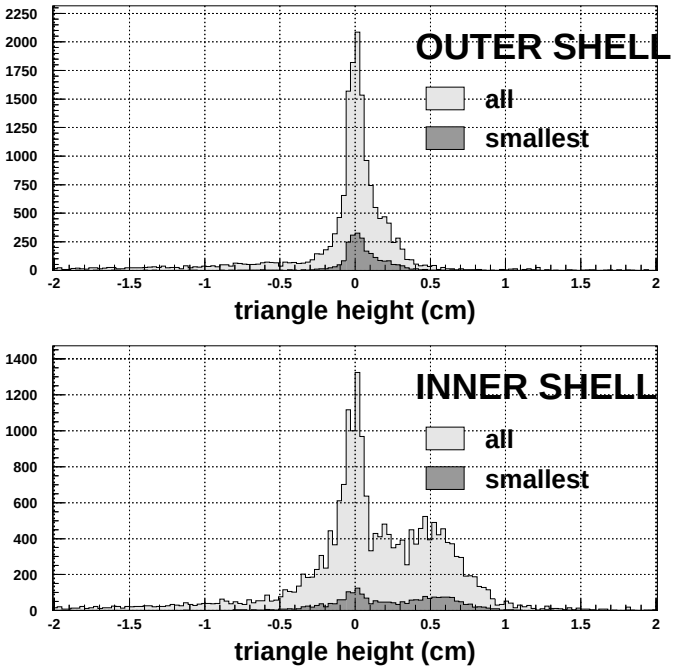

Figure 4.11: Triangle height after having rotated layer 3 of 11 channels backward (that means towards negative x values in the profile plots). All triangle heights are shown in light gray, while the dark colour indicates the smallest one.

basis of the shown plots, it has been decided to leave all the outer layers fixed and to make some trials only on the inner ones.

- Layer 3 presents an evident wrong mapping and must be rotated.
- As far as the inner stereo layers are concerned, layer 1 is the one that is likely to have been arranged with the best accuracy because it was the first placed on the support during the assembly phase.

At the end of the procedure, only layer 2 and 3 have been rotated of different angles (that will be always expressed in terms of number of channels) in order to find the best possible solution.
To check each step the following analysis on the triangle position has been performed: once the best triangle on the outer shell was found, its projected position on the inner shell was computed. The projection was extrapolated tracing a line

connecting the outer triangles and finding where this line crossed the inner shell of the tracker. If a triangle was reconstructed also on the inner shell, the distance from the previous computed one was stored and the obtained 2D distributions (a sort of residual plot) are shown in Fig. 4.12. Several trials have been made among

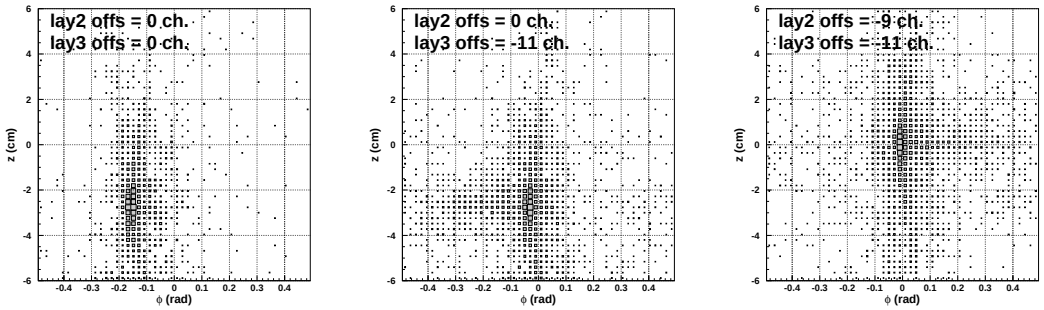

(a) (b) (c)

Figure 4.12: 2D residual distributions of the outer triangles projected on the inner shell with respect to the inner triangles. Different offsets (rotations), for layer 2 and 3, have been tried. Respectively: (a) 0,0 (none rotated); (b) 0,-11 (only layer 3); (c) -9, -11 (both rotated).

which the examples shown in the plots. At last, it seemed that the best variation on the original map was to rotate layer 2 and 3 respectively of 9 and 11 channels backwards, as shown in Fig. 4.12(c).

Efficiency

As far as efficiency is concerned, in both setup 2 and setup 3 of Fig. 4.2, the muons detected by the silicon detectors have been selected in order to be sure that the particle has crossed all the layers. Then, once defined an "acceptance angle" (see Fig. 4.13), the events with a hit in both the upper zone and the lower one of each layer have been counted. This analysis has been performed for different angles, from 0° to a maximum of 30° (it would be meaningless increasing the angles because above this limit the counted events will be always the same, since the size of the silicon detectors and/or the triggering scintillators allow to hit only a limited region of the scintillating fiber layers. This can be seen in the profile plots as those shown in Fig. 4.8). In Fig. 4.14 the number of counts (as a percentage of the total number of events) as a function of the acceptance angle is shown for a run taken

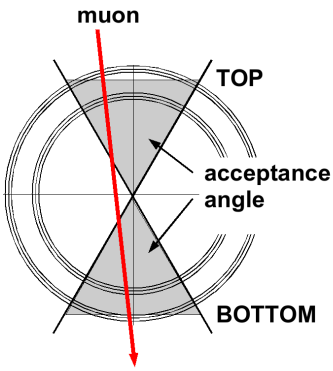

Figure 4.13: Scheme of the acceptance angle defined in the text.

with different setups (setup 2 and setup 3 of Fig. 4.2): the counts increase with the angle, but from a maximum angle (determined by the geometry of the system) on, the asymptotic values are reached. A single layer efficiency can be extrapolated

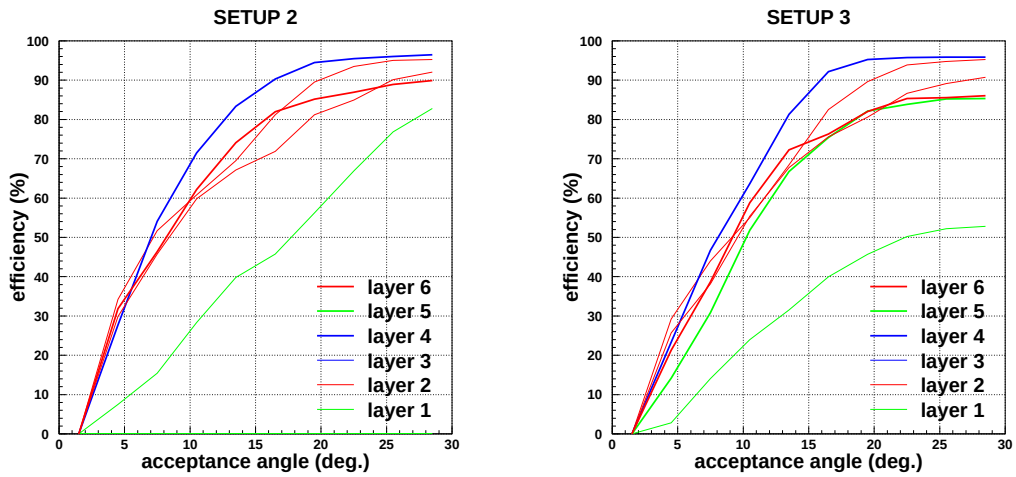

(a) (b)

Figure 4.14: Efficiency of the 6 layers as a function of the acceptance angle: (a) setup 2; (b) setup 3.

from these data, taking the square root of the values with the maximum angle; in fact, counting the times that a crossing muon is detected by both the upper and lower region of a layer, is a way of multiplying the single layer efficiency of the upper part for the lower one. The obtained values are presented in Tab. 4.1. All

layers show a satisfying value ranging from 92.5% to 98% except for layer 1 whose efficiency is 90% in setup 2 and 73.3% in setup 3. This last value is due to the multiplication of a good efficiency for the upper part (90% as for setup 2) and a bad one for the lower part (~60%); once finished the run and opened the detector, the PMT corresponding to 180° of layer 1 was found misplaced (the front face of the PMT did not touch the fiber edges).

	SETUP 2 single layer efficiency	SETUP 3 single layer efficiency
LAYER 1	90.3%	73.3%
LAYER 2	96.2%	95.5%
LAYER 3	98.0%	97.6%
LAYER 4	98.4%	92.5%
LAYER 5	$0^{\dagger}$	92.5%
LAYER 6	95.0%	93.0%

Table 4.1: Efficiency of the 6 layers. The poor value of layer 1 (setup 3) is due to a misplaced PMT. † = no PMT present.

Spatial resolution

The spatial resolution has been evaluated by means of the silicon detectors: the hits on the FAST layers, computed with the track reconstructed by the silicon xy planes, have been compared with the triangle positions. Two different setups (2 and 3 of Fig. 4.2) have been assembled. With the first one the results were not satisfactory because of several factors:

- The reference detector (silicon tracker) position was known only at a ~cm precision.
- No alignment between the fibers and the PMT anodes had been performed.
- The multiple scattering was not negligible. In fact there were several cm of plastic (2 cm of the trigger scintillators plus other ~2 cm of their PVC box) and of metals (the silicon tracker box itself, the tungsten on each tracker tray) between the reference detecting planes and the FAST tracker.
- The reference tracking detector was far from FAST (~30 cm above) and just on one side so that tracks could only be extrapolated while the best situation is to position FAST in between two tracking detectors (as in setup 3).

After the first cosmic run, that anyway allowed to verify the behaviour of the electronics and of the overall system and highlighted the real mechanical problems, the September 2006 data taking at AD took place. Since, as it will be explained in Sec. 4.2, no data for physics were collected, the second cosmic ray run goal was to solve the problems shown in the first one.
At the beginning of 2007, the FAST detector was opened and a coarse alignment verification was performed:

- One single channel was enlighted with a laser pointer at the edge opposite to the PMT and the PMT response was detected with an oscilloscope to match the fiber channel and the PMT one.
- The signal of the lighted channel was compared with the nearby ones and, changing the PMT position (within a few tenths of mm, that was the available range of the PMT support), the PMT was fixed minimizing the signal of the nearby pads with respect to the fiber matching anode.

A second cosmic ray data taking has been then performed with the last setup shown in Fig. 4.2 (setup 3). This configuration offered a better geometry than setup 2. In fact, the FAST tracker fibers were between the two reference silicon detectors, and the position of each beam chamber was known with a ~mm accuracy. After the PMT alignment the spatial resolution has been computed for this second cosmic ray run and the results are shown in Fig 4.15. In these plots the residuals between all the reconstructed triangles and the muon tracks, as computed by means of the silicon detectors, are shown. It is evident that, after the alignment the distributions are narrower (see the values in Tab. 4.2). As far as the z coordinate values are concerned, the gaussian fits have been performed considering only the central narrow peak because, as it will be explained in the following, this is the real residual distribution hidden among a lot of "noise" events (crosstalk, misalignment), since the plot contains all the triangles reconstructed in the event and not just one.

Having a reference detector and having obtained acceptable residuals, another question had to be answered: in the prototype analysis, where the crosstalk was negligible and the fibers were aligned one after the other on subsequent PMT anodes, the triangle with the smallest height was chosen as the good candidate to represent a hit. This (unique, since there is no other way to choose a triangle) possibility had to be verified and eventual systematic contributions had to be understood. For this reason, the residuals have been computed using not all the triangles but only the smallest ones, or the ones nearest to the muon hit. This kind of analysis can give a reliable value for the involved spatial resolutions because, even if the fibers are not correctly mapped, it is performed only when a track

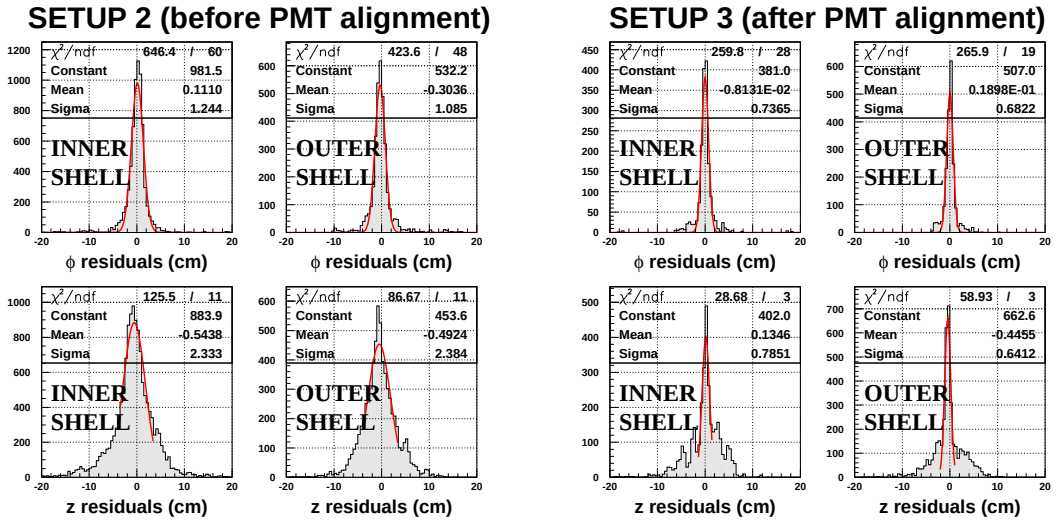

Figure 4.15: Comparison of the spatial resolution before and after the PMT alignment. The z coordinate values for setup 3 (b) and setup 2 (a) have been obtained fitting the central peak of the distribution.

	SETUP 2 (before alignment)	SETUP 3 (after alignment)
ϕ-INN	1.24 cm	0.74 cm
ϕ-OUT	1.08 cm	0.68 cm
z-INN	2.33 cm	0.79 cm
z-OUT	2.38 cm	0.64 cm

Table 4.2: Coarse spatial resolution (that is with all the triangles without any filter) obtained with setup 2 and setup 3 of Fig. 4.2.

is well reconstructed. In other words, it gives an idea of the potentiality of the detector if the mechanical problems were not there. The results are shown in Fig. 4.16 and summarized in Tab. 4.3. The two methods (the "best triangle" and the "nearest triangle") have similar results as far as the ϕ coordinate is concerned, thus confirming the reliability of the reconstruction algorithm. The z resolution on the other hand still suffers of the misalignment problems, so that the smallest triangle resolution is worse than the nearest one.

Summarizing, FAST is able to reconstruct the hits on its surfaces with a 1.8 mm and a 1.9 mm accuracy for the ϕ direction, respectively for the inner and outer

	best triangle	nearest triangle
ϕ-INN	1.8 mm	1.4 mm
ϕ-OUT	1.9 mm	1.7 mm
z-INN	3.6 mm	2.8 mm
z-OUT	4.0 mm	2.8 mm

Table 4.3: Spatial resolutions obtained with the best triangle method compared to the values corresponding to the nearest triangle.

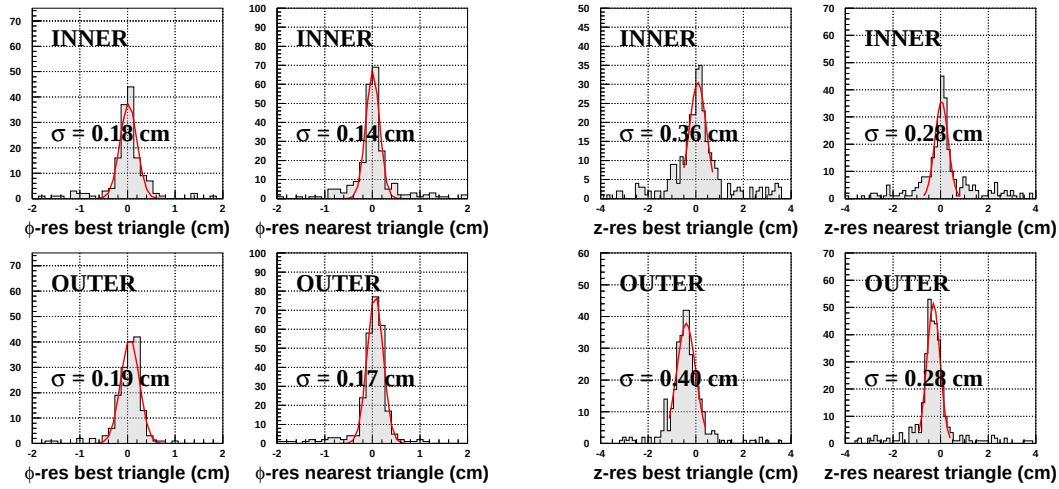

(a) ϕ spatial resolution

(b) z spatial resolution

Figure 4.16: Spatial resolutions computed by means of the "best triangle" method or the "nearest triangle" method (see the results in Tab. 4.3).

shell, and 3.6 mm and 4.0 mm for the z coordinate. The question is if these values allow to achieve the desired goals. The goal of the FAST tracker, as already said, is to reconstruct annihilation vertices with the tracks of the produced charged pions, and hits are assigned to a track using the time information. In other words, a vertex will be separated from another because the FAST tracker will distinguish the two corresponding annihilations in time. Being used in a cross section measurement experiment, the tracker will have the priority to count annihilations; thus these spatial resolution values, together with the efficiency ones, can be considered satisfying. The Geant simulation results that will be presented later on will confirm this idea.

Crosstalk

Considering the geometry of a channel (see the scheme in Fig. 3.33), when a particle crosses a layer it will hit one channel in 3/5 (60%) of the cases, while in 2/5 (40%) of the cases two channels will be hit; moreover, since two consecutive channels of the same layer are connected to the same PMT, one could expect that the same percentage can be found in the number of hit pads of a PMT. In other words, when a channel is hit, one could expect that on that PMT just one pad has a signal in 60% of the cases, while in the remaining 40% of the cases two pads are above threshold. This second number is an average value that takes into account the way fibers are grouped in a channel and the fact that particles do not cross layers orthogonally. The analysis has shown that this percentage is under-estimated. In Fig. 4.17 the number of hit pads per PMT is shown in two cases: before the PMT alignment (Fig. 4.17(a)) and after the PMT alignment (Fig. 4.17(b)). The highlighted percent-

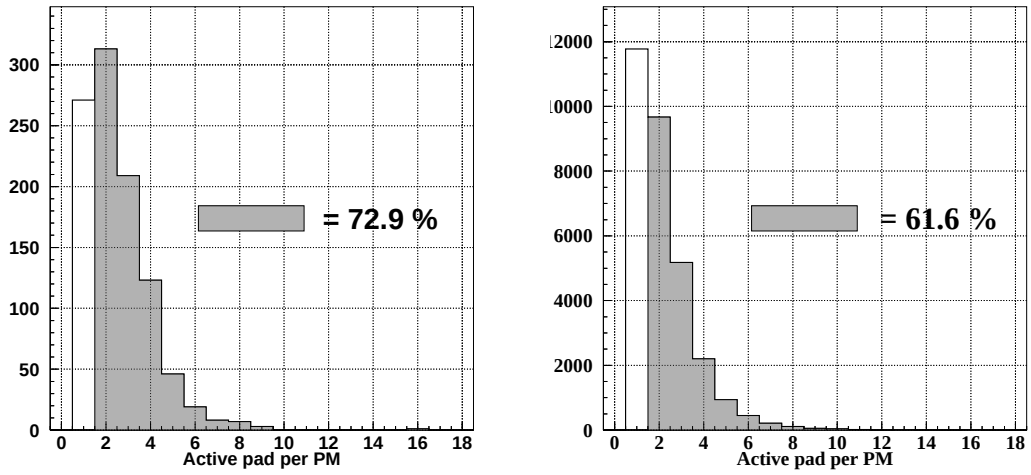

(a) before PMT alignment (b) after PMT alignment

Figure 4.17: Number of hit pads per PMT. The dark gray area indicates the percentage of the times that more than one single pad was hit in the runs before (a) and after (b) the PMT alignment.

age describes how many times more than one pad is hit. This number, after having subtracted a 40% for the geometrical considerations discussed above, is a coarse estimation of the optical cross talk for all the PMT pads. It can be noticed that the alignment has been really helpful in reducing this number (from ~33% to ~22%).

These values are consistent with the ~23% obtained with the prototype data in the previous Chapter.
To cross check this number, a "bad cluster" analysis has also been performed. The cluster has been defined as a set of hit nearby pads within the same event. This cluster is defined bad when two nearby pads do not correspond to nearby channels on the tracker. The average number of PMTs with a "bad cluster" on it has been computed on an event by event basis. The analysis has been performed after the PMT alignment and the obtained value is 2.55 PMTs. Since 12 PMTs are typically hit when a muon crosses all the layers, this value represents, dividing by 12, the probability of occurrence of crosstalk, thus 21% that is in agreement with the one obtained with the previous method.

4.1.4 The Geant simulation

The Geant simulation has been already introduced in the previous Chapter. While the FAST tracker geometry did not change, the experimental setups and the data taking conditions varied during the different phases (surrounding materials, type of particles, etc.). The simulation had to be tuned to cope with these changes.
In the following, the different goals and results of the simulation will be described comparing the obtained data with the experimental ones.

Cosmic rays

The cosmic ray setup 2 (see Fig. 4.2) has been reproduced. In this case, 1 GeV muons are generated at random positions (above the detector region) travelling downward with a random incident angle. Then, two filters, are applied: the first one has to do with the incoming angle that has to follow the $\cos^2\theta$ distribution; the second one is strictly geometrical since muons, in order to reproduce the experimental coincidence system, have to cross exactly the areas (in the zx plane) corresponding to the triggering scintillators (see Fig. 4.18(a)). In Fig. 4.18(b) one event is shown. These histograms, as well as the graphical event display, are useful tools to check all the simulation settings and to debug the software itself.
A first comparison between the experimental data and the simulated ones is shown in Fig. 4.19(b) in which the layer profiles, as those of Fig. 4.8(b), are presented together with the experimental ones (the 6 layer simulated data are shown in Fig. 4.19(a)). The main discrepancy between the two distributions is located in the last channels; it is evident, as already said, that there is no continuity between the left and right side of the plots even if these regions should correspond to adjacent

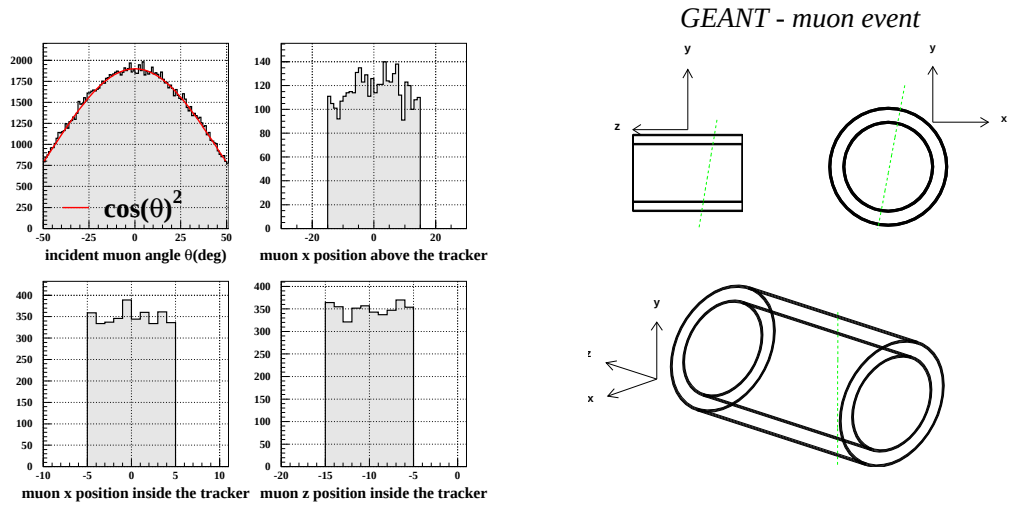

(a) (b)

Figure 4.18: Montecarlo simulation of the cosmic ray setup. (a) The incident angle θ of the muons depends on the cosmic rays distribution ($\cos^2\theta$) and the trigger system made of the scintillators placed above and inside the tracker. Some check histograms are plotted. (b) Example of an event: one muon crossing the tracker (line) as seen in the different projections.

sectors of the layers (top of the tracker). The most probable cause is again the wrong mapping. Moreover, there is the evidence of local misalignments of small groups of fibers (for example around channel 50 of layer 3). These problems have been already discussed in the previous sections; the simulation has provided another proof of these facts.

Triangle heights

As far as the particle hits on the layers are concerned, the fiber misalignments (the wrong mapping as well as the physical misplacements of groups of fibers) should not prevent the reconstruction of good triplets on the layers. In fact, even if some fibers (and the corresponding channels) were mapped in the wrong places, this should not vary the triangle heights distribution.
In Fig. 4.20 the best triangle height distributions are shown both for the cosmic ray data taking and the Geant simulation. The simulation values are 3 times narrower for the inner shell and 2 times for the outer one; as expected the misalignments do

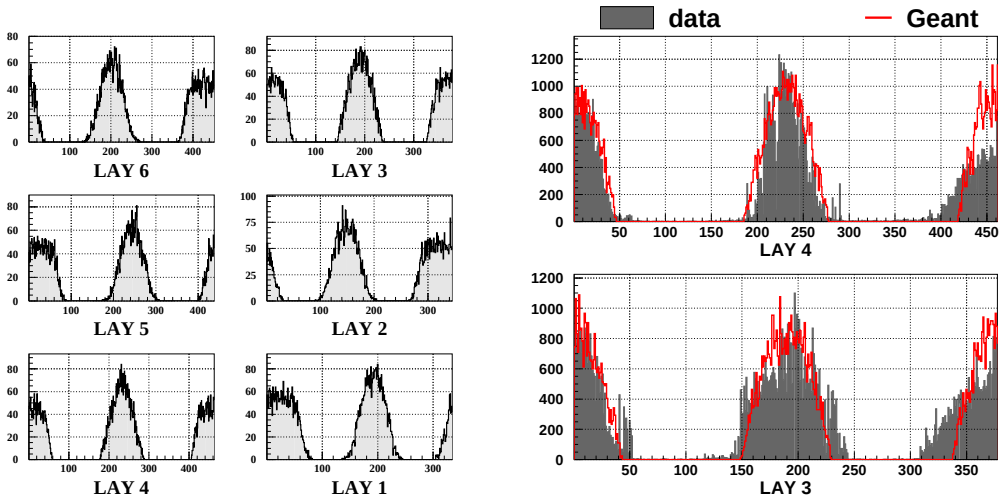

(a) (b)

Figure 4.19: Geant simulation of the cosmic ray data taking: (a) profile plots of the 6 layers; (b) detail of layer 3 and 4 superimposed to the experimental data.

not prevent a satisfactory reconstruction of the hits on the layers. The outer shell shows a better reconstruction capability than the inner one. Normalizing the two values to the corresponding circumferences (76.5 cm for the inner shell and 100 cm for the outer one) one obtains:

$$\sigma_{\text{exp}} = 0.57^\circ \quad \text{(INNER SHELL)}$$

$$\sigma_{\text{exp}} = 0.34^\circ \quad \text{(OUTER SHELL)}$$

This is in agreement with the hypothesis of a worse misalignment in the inner shell; as far as the crosstalk is concerned, it should give an equal contribution to both the shells, but it is reasonable to consider it a negligible effect in this case since, as already said in the previous Chapter, it does not prevent a right identification of the best triangle.
The obtained values will be used to compute the expected vertex reconstruction resolution by means of the simulation as will be explained in the next section.

Spatial resolution and vertex reconstruction

Two spatial resolutions have been considered:

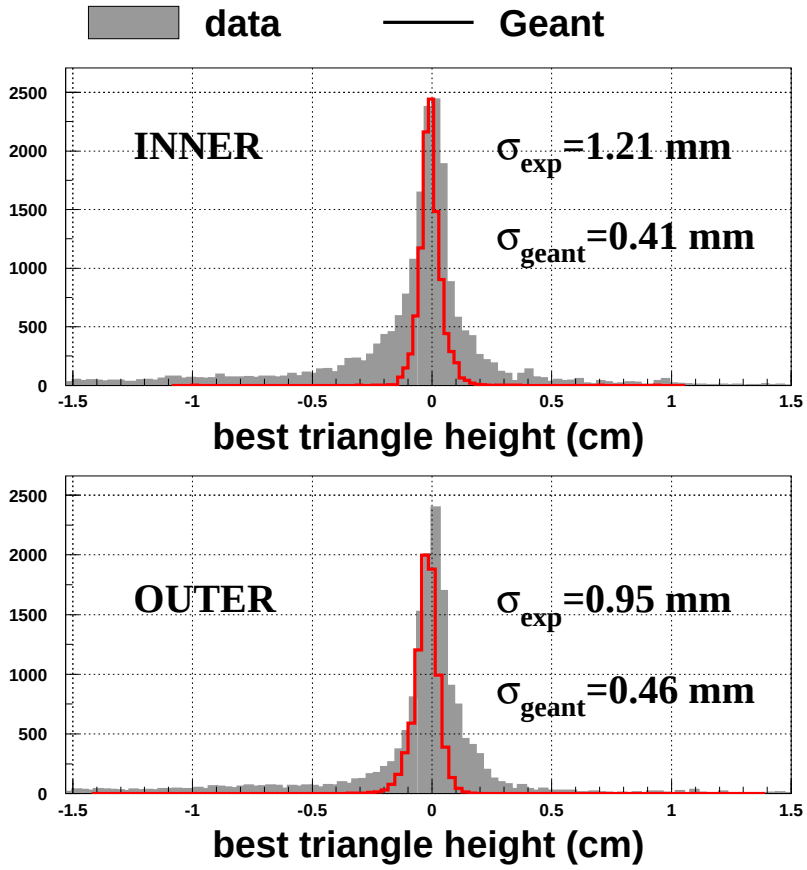

Figure 4.20: Best triangle height for the experimental data (filled histogram) and the Geant simulation (line). The inner shell values are shown in the upper plot and the outer ones in the lower plot.

- The ϕ and z resolution of the hit reconstruction
- The r and z resolution of the vertex reconstruction

The first one has been computed with the experimental data presented in the previous section (see Fig. 4.16), while for the second one this was not possible since no information about the real position of the vertex was available; thus, in the second case, the expected values have been computed with the help of the simulation with a method that will be described in the following.
The goal was to estimate how the reconstruction of the hits on the layers would affect the reconstruction of the vertex position inside the sensitive volume. In the

simulation the FAST tracker hosts an aluminum pipe with a 20 cm diameter (target vessel) containing hydrogen; in order to generate (charged) pions isotropically, antiprotons are placed within the filling gas, at rest. This is a configuration that approximately reproduces the AD data taking setup. It should be remarked that the filling gas is hydrogen, thus a pure $\bar{p}p$ annihilation occurs everytime a $\bar{p}$ is generated. Hydrogen has been one of the target gases for the 2006 run and, moreover, in literature the best known annihilation cross sections are referred to this gas (see in Sec. 3.3.2 the pion multiplicity comparison between the simulation values and the experimental ones).
In Fig. 4.21 an event is shown. In this case an antiproton has been generated at the center of the gas target and the annihilation products are four charged pions and two neutral ones (which decay in 2 photons each). Summarizing, the following

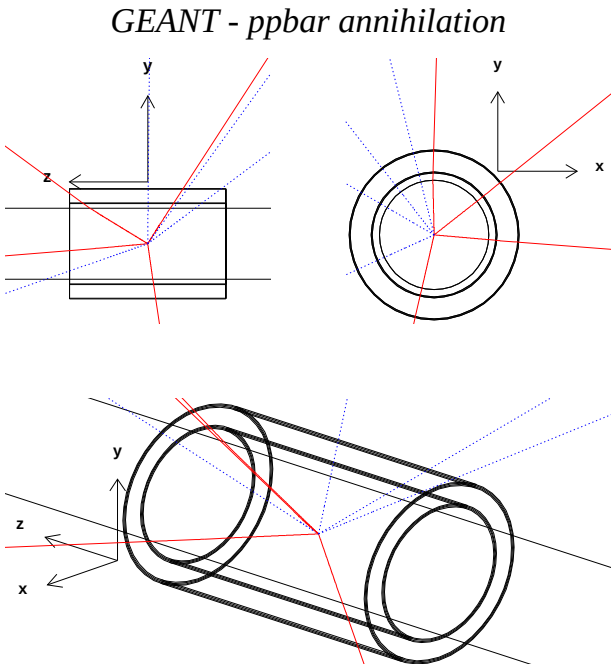

Figure 4.21: Geant $\bar{p}p$ annihilation. The produced particles in the event are 4 charged pions (π^+ or π^-), drawn with a solid red line, and 2 π^0s, which immediately (the mean life is $8.4{\cdot}10^{-17}$ s [41]) decay in two photons each (dotted blue line).

procedure has been applied to compute the vertex reconstruction resolution:

- The antiprotons are generated at rest in the desired position inside the target vessel. Their annihilation with the protons of the hydrogen nuclei is instantaneous. This occurs even if the gas is at low pressure. Therefore, the starting position of the antiprotons coincides with that of the annihilation, whose coordinates have to be stored.

- As far as the annihilation products are concerned, it should be noticed that in most of the events (~93%) charged pions are present. Their distribution (pion multiplicity) has already been discussed in the previous Chapter (see Fig. 3.38). In Tab. 4.4 the probabilities for different charged pion states are shown. The charged pions cross the scintillating fibers[5] and the correspond-

$\pi^{\pm}$s from $\bar{p}p$ annihilation	probability
0	8.0%
2	44.4%
4	45.3%
6	2.1%

Table 4.4: Charged pion multiplicity distribution in $\bar{p}p$ annihilations obtained with the Geant simulation. Only even numbers are allowed due to the charge conservation principle.

ing hit coordinates are stored. As far as the radial distance from the center is concerned, the hit has been placed at the average radius of layer 2 (for the inner shell) and layer 5 (for the outer shell). Only the events with two charged pions that crossed all 6 layers have been selected. This allowed to simplify a lot the vertex reconstruction algorithm.

- At this point, the prototype results have been used as well as those from the cosmic ray data taking. In the first case it has been obtained a ϕ resolution of σ_ϕ=570 μm and a z one of σ_z=1.6 mm (they correspond to the σ_x and σ_y values in Fig. 3.31), while in the second case σ_ϕ=1.8 mm and σ_z=3.6 mm for the inner shell and σ_ϕ=1.9 mm and σ_z=4.0 mm for the outer one (Fig. 4.16). These results are summarized in Tab. 4.5 and have been used to spread the single hits found with the simulation. In other words, once found the hit, a gaussian distribution with the measured hit resolution sigma has been generated centered in the hit and the hit has been chosen in this gaussian.

[5]It has been calculated, through the simulation, that only in 1.6% of the cases a charged pion decays in the corresponding muon and neutrino before it has crossed all the layers. Therefore this small fraction of events has been neglected.

	Prototype	Cosmic ray run
Spread values		
ϕ-spread	0.57 mm	1.8 mm (inner shell), 1.9 mm (outer shell)
z-spread	1.60 mm	3.6 mm (inner shell), 4.0 mm (outer shell)
Obtained vertex resolution		
r	**4.8 mm**	**12.6 mm**
z	**7.7 mm**	**17.6 mm**

Table 4.5: Vertex reconstruction resolution computed with the Geant simulation. The hits on the layers have been spread according to the ϕ and z resolutions obtained with the prototype tests and with the cosmic ray data taking.

- The resulting points have been connected by a line thus obtaining a sort of track.
- If no spread was applied, the two tracks would obviously have an intersection point in correspondence of the annihilation position where the two pions have been generated. But, since this is not the case, the two lines are skew, that means that they do not have any intersection point. Anyway a vertex can be reconstructed computing the minimum distance between the lines and placing the vertex at half this distance.
- The values found with this method were subtracted from the real vertex position to obtain a residual distribution.

In Fig. 4.22 the results of the procedure described above are shown. The x and y reconstructed vertex residuals present a similar value; the r resolution has been defined as the average of the x and the y one:

$$\sigma_r = 4.8 \text{ mm} \quad \text{(prototype data)}$$

$$\sigma_r = 12.6 \text{ mm} \quad \text{(cosmic ray run)}$$

It is difficult to give an estimation of the error on this value since the fit has been performed considering the central region, where the main peak is visible, but not the tails.
As far as the z coordinate is concerned, the obtained values are

$$\sigma_z = 7.7 \text{ mm} \quad \text{(prototype data)}$$

$$\sigma_z = 17.6 \text{ mm} \quad \text{(cosmic ray run)}$$

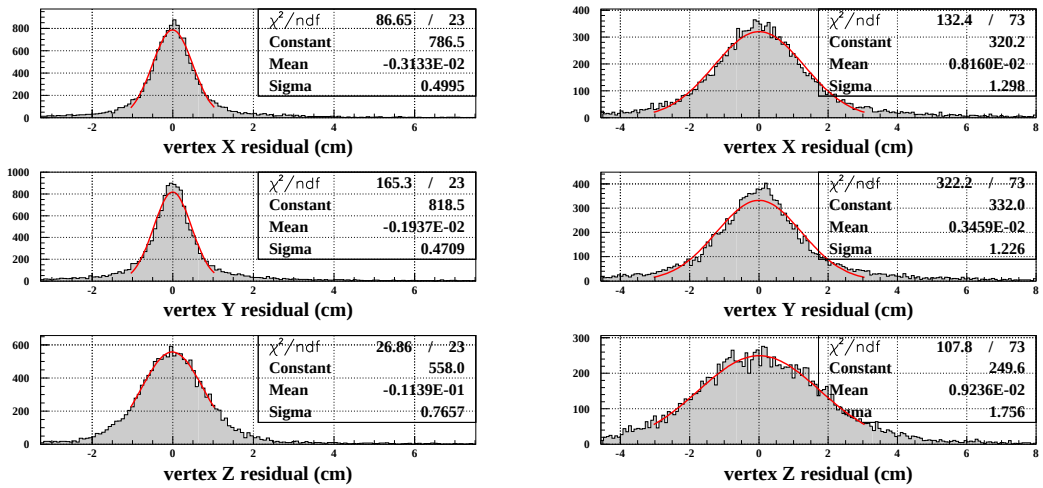

(a) Prototype data (b) Cosmic data taking

Figure 4.22: Expected reconstructed vertex residuals estimation by means of the Geant simulation. The distributions refer to a run in which 50000 antiprotons were generated at the center of the target vessel.

The values obtained for FAST are worse than what had been foreseen after the prototype test. These data confirm that something went wrong with the detector assembly and that the alignment corrections described in Sec. 4.1.3 are not enough to solve it.
The same simulation runs provide another information: on an event by event basis, if the number of pions that cross both the inner shell and the outer one is at least two, in principle this is enough to reconstruct a vertex. Thus the number of events with this feature, divided by the total number of events, gives a sort of *reconstruction efficiency*. For antiprotons generated at the target vessel center and, as far as the z coordinate is concerned, at the center of the sensitive volume of the FAST tracker, the obtained value is

$$\epsilon_{rec} = 80.2\%$$

This is in complete agreement with the theoretical value that can be computed in this way: given the charged pion multiplicity distribution obtained in the simulation (see Tab. 4.4) and given the geometrical efficiency at that z value (see in the previous Chapter Fig. 3.40(b); for z=0 cm the geometrical efficiency is 85%), the

reconstruction efficiency can be computed by means of the binomial distribution[6] obtaining:

$$\epsilon_{rec} = 80.15\% \qquad \text{(THEOR.)}$$

After having computed these quantities relative to antiprotons generated at the target vessel center (x=y=z=0), other starting positions have been tried in order to characterize the tracker behaviour as a function of the annihilation position. This is important as far as the gaseous targets are concerned. In fact, as it will be explained in the next section, the annihilation can occur along the whole vessel length, thus it is relevant to know how the resolution efficiency is affected by this.
Scans along both the z axis (Fig. 4.23) and the r coordinate (Fig. 4.24) have been performed independently. In both cases the 2D histograms (see plots on the right of Fig. 4.23 and 4.24) have been sliced and the resulting distributions fitted with a gaussian function in order to obtain the resolution at that position. In principle, at z=0 and r=0, the computed values of the spatial resolution should be the same as those already presented in Fig. 4.22, that is σ_r = 4.9 mm and σ_z = 7.7 mm. But this is not the case; in fact, looking at z=0 for the z scan (or r=0 for the r scan), larger values are obtained. This is due to the fact that the gaussian fits are not limited to the narrower bulk of the residual distribution as was for those in Fig. 4.22.

Anyway in the following the values obtained from Fig 4.22 will be considered the vertex reconstruction resolutions.
In the z scan no significant change can be noticed. This is reasonable since changing the z coordinate of the antiprotons position (and not the x or y one) does not modify the distance of the annihilation from the layers. On the contrary, as it has been already shown in the previous Chapter, the geometrical efficiency varies a lot going from z=0 to the edge of the sensitive region (the values decreases to ~45% at z=±25 cm).
The r scan presents an unexpected trend. In fact both the z and r resolutions show an improvement when the antiprotons are generated closer to the layers. Going from the center to the border at 10 cm there is, for both z and r values, an improvement of ~10%. The possible reason could be that the pions are produced closer to the layers, thus the lines that are back-traced towards the vertex position have a smaller lever arm and the vertex is reconstructed with a better accuracy. One could observe that pions are generated isotropically so no such effect could be present. But it has to be remarked that, while at r=0 the geometrical efficiency is

[6] The probability of getting exactly k hits from n trials of an event that has an occurring probability p is the so called probability mass function $f(k;n,p) = \binom{n}{k} p^k (1-p)^{n-k}$. Thus the probability that at least 2 pions reach the outer layers is given by $1 - \sum_{n=0}^{6} w_n f(1;n,p)$ where w_n is the probability of having n starting pions (see Tab. 4.4) and p is 85% (see Eq. 3.3).

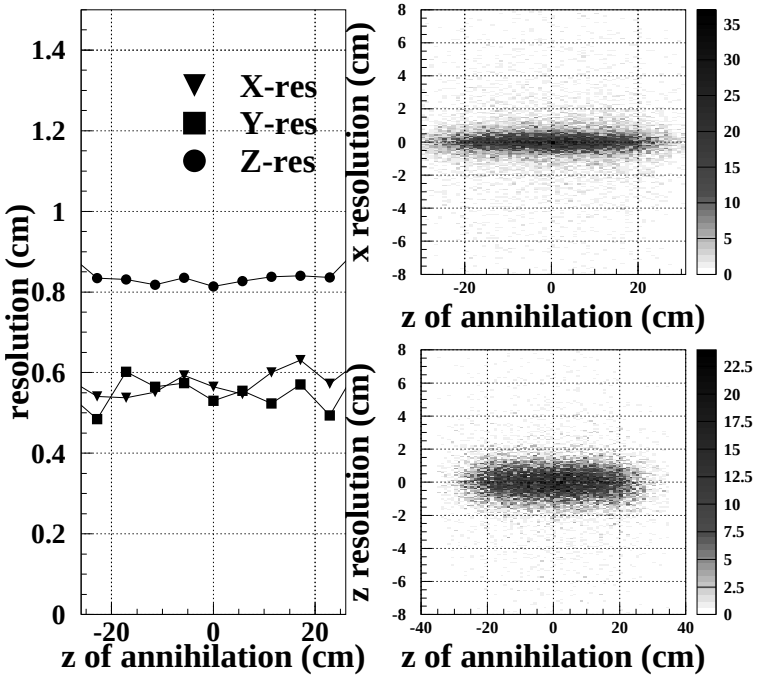

Figure 4.23: Spatial resolution as a function of the annihilation position (z scan). Left: resolution values (sigma of the gaussian fits). Right: bidimensional distribution of the x and the z resolution.

isotropic too, for larger values of the r coordinate the probability of detecting the pion is higher if its direction is towards the nearest layers. In other words, if a pion is generated at a large r, for example near the top of the target vessel (while z is fixed at 0 cm), the solid angle offered by the scintillating fiber layers is larger in the upward direction with respect to the downward one. This fact probably causes the improvement of the spatial resolution with the increasing r of the vertex.

4.2 September 2006 data taking

The first data taking period started in September 2006 and lasted 10 days.
After the installation of all the experiment parts and a few pre-run tests, the problem of the beam characteristics became evident. As already anticipated, this occupied almost all the available shifts and no data useful for physics were collected.

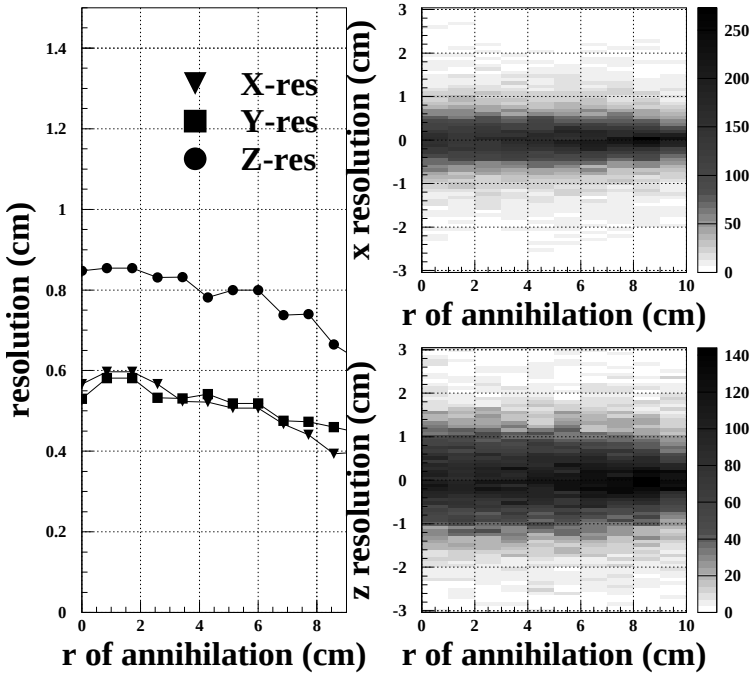

Figure 4.24: Spatial resolution as a function of the annihilation distance from the z axis (beam axis). Left: resolution values (sigma of the gaussian fits). Right: bidimensional distribution of the x and the z resolutions.

4.2.1 Experimental setup

The experimental layout of the data taking is shown in Fig. 4.25. The tracker, in this case, hosted a 213 cm aluminum vessel (diameter 21 cm, width 1 cm) which had the function of containing the chosen target gas. The beam pipe was closed by a 70 μm Kapton window[7]. The incoming 100 MeV/c antiprotons, once out of the beam pipe, had to pass through ~10 cm of air and then enter the vessel crossing a 50 μm mylar window[8]. In the gas region, antiprotons normally do not interact until they reach the end of the aluminum vessel (2 cm thick) where the bunch particles completely annihilate. A small fraction of them (depending on the density of the target or, in other words, on its pressure) undergoes an in-flight annihilation which, in principle, should be detected by the FAST tracker.

[7]Kapton® polymide film [74].
[8]Mylar® polyester film [74].

As far as the electronics readout is concerned (see the scheme in Fig. 3.5), the frontend boards have been mounted on a support close to the PMT side of the tracker; the repeater boards were arranged in a tower on the tracker box, while the remaining data acquisition elements were aside the tracker on a rack (Fig. 4.26(a)). Different gases (molecular ^{2}H and ^{2}D, ^{4}He, Ne, Xe) were available and the switch from one of them to another was possible in 60–90 minutes through a set of valves and pumps assembled in a compact gas control unit on a dedicated rack (Fig. 4.26(b)).
The whole system assembly in the ASACUSA area at AD lasted 2 days and is shown in Fig. 4.27.

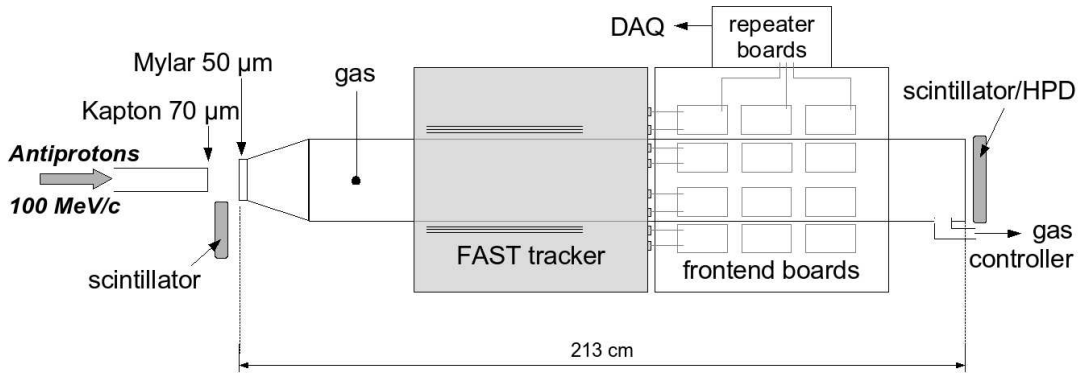

Figure 4.25: Experimental setup of the September 2006 data taking at AD.

The HPDs

Together with the already presented scintillators (see Chapt. 3), another kind of detector has been used to have one more timing reference: even if the name HPD (Hybrid Photo Diode) strictly refers to the photodetector alone, it is common to indicate the scintillator whose light is read by a silicon photodetector. The ones employed during the data taking had already been successfully used to evaluate the antiproton multiplicity during the ATHENA experiment [75].
The detector consists in a 20×10 cm^2 scintillator readout by the HPD. It is a high dynamic range photodetector made of a photocathode at one side (hosted in an aluminum vacuum box) kept at a negative high voltage (a few thousands of Volts) and a silicon photodiode at the opposite side working as an anode plane. The photons generated in the scintillator strike the cathode producing electron-hole pairs. The high potential accelerates them towards the silicon plane that, being

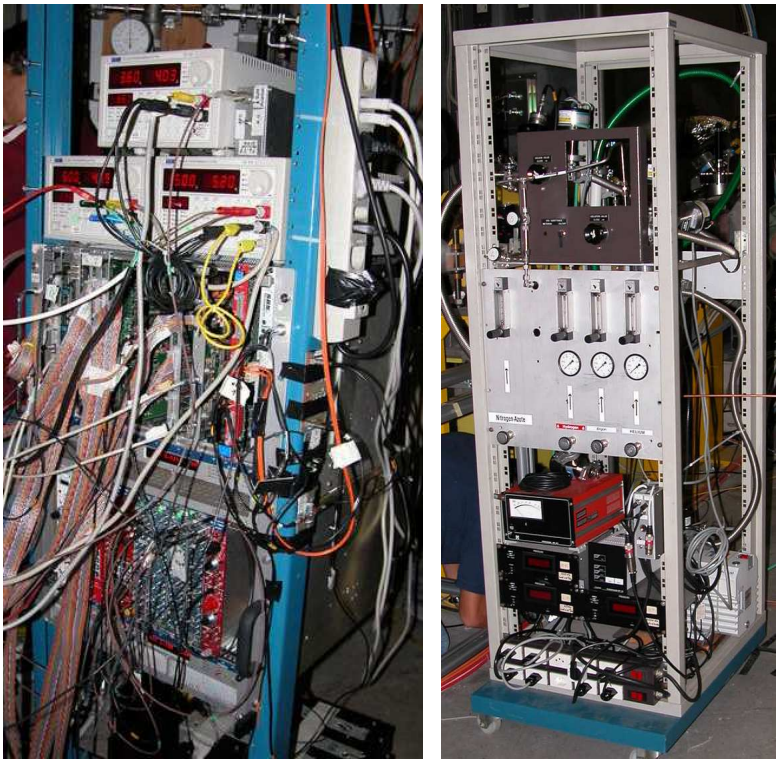

(a) (b)

Figure 4.26: (a) Electronics rack. (b) Gas control panels.

biased at a few Volts, collects the produced electrons generating the output signal. The scintillator is connected to the HPD with a lucite light guide.
During the data taking the HPD, as well as the other scintillators, have been placed in different positions especially to monitor the time characteristics of the beam (see Fig. 4.28). In particular, the HPD has been placed just behind the endcap of the target vessel in order to monitor the arrival time of the beam detecting the charged pions generated in the annihilations in the 2 cm of aluminum.

Expected number of events

The number of in-flight annihilations is determined by the annihilation cross section itself, that is the investigated quantity. Therefore the number f of expected in-flight annihilations per incoming particle can be only roughly estimated consid-

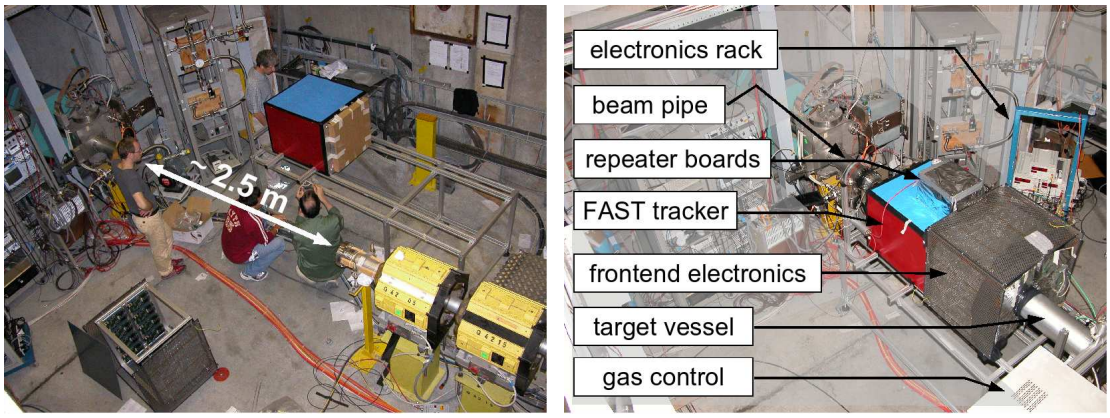

(a) (b)

Figure 4.27: ASACUSA experimental area at AD. (a) Before the installation completion. (b) After having completed the assembly.

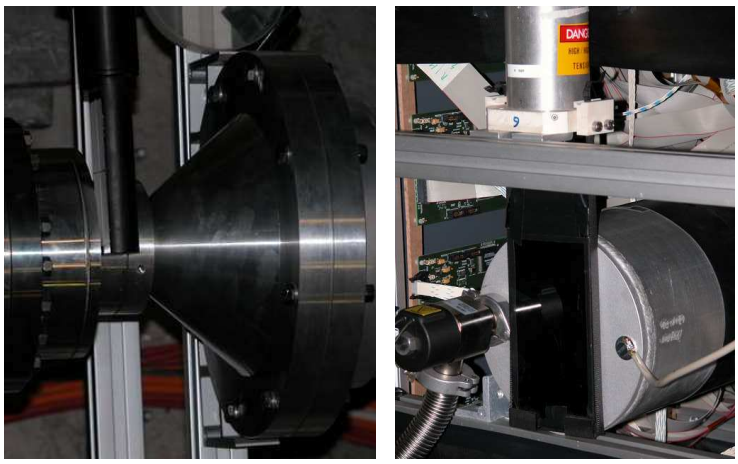

(a) (b)

Figure 4.28: Positioning of the time reference detectors during the data taking. (a) The 3×10 cm^2 (1 cm thick) scintillator placed close to the entrance window of the target vessel. (b) The HPD scintillator next to the vessel endcap.

ering the formula:

$$f = \sigma_{ann} \cdot D \cdot L$$

where σ_{ann} is the total annihilation cross section, D is the number of targets per unit volume and L the length of the whole target (200 cm). As far as D is concerned, at

room temperature and pressure (~18° C, 1 atm), 1 mole of gas occupies a volume of ~24 liters. As an example, using the ideal gas law PV=nRT where P is the pressure (1 atm $\simeq 10^5$ Pa), n is the number of moles, T is the absolute temperature and R the gas constant (R=8.314 $m^3 \cdot Pa \cdot K^{-1} \cdot mol^{-1}$), and given that 1 mole contains $N_A \simeq 6 \cdot 10^{23}$ (Avogadro's number) molecules, one can compute for molecular hydrogen at 1 mbar pressure:

$$D \simeq 2 \cdot 6 \cdot 10^{23} / 24 \cdot 10^6 = 5 \cdot 10^{16} \text{ protons/cm}^3$$

As far as the annihilation cross section is concerned, a suitable value (at the order of magnitude level) is 1 barn (10^{-24} cm^2) (see Chapt. 1). Substituting, one obtains:

$$f \simeq 10^{-4}$$

This fraction is even smaller considering the geometrical acceptance of the FAST tracker (at a good approximation, 1/4 of the vessel length, that is 50 cm, contributes to the number of detectable events).
Thus if a single bunch contains 10^5 antiprotons, the expected number of in-flight annihilations is ~2–5.
The electronics readout, the data acquisition software and the tracker itself had been thought to cope with this number of events per bunch.

Vertex reconstruction

Once the acquisition software provided the raw data, the offline analysis was organized in two steps:

- A first program (written in Fortran) allows the selection of the interesting events. An example of its graphic interface is shown in Fig. 4.29. Starting from the raw data, the program organizes the hits on the channels on the basis of their time of arrival (within the 800 ns gate) and, if necessary, these time profile histograms can be shown to the user; in this case, one can select a specific time window (as shown in Fig. 4.29) and activate another graphic tool that shows the corresponding hit channels on the cylinder surfaces (Fig. 4.29 on the left). When the analysis ends, a new ntuple is created with a minimal set of data (hit channels and corresponding time) and passed to the second program. This procedure can be run both manually (with the help of the graphic display to select, event by event, different time windows) or automatically, that should be the normal working mode. In other words, the graphic interface with the manual selection can be run as a preliminary evaluation to tune the region of

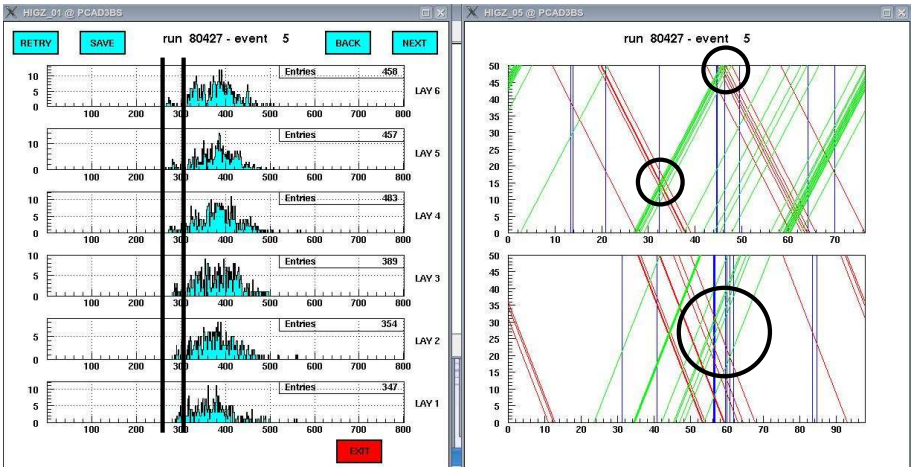

Figure 4.29: Offline event analysis graphic interface. The time interval to consider is manually selected on the left (lines); after this selection the corresponding hit channels are drawn on the opened cylinder surfaces on the right window where the possible hits (here highlighted with circles) are easier to identify.

interest; then the software is ready to be run automatically, becoming faster and coping with the entire data set.

- A second program (written in Root[9]) uses the previously created ntuples to reconstruct the vertices, also with the help of a 3D viewer (Fig. 4.30). Given the hits on the channels, the program reconstructs doublets and triplets and identifies a point in space. Connecting all these points, lines are drawn among which the charged pions ones have to be discriminated with dedicated algorithms. Without entering into details, it can be said that different levels of confidence can be selected: for example, if the statistics is high, a possible criterion is to consider only those lines formed with a triplet chosen with a suitable threshold (on the height of the triangle itself); on the other side, if only a few channels per event are hit for a certain run, the selection can be less stringent including those lines obtained with the connection of the doublets too.

[9]http://root.cern.ch/

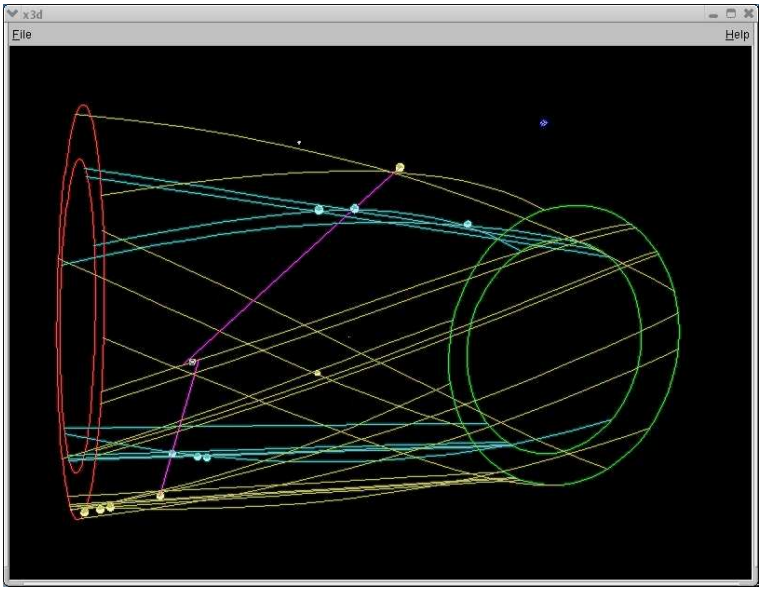

Figure 4.30: 3D viewer of the vertex reconstruction software. The perspective can be easily changed in order to evaluate the quality of the event.

4.2.2 The Geant simulation

The 2006 data taking setup has been reproduced with the Geant simulation. The aluminum vessel, the target gases, the flanges, the mylar entrance window as well as the vacuum pipe with the Kapton film have been added to the already built geometry. In Fig. 4.31 an event is presented: a single antiproton enters the gas region and reaches the endcap annihilating on it. Since the annihilation occurs on an aluminum nucleus, it can be on a proton as well as a neutron allowing the production of any number (even and odd) of charged pions. This simulation cannot provide information about in-flight annihilations since the probability of occurrence of such events is so small that the number of starting antiprotons would be too large. Moreover, the in-flight annihilation rate, being strictly connected to the annihilation cross section, is the investigated physical quantity of the experiment. Therefore, in this case, the simulation was used only for evaluating the possible solutions to the beam problem as far as the tracker is concerned as it will be explained in the next section. In fact, the beam problem was not completely understood (until the 2007 data taking) nor solved; thus, at the beginning of the data taking, a lot of trials to shield some parts of the tracker to avoid its saturation have been done and the simulation was used to choose suitable thicknesses of the

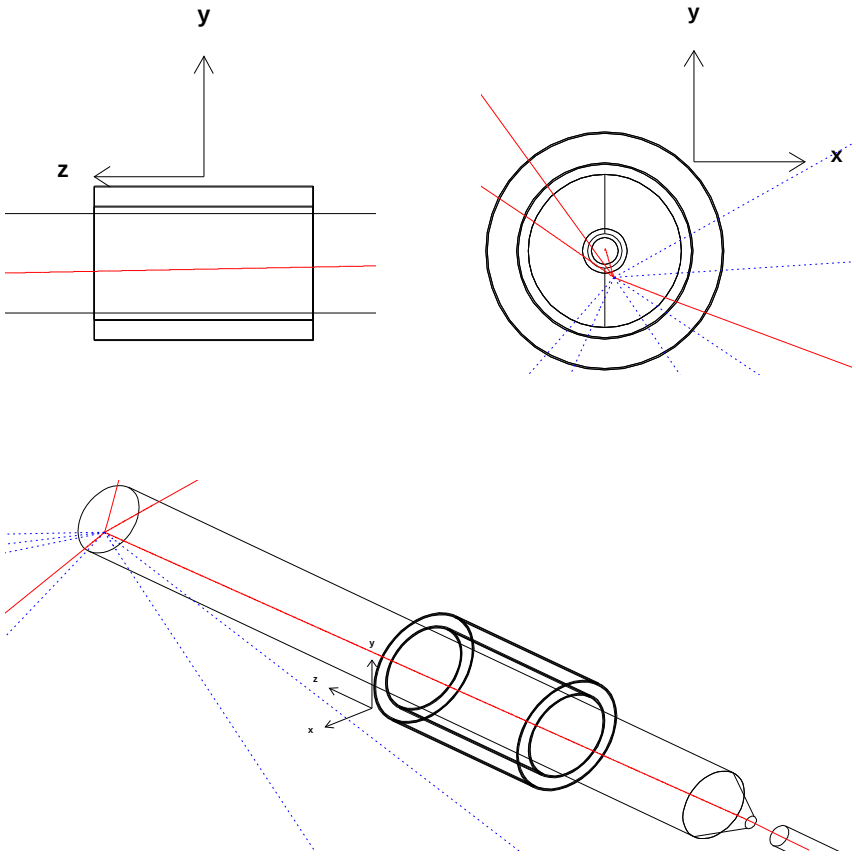

Figure 4.31: Geant simulation of the 2006 data taking setup. The antiprotons come from the beam pipe, cross the Kapton and mylar windows (as well as the air between them) and enter the gas region. In this example, that is the most probable event, nothing happens until the antiproton reaches the aluminum of the endcap where it annihilates producing 3 charged pions (solid lines) and 3 neutral ones (the dotted lines are the 6 photons coming out from the π^0 decays).

shielding material (lead).

4.2.3 The beam problem

The expected beam characteristics, as presented in Chapt. 1, consisted in a 6-bunch structure with ~2 s between each one, in which each bunch had a time width of 20–50 ns. As far as the 6-bunch structure is concerned, 6 extractions were correctly performed by the machine and, even if there was an instability in the 6-bunches intensity, this was always maintained.
When the first data were collected the situation was the one shown in Fig. 4.32 where the time of arrival of the signals on the hit channels is plotted. Unfortunately

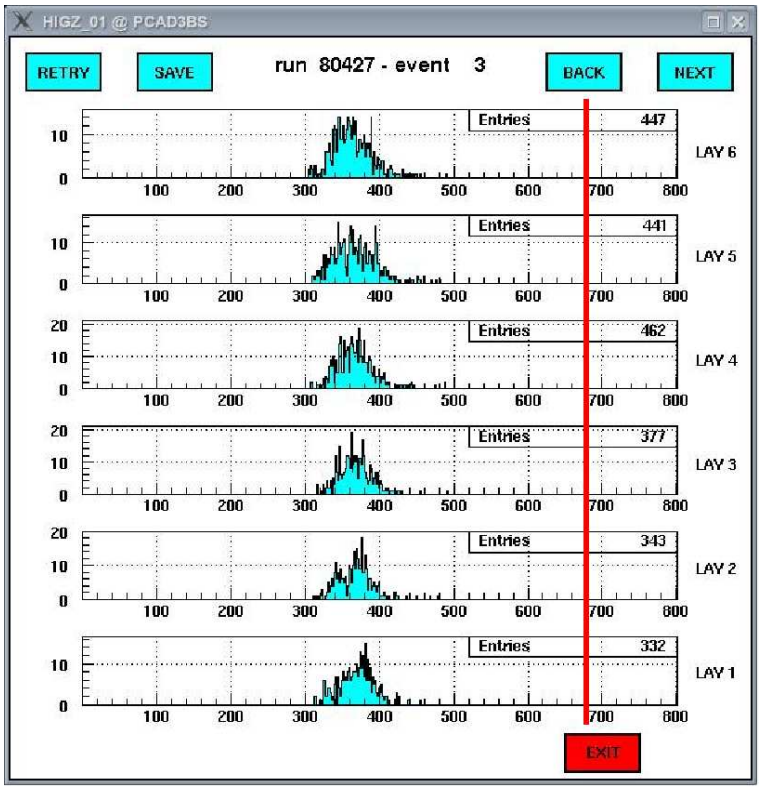

Figure 4.32: Time profile of the hit channels of the FAST tracker during the 2006 data taking. The line marks the expected time of arrival of the bunch on the endcap of the target vessel.

this was a completely unexpected situation. The channel signals started too early with respect to the expected time of arrival of the antiprotons on the endcap of the vessel. The problem, now solved, required a lot of time consuming tests to understand its cause and to try to solve it.

The first investigated field was the trigger system. As already explained in Sec. 3.1.5, the acquisition electronics is triggered by AD itself at some point of the ASACUSA line extraction. The trigger signal has to be sent to the electronics taking into account the antiprotons time of flight (at 100 MeV/c of momentum they travel at ~3 cm/ns, that is 1/10 c) and the delay due to the cable lengths. The most probable cause of errors was the second one (the machine trigger signal was brought from the counting room to the experimental area by means of ~15 m long cables). This aspect was checked and it was found that the machine trigger jittered, for the first bunch, of at least ~10 ns. This could be a problem, but, at the same time, could not justify the ~250–300 ns earlier arrival of antiprotons.
Thus the conclusion was that the bunch time shape was not the expected one. A not negligible fraction of the antiprotons arrived a few hundreds ns before the main bunch. These early antiprotons (in the following they will be referred to as "pre-bunch") annihilated on the endcap of the vessel just as the main bunch was crossing the fiducial region of the FAST tracker, preventing any in-flight annihilation to be detected. In fact, as explained in Sec. 3.1.5, the recovery time of each channel is ~100 ns, thus the whole tracker can be blinded by a few thousands of annihilations on the endcap of the vessel.
The existence of the pre-bunch was definitely proved in the 2007 data taking.

4.3 July 2007 data taking

In July 2007 another run was planned. Considering the pre-bunch problem described in the previous section, the first goal was to solve it. After a few investigations and thanks also to the help of the AD operators, the problem was finally solved. The run lasted 10 days and a lot of data useful for physics have been collected with different targets. The analysis is still ongoing; for this reason only a brief description of the setup will be presented.

4.3.1 Experimental setup

The main change from the 2007 setup was the solid targets instead of the gaseous ones. In Fig. 4.33 a scheme of the experiment is shown (see also a photo in Fig. 4.34). The beam pipe is directly connected to the target vessel through vacuum valves and a turbo pump. The FAST tracker hosts a 14 cm diameter aluminum (2 mm thick) tube which is connected to another steel tube with a diameter of 30 cm.
The turbo pump allowed a fast emptying (~5 hours) of the vessel tubes after the target replacement: due to the limited available space and to the mechanics of the

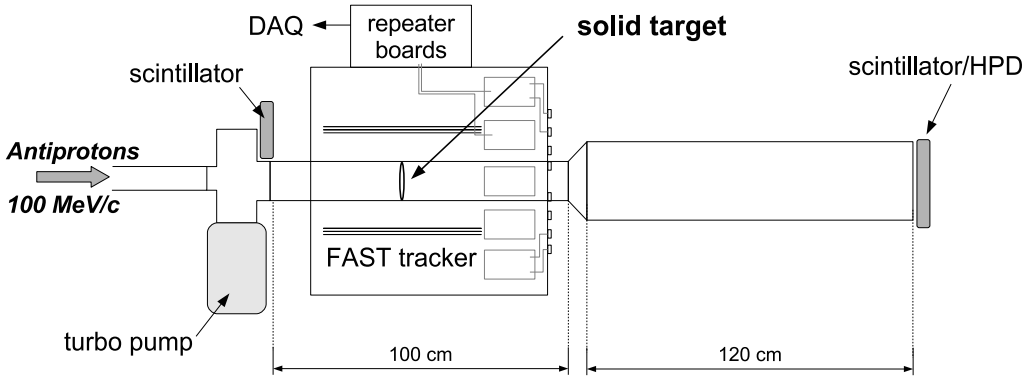

Figure 4.33: Experimental setup of the 2007 data taking at AD.

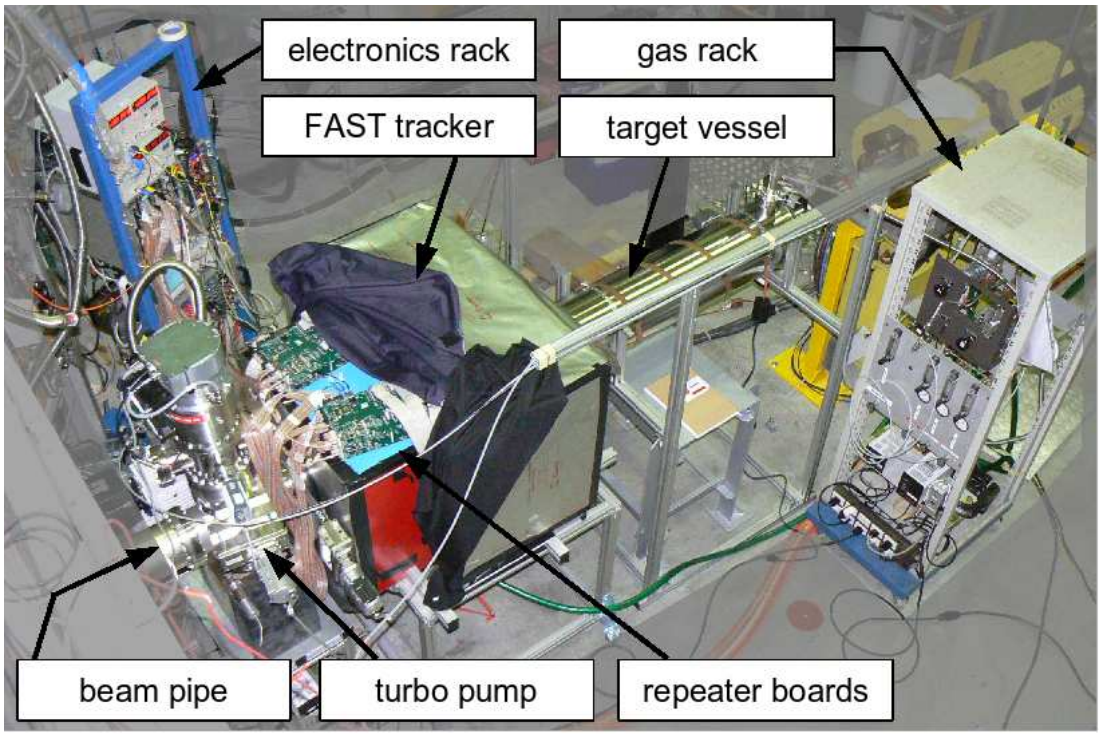

Figure 4.34: Photo of the 2007 data taking setup.

system, the whole operation lasted ~2 hours. Anyway these operations (target replacement and emptying down to a few 10^{-13} bar vacuum) could be easily performed in the 12 hours available between the assigned shifts.
The solid targets consisted in a set of thin disks of Mylar (0.9 μm) with a deposit of different metals: Sn (412 nm), Ni (267 nm) and Pt (169 nm). These correspond to different regions of interest as far as the atomic mass number A is concerned; thus 5 "targets" were available: empty target, the Mylar support alone and the same Mylar plus one of the cited materials. The target support is shown in Fig. 4.35(a) while in Fig. 4.35(b) the target during the replacement is presented.
The replacement of the targets was performed closing the vacuum valves, restoring

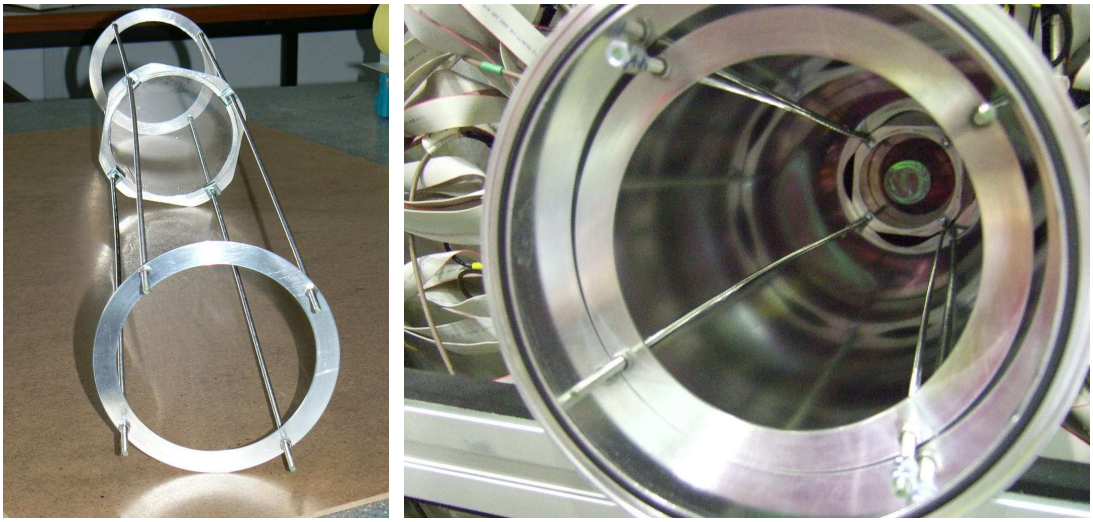

(a) (b)

Figure 4.35: Target of the 2007 data taking. (a) Aluminum support with only the Mylar disk. (b) The target inside the 14 cm diameter tube hosted by the FAST tracker.

the room pressure in the vessels by means of nitrogen filling (to avoid contaminations, for this purpose the same gas control unit of the previous data taking has been used), taking the tubes out of the tracker as well as the target support, substituting the target disk; all the operations were then performed the other way round to have FAST ready to run.
The frontend electronics (the frontend boards and the repeater boards too), due to the limited available space, have been placed directly on the tracker box close to the PMT side of it.

With this setup, differently from the last year one, the antiprotons do not cross any material until the thin target disk placed at the tracker center (or other positions in the z coordinate). Here some annihilations could occur, while the main part of the bunch goes straight to the endcap of the larger vessel. All the targets widths have been studied to obtain ~20–40 annihilations for every 10^4 incoming antiprotons. Since ~3 charged pions are produced for each annihilation, this number could be too large; but it must be taken into account that the detector geometrical efficiency makes it lower and also the fact that in this case annihilations, in principle, are well localized at the target position, thus making the reconstruction algorithms simpler.

4.3.2 The solution of the pre-bunch puzzle

When the first bunches were spilled for the ASACUSA experiment the situation was the same as the previous year: the pre-bunch was still present striking the vessel endcap a few hundreds ns before the expected arrival time. A deep investigation of the pre-bunch nature was done. In fact, two were the reliable hypotheses:

- the first one was that the early signals on the tracker were due to charged pions coming from the bending magnets placed ~10 m upstream. When the beam was steered to the ASACUSA beam line the tails of the beam could have annihilated on the beam pipe and the generated pions (moving at $\sim c$, that is 30 cm/ns) could reach the tracker instantaneously while the main beam (travelling at 3 cm/ns), arrived at the fiducial region ~300 ns later;

- the second hypothesis was the existence of a physical antiproton pre-bunch, in the sense that the early hits on the tracker were due to early antiprotons arriving at the vessel endcap.

The two hypotheses were investigated also by means of the scintillator detectors already described. A lot of trials were done and finally the second hypothesis was proved. A significant plot is presented in Fig. 4.36(a). The 3×10 cm^2 scintillator (sensible to the single charged particle) has been placed at the tracker entrance (close to the turbo pump), while the HPD (low sensitivity) has been placed at the vessel endcap in order to detect the arrival of the main bunch. It can be seen that the scintillator signal saturates a few hundreds ns before the main bunch generates the signal in the HPD.
Unfortunately the diagnostic devices of the AD ring are not designed to detect these low intensities and, moreover, all the AD experiment acquisitions are studied to detect a few secondary particles after the main bunch has annihilated, being not sensible to a low intensity pre-bunch. Therefore the discovery of these early

antiprotons was an unwanted surprise.
The only possibility to solve the problem was to change the timing of the extraction system, as it has been done, removing completely the pre-bunch. In Fig. 4.36(b) the signals of the scintillator and of the HPD (in the same positions of Fig. 4.36(a)) are perfectly synchronized.
After the problem was solved, several data with all the targets have been collected

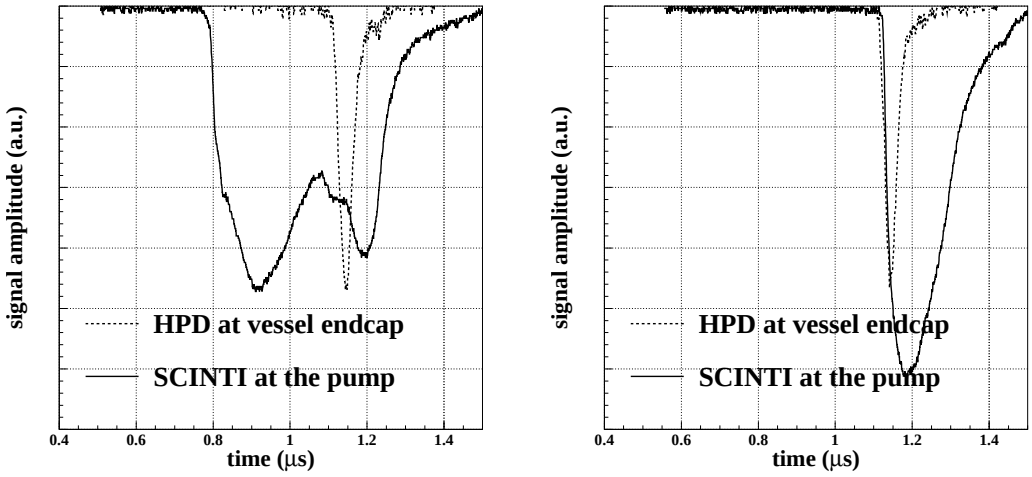

(a) (b)

Figure 4.36: Scope signals of the 3×10 cm^2 scintillator placed at the tracker entrance and of the HPD at the vessel endcap. (a) Pre-bunch antiprotons saturate the high sensitivity scintillators ~300 ns before the arrival of the main beam. (b) The same signals after the pre-bunch problem was solved.

(see a correct time profile in Fig. 4.37 and an example of a good reconstruction in the Sn target in Fig. 4.38). The ongoing analysis is dealing with the timing information of each fiber, with the correlation timing-hits and with the identification of the good bunches (since they were characterized by a high variability in intensity).

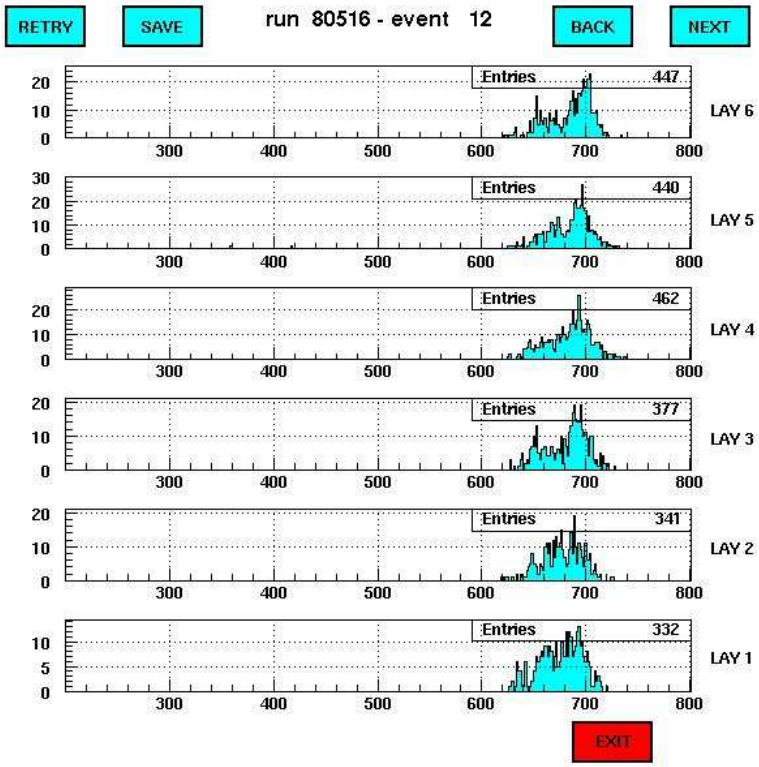

Figure 4.37: Time profile of the hit channels after the beam timing problem has been solved for the 2007 data taking (as a comparison, see Fig. 4.32). The tracker has a complete saturation at ~680 ns when the bunch annihilates on the endcap of the target vessel. A few tenths of ns before, corresponding to the target position, there can be some hit channels that are good candidates to be charged pions from an in-target annihilation.

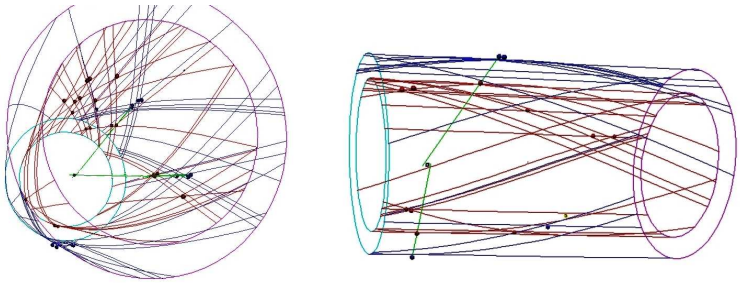

Figure 4.38: Annihilation event in Sn. The vertex is reconstructed in the target position (10 cm from the edge for this run).

Conclusions and outlooks

In this thesis work a scintillating fiber tracker (FAST) has been assembled and tested to perform a measurement of the antiproton annihilation cross section with different nuclei at the Antiproton Decelerator (AD) at CERN. It consists in 6 layers of 1 mm scintillating fibers readout by 42 multianode photomultipliers; each anode signal is amplified, shaped and discriminated by dedicated VLSI ASICs. A FPGA system samples the time the signal goes over threshold assigning a time tag to each event. The detector has more than 2000 readout channels. The 6 layers are organized in two shells with 3 layers each, an axial one (parallel to the beam direction) and two stereo (at $\pm 20^\circ$); the two shells radii are 12.2 cm and 15.6 cm. The maximum fiber length is $\lesssim$1 m; a total of 10 km of fibers have been used for the assembly.
The commissioning of the detector with cosmic rays lasted 1 month and was performed twice; the data analysis allowed a detailed characterization of the FAST performances and capabilities in terms of spatial resolution and time resolution.
The commissioning phase included the assembly of a prototype module built with the same fibers, the same multianode photomultiplier and the same readout electronics of the final tracker. The geometry reproduced the FAST one, that is 3 layers of fibers, in a double ribbon structure to eliminate dead zones, one longitudinal (0°) and two stereo placed at $\pm 20^\circ$ with respect to the longitudinal one. The prototype has been tested at the BTF line (Laboratori Nazionali di Frascati, Italy) that provides an electron beam with kinetic energies up to 500 MeV. The time resolution measured in these tests was 3 ns while a spatial resolution of 570 μm in ϕ and of 1.6 mm in z was obtained, in complete agreement with the expected values. The single efficiency layer is ~93%.
Several Montecarlo simulations, by means of the Geant3 program, have been implemented mostly to reproduce the geometrical structure of the fibers and to evaluate the possible intrinsic limits of such a detector. The prototype and the FAST tracker, in all the data taking configurations, have been reproduced.
The data of the commissioning phase have provided several information: on one

hand, the frontend and readout electronics fulfilled completely the design requirements; on the other, lot of difficulties have been met for the track reconstruction (in the cosmic ray case, no vertices could be found since the cosmic ray crossed the detector throughout) that seemed due to a mis-positioning of the fiber bundles and of the layers during the assembly procedure. Using the cosmic ray data, an off-line alignment has been tried which has solved problems only partially with the net result that the spatial resolution is worse than what expected and what measured in the test beam. The simulation allowed to compute the r and z vertex resolution in both cases (the prototype and the final detector): respectively 4.8 mm and 7.7 mm for the prototype, 12.6 mm and 17.6 mm for the tracker.

The FAST detector has been installed in the ASACUSA experimental area (AD, CERN) in September 2006, but, unfortunately, the unexpected bad beam characteristics prevented any data (useful for physics) to be collected. The antiproton beam in fact was not under control both from the time and dimension point of view (a pre-bunch was present that saturated completely the detector). The run has been used to test the detector performances while trying to solve the beam problem.
In July 2007, the second data taking period took place. The beam problem has been faced and solved; thus the first annihilation events have been collected and are shown in the very last part of this work.

As far as the next future is concerned, two other measurements are foreseen, both of them at energies below 100 keV. In these different experimental setups, the number of incoming antiprotons, due to the way the antiprotons are decelerated, will be orders of magnitude lower than the previous data takings, avoiding any possible saturation or pile-up. Some of the limits presented in this work have anyway to be faced. In particular the spatial resolution, which resulted to be poorer than the one computed with the simulation and measured with the prototype, seems due to the misalignment of several fiber/bundles. The position of each single fiber has to be reconstructed, and the only possibility at the moment is to use a high intensity (to save time) high energy (to avoid multiple scattering) beam, reconstructing the tracks with a high resolution detector (such as a silicon microstrip tracker). Computing the residuals (that is the difference between the reconstructed and the measured position), each region of FAST can be studied.
To improve the time resolution and also the track reconstruction capability, the present tracker geometry could be modified adding one outer cylinder of scintillators; given the larger radius, there would be no need of a high granularity, thus allowing the use of small rods (easier to manage from the mechanical point of

view) of plastic scintillators instead of fibers. The number of channels would not increase too much and, at the same time, the spatial resolution (especially in the ϕ direction) would be strongly enhanced also improving the capability of resolving the disambiguities in the vertex reconstruction.
One more item has to be faced to use this detector at AD, which is the possibility of controlling the antiproton beam size and position. Antiprotons of these energies annihilate immediately on the materials of the standard detectors used for this application (multiwire proportional chambers, scintillators) producing showers of charged pions that saturate the detectors themselves; an antiproton monitor before the tracker and at its end should be developed (using for example scintillating fibers at a very wide pitch) with the possibility of inserting or extracting it when needed.

List of acronyms

AA	Antiproton Accumulator
AC	Antiproton Collector
AD	Antiproton Decelerator
ADC	Analog to Digital Converter
ALPHA	Antihydrogen Laser PHysics Apparatus
APD	Avalanche PhotoDiode
ASACUSA	Atomic Spectroscopy And Collisions Using Slow Antiprotons
ASIC	Application Specific Integrated Circuit
ATRAP	Antihydrogen TRAP
BNL	Brookhaven National Laboratories
BTF	Beam Test Facility
CBAR	Crystal BARrel
CCD	Charged Coupled Device
CERN	European Organization for Nuclear Research (formerly Conseil Europeen pour la Recherche Nucleaire)
CFT	Central Fiber Tracker (DØ detector)
DAC	Digital to Analog Converter
DAQ	Data AcQuisition
EMA	Extra Mural Absorber
FAST	Fiber Antiproton Scintillating Tracker
FNAL	Fermi National Accelerator Laboratories
FPGA	Field Programmable Gate Array
FWHM	Full Width Half Maximum
HF3	3-Hydroxyflavone
KEK	High Energy Accelerator Research Organization (Japanese)
JDC	Jet Drifted Chamber
LEAR	Low Energy Antiproton Ring
LEP	Large Electron-Positron Collider

LINAC	LINear ACcelerator
MAPMT	Multi-Anode PhotoMultiplier Tube
MCP	Micro Channel Plate
MWPC	MultiWire Proportional Chamber
PAW	Physics Analysis Workstation
PCB	Printed Circuit Board
PDE	Photo Detection Efficiency
PH	Pulse Height
PMT	PhotoMultiplier Tube
PS	Proton Synchrotron
PVT	PolyVinilToluene
QCD	Quantum CromoDynamics
QED	Quantum ElectroDynamics
SEQ	SEQuencer
SFD	Scintillating Fiber Detector (UA2 experiment)
RFQD	Radio Frequency Quadrupole Decelerator
RMS	Root Mean Square
SiPM	Silicon PhotoMultiplier
Sp$\bar{p}$S	Super proton-antiproton Synchrotron
SPS	Super Proton Synchrotron
STRAD	STReamer chamber at AD
TDC	Time to Digital Converter
TOF	Time Of FLight
PMMA	Polymethyl-methacrylate
VLPC	Visible Light Photon Counter
VME	Versa Module Eurocard

List of Figures

1.1 Normalized antiproton yield 10
1.2 $\bar{p}$ momentum for maximum yield 11
1.3 FNAL antiproton factory 12
1.4 The CERN antiproton factory 13
1.5 The CERN Low-Energy Antiproton Ring (LEAR) 15
1.6 RFQ scheme 16
1.7 AD experimental hall 17
1.8 AD deceleration cycle. 18
1.9 KEK detector 20
1.10 Scheme of the ASTERIX detector 22
1.11 Scheme of the OBELIX detector 23
1.12 Crystal Barrel experiment detector 24
1.13 Antiproton annihilation cross section data 26
1.14 Antiproton cross section data for low energies 27
1.15 Proposed detector setup 29

2.1 π-states in organic scintillators molecules 34
2.2 Scheme of an optical fiber 36
2.3 Propagation of light within a fiber 37
2.4 Two possible fiber arrangements 40
2.5 Image intensifier with CCD readout 42
2.6 Hamamatsu H7546 series MAPMT 43
2.7 Avalanche Photodiode scheme 45
2.8 Silicon photomultiplier 46
2.9 VLPCs scheme and photo 48
2.10 UA2 Scintillating Fiber Detector (SFD) 49
2.11 DØ detector scheme 51

3.1 Scheme of the FAST detector 55

3.2 FAST tracker assembly 1 57
3.3 FAST tracker assembly 2 57
3.4 Hamamatsu R7600-M64 photomultiplier anodes scheme and photo 59
3.5 The FAST electronics chain 60
3.6 The FAST frontend board photo 61
3.7 The VA64TAP2.1 ASIC channel scheme 61
3.8 FAST repeater board 63
3.9 Data acquisition scheme 64
3.10 DAQ user interface 65
3.11 Tracker prototype photo 67
3.12 Tracker prototype scheme 67
3.13 Aerial view of the National Laboratories at Frascati, Rome. 68
3.14 Experimental setup at the BTF (Frascati, Rome) 70
3.15 PMT pedestal and RMS values 71
3.16 Pedestal and RMS values for the 4 silicon detector modules 72
3.17 Prototype DAQ scheme at the BTF 73
3.18 Plot of PH/RMS for the silicon modules and the prototype 74
3.19 PMT channels pulse height 75
3.20 Prototype pulse heights at different PMT bias values. 76
3.21 Beam profile plot of the prototype and of the silicon detectors . . . 77
3.22 Graphical monitor for event display 78
3.23 Scheme of the reconstruction of a hit 79
3.24 Prototype total number of hits 79
3.25 Reconstructed hit position 80
3.26 Example of an event with crosstalk 82
3.27 Crosstalk in the central region of the PMT 83
3.28 Region subsets considered in the crosstalk analysis 83
3.29 Crosstalk analysis for different PMT regions 84
3.30 Scheme of a tracking device with a digital readout 84
3.31 Prototype residual distribution 85
3.32 Energy loss of electrons and negative pions in the fiber 87
3.33 Scheme of the channel structure 88
3.34 Energy loss in the 4 fibers (Geant simulation) 89
3.35 Energy loss of 500 MeV electrons in the scintillating fiber 90
3.36 Number of photoelectrons produced by the fibers 92
3.37 Layer geometry as reproduced with the Geant simulation toolkit . 93
3.38 Pion multiplicity 95
3.39 Momentum distribution of $\pi^{\pm}$ produced in $\bar{p}p$ annihilations 96

3.40 Geometrical efficiency of the FAST tracker 97

4.1 Final detector assembly 101
4.2 Cosmic ray data taking different setups 102
4.3 Scintillation counters 103
4.4 Photo of the silicon tracker 104
4.5 Analysis software block diagram 107
4.6 Graphic event display 108
4.7 Graphic event display of the analysis software 109
4.8 Layer profile 110
4.9 Profile of the 6 FAST tracker layers 111
4.10 Layer 3 and 4 misalignment 112
4.11 Triangle height after layer 3 rotation 113
4.12 Residuals of outer triangles wrt the inner ones 114
4.13 Scheme of the acceptance angle defined in the text. 115
4.14 Efficiencies of the 6 layers as a function of the acceptance angle . . 115
4.15 Spatial resolution before and after the PMT alignment 118
4.16 ϕ and z spatial resolutions 119
4.17 Crosstalk analysis of the hit pads on the PMTs 120
4.18 Montecarlo simulation of the cosmic ray setup 122
4.19 Geant simulation of the cosmic ray data taking 123
4.20 Best triangle height for experimental data and the Geant simulation 124
4.21 Geant $\bar{p}p$ annihilation event 125
4.22 Reconstructed vertex residuals with the Geant simulation 128
4.23 Spatial resolution as a function of the annihilation position z 130
4.24 Spatial resolution as a function of the annihilation r 131
4.25 Experimental setup of the September 2006 data taking at AD 132
4.26 Electronics rack and gas control rack 133
4.27 ASACUSA experimental area at AD 134
4.28 Positioning of the scintillators during the data taking 134
4.29 Offline analysis interface 136
4.30 3D viewer of the vertex reconstruction program 137
4.31 Geant simulation of the 2006 data taking setup 138
4.32 Time profile of the hit channels 139
4.33 Experimental setup of the 2007 data taking at AD 141
4.34 Photo of the 2007 data taking setup 141
4.35 Target of the 2007 data taking 142
4.36 Scope signals of the reference detectors 144
4.37 Time profile of the hit channels after the beam problem was solved 145

4.38 Annihilation vertex reconstructed in the Sn target 145

List of Tables

2.1 BCF-10 scintillator properties (Bicron datasheet). 35
2.2 Properties of the most common wavelength shifter materials 36
2.3 Bicron BCF-10 scintillating fiber properties 39
2.4 Hamamatsu R7600-M64 multianode photomultiplier data 43
2.5 Optical crosstalk measured for the Hamamatsu H7546 MAPMT . . 44

3.1 Scintillating fiber layers features. 56
3.2 BCF-10 scintillating fiber data 58
3.3 Hamamatsu R7600-M64 photomultiplier characteristics 59
3.4 Beam parameters at BTF (Frascati) 69
3.5 Single layer efficiency results for the prototype 77
3.6 Plastic scintillator defined for the Montecarlo simulation 87

4.1 Efficiency values for the 6 layers 116
4.2 Coarse spatial resolution 118
4.3 Spatial resolutions with the best triangle and nearest methods . . . 119
4.4 Charged pion multiplicity (Geant simulation) 126
4.5 Vertex reconstruction resolution (Geant simulation) 127

Bibliography

[1] J. Eades and J. Hartman. Forty years of antiprotons. *Rev. Mod. Phys.*, 71: 373–419, 1999.

[2] K. P. Jungmann. Low energy antiproton experiments – a review. *Prog. Part. Nucl. Phys.*, 29:87–173, 1992. URL http://arxiv.org/abs/hep-ex/0512026v1.

[3] P. A. M. Dirac. A theory of electrons and protons. *Proc. Roy. Soc. London*, 126 A:360–365, 1930.

[4] C. D. Anderson. The positive electron. *Phys. Rev.*, 43:491–494, 1933.

[5] H. S. Bridge, D. O. Caldwell, Y. Pal, and B. Rossi. Possible example of the annihilation of a heavy particle. *Phys. Rev.*, 95:1101–1103, 1954.

[6] E. Amaldi *et al.* Unusual event produced by cosmic rays. *Nuovo Cim.*, 1: 492–500, 1955.

[7] H. S. Bridge, D. O. Caldwell, Y. Pal, and B. Rossi. Further analysis of the Massachusetts Institute of Technology antiproton event. *Phys. Rev.*, 102:930–931, 1956.

[8] O. Chamberlain, E. Segré, C. Wiegand, and T. Ypsilantis. Observation of antiprotons. *Phys. Rev.*, 100:947–950, 1955.

[9] B. Cork, G. R. Lambertson, O. Piccioni, and W. A. Wenzel. Antineutrons produced from antiprotons in charge-exchange collisions. *Phys. Rev.*, 102: 1193–1197, 1956.

[10] C. S. Wu *et al.* Experimental test of parity conservation in beta decay. *Phys. Rev.*, 105:1413, 1957.

[11] T. D. Lee and C. N. Yang. Question of parity conservation in weak interaction. *Phys. Rev.*, 104:254, 1956.

[12] E. Segré. Antinucleons. *Annu. Rev. Nucl. Sci.*, 8:127, 1958.

[13] K. M. Crowe. Masses of light mesons, K-mesons, and hyperons in 1956. *Nuovo Cim.*, 5:541, 1957.

[14] S. Bell. Time reversal in field theory. *Proc. R. Soc. London*, 231:479, 1955.

[15] G. Lüders. Die Entdeckung des Antiprotons. *Naturwissenschaften*, 43:121–123, 1956.

[16] G. Lüders and B. Zumino. Some consequences of *CPT*-invariance. *Phys. Rev.*, 106:385, 1957.

[17] T. D. Lee, R. Oehme, and C. N. Yang. Remarks on possible noninvariance under time reversal and charge conjugation. *Phys. Rev.*, 106:340, 1957.

[18] E. Klempt, C. Batty, and J.-M. Richard. The antinucleon–nucleon interaction at low energy: Annihilation dynamics. *Phys. Rep.*, 413:197–317, 2005.

[19] C Amsler and F Myhrer. Low energy antiproton physics. *Annu. Rev. Nucl. Part. Sci*, 41(1):219–267, 1991. doi: 10.1146/annurev.ns.41.120191.001251.

[20] D. M. Kaplan. Prospects for low-energy antiproton physics at Fermilab. *Nucl. Phys.*, A692:206–213, 2001.

[21] D. Möhl. International Workshop on Antimatter gravity and Antihydrogen Spectroscopy, Sepino. *Hyperfine Interact.*, 109:33, 1997.

[22] D. Möhl, G. Petrucci, L. Thorndahl, and S. van der Meer. Physics and technique of stochastic cooling. *Phys. Rep.*, 58:73, 1980.

[23] L. Evans and H. Koziol. *Proton-Antiproton Collider Physics*. ed. G. Altarelli and L. Di Lella, World Scientific, Singapore, 1989.

[24] AC Design Study Team. Design study of an antiproton collector for the antiproton accumulator. *CERN Yellow Report*, pages 83–10, 1983.

[25] LEAR Design Study Team. Design study of a facility for experiments with low energy antiprotons (LEAR), CERN. *CERN Report*, CERN/PS/DL 80–7, 1980.

[26] L. M. Simons. The cyclotron trap for antiprotons. *Hyperfine Interact.*, 81:253, 1993.

[27] I. M. Kapchinsky and V. A. Teplyakov. Linear accelerator with spatially homogeneous strong focusing. *Prib. Tekh. Eksp.*, page 19, 1970. (In Russian).

[28] S. Baird *et al.* Design study of the Antiproton Decelerator. *AD, CERN-PS/96-043 (AR)*, 1996.

[29] P. Belochitskii *et al.* Commissioning and first operation of the Antiproton Decelerator (AD). *Proceedings of the 2001 Particle Accelerator Conference, Chicago*, pages 580–584, 2001.

[30] P. Belochitskii on behalf of the AD team. Report on operation of Antiproton Decelerator. *AIP Conference Proceedings*, 821:48–56, 2006.

[31] E. P. Wigner. On the behaviour of cross section near threshold. *Phys. Rev.*, 73 (9):1002–1009, 1948.

[32] E. Klempt, F. Bradamante, A. Martin, and J.-M. Richard. Antinucleon–nucleon interaction at low energy: scattering and protonium. *Phys. Rep.*, 368:119–316, 2002.

[33] A. Bianconi *et al.* (The STRAD Collaboration). $\bar{p}$-nucleus Interactions at Low Energies with a Streamer Chamber at AD. CERN/SPSC 2000-037/P319, 2000.

[34] A. Gal, E. Friedman, and C.J. Batty. Saturation of low-energy antiproton annihilation of nuclei. *Phys. Lett. B*, 491:219–224, 2000.

[35] K. Protasov and R. Duperray. Antiproton annihilation on nuclei. 9th Intern. Conf. on Hadron Spectroscopy - CP619, 2002.

[36] S. Maury. The Antiproton Decelerator: AD. *Hyperfine Interact.*, 109:43–52, 1997.

[37] S. Maury on behalf of the AD team. The Antiproton Decelerator: AD. May 15 1999. Paper presented at LEAR Symposium, CERN.

[38] T. Forster. *Z. Naturforsh. A*, 4:321, 1949.

[39] I. B. Berlman. *Handbook of Fluorescence Spectra of Aromatic Molecules*. Academic, New York, 1971.

[40] T. O. White. Scintillating fibers. *Nucl. Instr. and Meth.*, A 273:820–825, 1988.

[41] W.-M. Yao *et al.* Review of Particle Physics. *Journal of Physics G*, 33:1+, 2006. URL http://pdg.lbl.gov.

[42] B. Baumbaugh *et al.* Performance of a large scale scintillating fiber tracker using VLPC readout. *IEEE Trans. Nucl. Sc.*, 43(3):1146–1152, 1996.

[43] I. Efthymiopoulos. Elastic Cross-Section and Luminosity Measurement in ATLAS at LHC, 2005. URL arXiv.org:hep-ex/0510078.

[44] A. Suzuki *et al.* (K2K Collaboration). Design, construction, and operation of SciFi tracking detector for K2K experiment. *Nucl. Instr. and Meth. A*, 453: 165–176, 2000.

[45] *Multianode photomultiplier tube assembly H7546A, H7546B*. HAMAMATSU PHOTONICS K. K., Electron Tube Division - Japan. URL http://www.hamamatsu.com.

[46] N. Tagg. *et al.* Performance of Hamamatsu 64-anode photomultipliers for use with wavelength–shifting optical fibres. *Nucl. Instr. and Meth. A*, 539:668–678, 2005.

[47] T. Yoshida and T. Sora. A prototype avalanche photodiode array for scintillating-fiber tracking detectors. *Nucl. Instr. and Meth. A*, 539:397–402, 2004.

[48] H. Dautet *et al.* Photon counting techniques with silicon avalanche photodiodes. *Appl. Opt.*, 32(21):3894, 1993.

[49] S. A. Vasile, D. Shamo, S. O. Shera, and G. J. Fishman. Development of Geiger-mode microavalanche photodiode arrays for fiberglast. volume 3765, pages 2–11. SPIE, 1999. doi: 10.1117/12.366489.

[50] A. Akindinov *et al.* New results on MRS APDs. *Nucl. Instr. and Meth. A*, 387: 231–234, 1997.

[51] G. Bondarenko *et al.* Limited Geiger-mode microcell silicon photodiode: new results. *Nucl. Instr. and Meth. A*, 442:187–192, 2000.

[52] E. Guschin *et al.* Multi-pixel Geiger-mode avalanche photodiodes with high quantum efficiency and low excess noise factor. *Nucl. Instr. and Meth. A*, 567: 250–254, 2006.

[53] O. Mineev, A. Afanasjev, and G. Bondarenko. Scintillator counters with multi-pixel avalanche photodiode readout for the ND280 detector of the T2K experiment, 2006. arXiv:physics/0606037v1.

[54] M. D. Petroff, M. G. Stapelbroek, and W. A. Kleinhans. Detection of individual 0.4–28 μm wavelength photons via impurity-impact ionization in a solid-state photomultiplier. *Appl. Phys. Lett.*, 51(6):406–408, 1987. doi: 10.1063/1.98404.

[55] J. Kim, Y. Yamamoto, and H. H. Hogue. Noise-free avalanche multiplication in Si solid state photomultipliers. *Appl. Phys. Lett.*, 70(21):2852–2854, 1997. doi: 10.1063/1.119022.

[56] E. Waks *et al.* High-efficiency photon-number detection for quantum information processing. *IEEE - Sel. Top. in Quant. Elect.*, 9(6):1512–1518, 2003.

[57] A. Bross *et al.* Time resolution and linearity measurements for a scintillating fiber detector instrumented with VLPCs. *Nucl. Instr. and Meth. A*, 394:87–96, 1997.

[58] R. E. Ansorge *et al.* Performance of a scintillating fibre detector for the UA2 upgrade. *Nucl. Instr. and Meth. A*, 265:33–49, 1988.

[59] S. G. Katvars, B. T. McCluskey, and J. M. Pentney. A fastbus digitiser for the UA2 scintillating fiber tracker. *Nucl. Instr. and Meth. A*, 276:482–491, 1989.

[60] J. Alitti *et al.* Performance of the scintillating fibre detector in the upgraded UA2 detector. *Nucl. Instr. and Meth. A*, 279:364–375, 1989.

[61] J. Kirkby. Today and tomorrow for scintillating fibre (SCIFI) detectors. *CERN-EP/87-60*, 1987.

[62] A. D. Bross. The DØ detector upgrade. *Nucl. Phys. Proc. Suppl.*, 44:12–19, 1995.

[63] J. Ellison. The DØ detector upgrade and physics program. 2000.

[64] DØ Central Fiber Tracker Home Page,
URL `http://d0server1.fnal.gov/projects/SciFi/cft_home.html`.

[65] A. E. Baumbaugh. Scintillating fiber detector performance, detector geometries, trigger, and electronics issues for scintillating fiber tracking. *Nucl. Instr. and Meth. A*, 360:1–6, 1995.

[66] S. Glenn *et al.* Tracking triggers for the upgraded DØ detector. *Nucl. Instr. and Meth. A*, 360:314–317, 1995.

[67] A. Mozzanica *et al.* Design and prototype results of the fast detector. *Nucl. Instr. and Meth.*, A 567:315–318, 2006.

[68] SBS Technologies Inc., US, `http://www.sbs.com`.

[69] Tck/Tl web site `http://www.tcl.tk`.

[70] M. Prest *et al.* The AGILE silicon tracker: an innovative γ-ray instrument for space. *Nucl. Instr. and Meth.*, A 520:280–287, 2003.

[71] *GEANT Detector Description and Simulation Tool*. Application Software Group, Computing and Networks Division – CERN Geneva, Switzerland, October 1994.

[72] L. Landau. On the energy loss of fast particles by ionisation. *J. Phys.(USSR)*, 8:201, 1944.

[73] J. E. Moyal. Theory of ionization fluctuations. *Phil. Mag.*, 7:46, 1955.

[74] Du Pont, USA, URL `http://www2.dupont.com`.

[75] M. C. Fujiwara and M. Marchesotti. A novel current mode operating beam counter based on not preamplified HPDs. *Nucl. Instr. and Meth. A*, 484:162–173, 2002.